



HAL
open science

Derivation and numerical approximation of two-temperature Euler plasma model

Afeintou Sangam, Élise Estibals, Hervé Guillard

► **To cite this version:**

Afeintou Sangam, Élise Estibals, Hervé Guillard. Derivation and numerical approximation of two-temperature Euler plasma model. *Journal of Computational Physics*, 2021, 444, pp.48. 10.1016/j.jcp.2021.110565 . hal-03543365

HAL Id: hal-03543365

<https://inria.hal.science/hal-03543365>

Submitted on 26 Jan 2022

HAL is a multi-disciplinary open access archive for the deposit and dissemination of scientific research documents, whether they are published or not. The documents may come from teaching and research institutions in France or abroad, or from public or private research centers.

L'archive ouverte pluridisciplinaire **HAL**, est destinée au dépôt et à la diffusion de documents scientifiques de niveau recherche, publiés ou non, émanant des établissements d'enseignement et de recherche français ou étrangers, des laboratoires publics ou privés.

DERIVATION AND NUMERICAL APPROXIMATION OF TWO-TEMPERATURE EULER PLASMA MODEL

AFEINTOU SANGAM^(*), ÉLISE ESTIBALS^(*), HERVÉ GUILLARD^(*)

(*) Université Côte d'Azur, INRIA, CNRS, LJAD, Faculté des Sciences, Parc Valrose, 06108 Nice Cedex 2, France
Afeintou.Sangam@univ-cotedazur.fr
Elise.Estibals@univ-cotedazur.fr
Herve.Guillard@univ-cotedazur.fr

Highlights

- Two-temperature Euler plasma model is an asymptotic regime for weakly magnetized plasma of two-fluid MHD system.
- Previous derivations are immediate consequences of our work.
- Newly designed robust relaxation scheme solves two-temperature Euler plasma model.
- Finite volume method in toroidal geometry, that retains the strong conservative form of equations of the model, is devised.
- Finite volume approximation is performed on unstructured mesh of tokamak toroidal geometry.

ABSTRACT. This paper gives a derivation of the two-temperature Euler plasma system from the two-fluid MHD model. The two-temperature Euler plasma system is proved to be an asymptotic regime for weakly magnetized plasma of the two-fluid MHD model. Our procedure is more general, enabling us to show that assumptions in previous derivations in literature are straightforward consequences of our work. We then propose a finite volume approximation to compute the solution of the two-temperature Euler plasma model in unstructured tessellations used to adequately mesh the toroidal geometry of the tokamak, where flows the plasma. Numerical tests illustrate our method.

Keywords: Two-Temperatures Euler plasma model, finite volume, relaxation scheme, unstructured mesh, toroidal geometry

CRedit authorship contribution statement

Afeintou Sangam: Conceptualization, Methodology, Software, Writing. **Élise Estibals:** Conceptualization, Methodology, Software, Writing. **Hervé Guillard:** Conceptualization, Methodology, Software, Writing.

Declaration of competing interest

The authors declare that they have no known competing financial interests or personal relationships that could have appeared to influence the work reported in this paper.

Acknowledgements: Afeintou Sangam thanks the following institutions that granted him opportunity to visit them allowing thus presentations of this work in their seminars and colloquia: the INRIA Project Laboratory FRATRES, the Magneto-Fluid Dynamics Division of the Courant Institute of Mathematical Sciences at New York University, the Lawrence Livermore National Laboratory, the Fields Institute for Research in Mathematical Sciences at Toronto and the Department of Mathematics at University of Toronto, and the Institut für Mathematik at Universität Zürich. He really appreciates intensive and rewarding discussions many colleagues in these institutions had with him around this work.

1. INTRODUCTION

A Plasma is a gas composed of electrons and ions that interact throughout electromagnetic forces [19, 23]. The dynamics of plasma charged particles can be described by a two-fluid MHD model. This description considers a plasma as a mixture of ions fluid and electrons fluid that are coupled by exchanged terms such as momentum transfer terms, ion and electron heating terms due to collisions, and undergoing electromagnetic forces. This system is quite intricate so that it is usually reduced to more tractable single fluid models. In such models, the plasma is described as one fluid whose characteristic quantities are weighted averages of ones of electrons and ions: only one density ρ , one velocity \mathbf{v} , either one temperature T or both ions temperature T_i and electrons temperature T_e are then considered [19, 23]. On one side, when the evolution of magnetic field is taken into account in a one-fluid model with one temperature T , the ideal or resistive MHD equations are then evoked, meaning that the plasma is a perfect electrical conductor or all dissipative processes are considered, respectively. On other side, the two-temperature Euler plasma model is an elaborated one-fluid model, in which electrons and ions possess two different temperatures, T_i for ions and T_e for electrons [13, 32, 1]. Such a description is assumed to reconstitute the correct

plasma behaviour once either the difference between T_i and T_e or the gradient of the deviation $T_i - T_e$ becomes important. The two-temperature Euler plasma model is known as either the bi-temperature Euler model or the T_i - T_e Euler model. The two-temperature Euler model is principally used in the context of Inertial Confinement Fusion [2], while the ideal and resistive MHD equations entered mainly in the frame of Magnetic Confinement Fusion [34]. As such, these two types of models are not often connected, making then questionable their domains of validity and their derivation from first principles. In particular, electromagnetic fields are not explicitly present in two-temperature model while they are important variables in the ideal and resistive MHD equations.

Here, we are concerned with a derivation and numerical approximation of two-temperature Euler plasma model. The derivation of two-temperature Euler model, the ideal and resistive MHD equations from the same background model is crucial, since it gives a solid foundation of modeling of plasma which exhibits different behaviors in physical domain of interest where it flows. In a tokamak for instance, the plasma presents a large variety of properties requiring different models to simultaneously describe it. Our derivation starts from the two-fluid MHD model. After scaling it with pertinent parameters such as the plasma β parameter, the electron and ion skin depths, the magnetic Reynold number, we identify the two-temperature Euler model. Our procedure is more general, enabling us to show that assumptions in previous derivations in literature [13, 32, 1] are straightforward consequences of our work.

Numerical approximation of the two-temperature Euler model is also challenging. An important part of the present work is concerned with a numerical approximation of two-temperature Euler model. The numerical approximation of the proposed model by finite volume schemes is difficult since the two-temperature Euler model system is non-conservative. A significant work towards the numerical computation of solutions of the two-temperature Euler model was suggested by Coquel and Marmignon in [13] for multi-species plasma: they transformed the non-conservative form into conservative one under the assumption of null electron entropy jump across shocks, and then solved the obtained system by a Roe-type scheme. As application of Riemann solvers derived in [17] in the Lagrangian framework, Després has proposed a remarkable procedure to compute two-temperature Euler model using again an equation of total energy and an equation on electron entropy. In the present work, a relaxation scheme is proposed to solve the two-temperature Euler model both in Cartesian and cylindrical coordinates. With in mind future applications to Magnetic Confinement Fusion, we study the modification of finite volume type method to approximate the solutions of the two-temperature Euler model in a toroidal geometry. Such a geometry is relevant in tokamaks [3, 4, 19, 27, 29, 34], and in astrophysical systems as stars and galaxies [23].

The difficulty when dealing with models in a toroidal geometry is to appropriately take into account curvilinear coordinate systems within equations are formulated. Put simply in other words, the strong conservative form of equations of the model can be destroyed, introducing artificial source terms if cautions are not considered when manipulating vectorial equations in curvilinear coordinates. The scheme we proposed is based on recent works reported in [9, 8] where it is shown that the strong conservative form of the model can be kept whatever the system of curvilinear coordinates used. More precisely, the finite volume scheme designed in this paper is an application of the method described in [9, 8] to the two-temperature Euler model in cylindrical coordinates for toroidal problems. However, such as application is not straightforward due to both the complexity of the two-temperature Euler model and the unstructured tessellation used to adequately mesh the toroidal geometry of the tokamak.

This work is organised as follows. In Section 2 a review of the two-fluid MHD model is given. We derive the two-temperature Euler model from the two-fluid MHD system, and show that it corresponds to an asymptotic regime for weakly magnetized plasmas. The two-temperature Euler model considered in this paper is introduced as a limit for large plasma β parameter of the two-fluid model. The mathematical properties of this model are then studied. A numerical strategy devised to approximate the two-temperature model constitutes the matter of Section 3. It is based on a finite volume method in a toroidal geometry addressed in [9, 8] coupled to a newly devised relaxation scheme. Numerical tests are performed in Section 4. A conclusion is finally given in Section 5.

2. DERIVATION OF THE TWO-TEMPERATURE EULER PLASMA MODEL

In this section, the two-fluid MHD plasma model is first presented, then the two-temperature Euler plasma system is derived from it. Finally, some mathematical properties of the two-temperature Euler equations, important for the numerical approximation envisaged in this paper, are addressed.

2.1. Two-fluid MHD plasma model. The two-fluid MHD model is a set of hydrodynamic equations combined to the low frequency Maxwell equations, intended to describe a totally ionized plasma in both weak and strong

magnetic fields. The two-fluid MHD equations are given by the following system:

$$\begin{cases} \partial_t \rho_e + \nabla \cdot (\rho_e \mathbf{u}_e) & = 0, & (1.a) \\ \partial_t \rho_i + \nabla \cdot (\rho_i \mathbf{u}_i) & = 0, & (1.b) \\ \partial_t (\rho_e \mathbf{u}_e) + \nabla \cdot (\rho_e \mathbf{u}_e \otimes \mathbf{u}_e) + \nabla p_e + \nabla \cdot \mathbf{\Pi}_e & = q_e n_e (\mathbf{E} + \mathbf{u}_e \times \mathbf{B}) + \mathbf{F}_{ei}, & (1.c) \\ \partial_t (\rho_i \mathbf{u}_i) + \nabla \cdot (\rho_i \mathbf{u}_i \otimes \mathbf{u}_i) + \nabla p_i + \nabla \cdot \mathbf{\Pi}_i & = q_i n_i (\mathbf{E} + \mathbf{u}_i \times \mathbf{B}) - \mathbf{F}_{ei}, & (1.d) \\ \partial_t \mathcal{E}_e + \nabla \cdot [(\mathcal{E}_e + p_e) \mathbf{u}_e] + \nabla \cdot (\mathbf{\Pi}_e \mathbf{u}_e) + \nabla \cdot \mathbf{Q}_e & = q_e n_e \mathbf{E} \cdot \mathbf{u}_e + \mathcal{Q}_{ei} + \mathbf{F}_{ei} \cdot \mathbf{u}_e, & (1.e) \\ \partial_t \mathcal{E}_i + \nabla \cdot [(\mathcal{E}_i + p_i) \mathbf{u}_i] + \nabla \cdot (\mathbf{\Pi}_i \mathbf{u}_i) + \nabla \cdot \mathbf{Q}_i & = q_i n_i \mathbf{E} \cdot \mathbf{u}_i + \mathcal{Q}_{ie} - \mathbf{F}_{ei} \cdot \mathbf{u}_i, & (1.f) \\ \partial_t \mathbf{B} & = -\nabla \times \mathbf{E}, & (1.g) \\ \mu_0 \mathbf{J} & = \nabla \times \mathbf{B}, & (1.h) \\ \varepsilon_0 \nabla \cdot \mathbf{E} & = \bar{\rho}, & (1.i) \\ \nabla \cdot \mathbf{B} & = 0. & (1.j) \end{cases}$$

The quantities that intervene in the two-fluid MHD model are collected in Table 1. The derivation of the two-fluid MHD model from plasma kinetic equations is addressed in [1, 4, 7, 16, 14, 19, 20, 23] and not reproduced in the present paper.

From experiment point of view, the mass density ρ of the mixture of ion and electron populations, the charge of the plasma $\bar{\rho}$, the velocity of the mixture \mathbf{u} and the current density \mathbf{J} matter instead of ρ_i , ρ_e , \mathbf{u}_i and \mathbf{u}_e . This translates to rewrite (1) in term of ρ , $\bar{\rho}$, \mathbf{u} , and \mathbf{J} using the bijection

$$\begin{cases} \rho & = m_e n_e + m_i n_i & = \rho_e + \rho_i, \\ \bar{\rho} & = q_e n_e + q_i n_i & = q_e \frac{\rho_e}{m_e} + q_i \frac{\rho_i}{m_i}, \\ \mathbf{u} & = \frac{m_e n_e \mathbf{u}_e + m_i n_i \mathbf{u}_i}{m_e n_e + m_i n_i} & = \frac{\rho_e}{\rho} \mathbf{u}_e + \frac{\rho_i}{\rho} \mathbf{u}_i, \\ \mathbf{J} & = q_e n_e \mathbf{u}_e + q_i n_i \mathbf{u}_i & = q_e \frac{\rho_e}{m_e} \mathbf{u}_e + q_i \frac{\rho_i}{m_i} \mathbf{u}_i. \end{cases}$$

Implicitly $\rho > 0$ is assumed throughout this work, meaning that phenomena leading to vacuum are excluded.

The formulation of the two-fluid MHD model (1) in term of ρ , $\bar{\rho}$, \mathbf{u} , and \mathbf{J} is postponed to Section 2.2, where quasi-neutrality assumption will enable further simplifications. For the moment, we are interested in writing (1.e), (1.f), in terms of total energy \mathcal{E}_T of two-fluid MHD model and electron entropy S_e . This choice is guided by the numerical approximation of the two-temperature Euler model suggested in this work and will be clarified at the end of this section. In this way, we recall the expression of the total mechanical energy \mathcal{E} of the plasma:

$$\mathcal{E} = \mathcal{E}_e + \mathcal{E}_i = \frac{1}{2} \rho_e \mathbf{u}_e^2 + \frac{p_e}{\gamma - 1} + \frac{1}{2} \rho_i \mathbf{u}_i^2 + \frac{p_i}{\gamma - 1},$$

where $\gamma = \frac{5}{3}$ is the monoatomic gases index. By summing the energy equations of the ions (1.e) and electrons (1.f), the equation of total mechanical energy \mathcal{E} is obtained:

$$(2) \quad \partial_t \mathcal{E} + \nabla \cdot [(\mathcal{E}_e + p_e) \mathbf{u}_e + (\mathcal{E}_i + p_i) \mathbf{u}_i] + \nabla \cdot (\mathbf{\Pi}_e \mathbf{u}_e + \mathbf{\Pi}_i \mathbf{u}_i) + \nabla \cdot (\mathbf{Q}_e + \mathbf{Q}_i) = \mathbf{E} \cdot \mathbf{J}.$$

Along this paper, the plasma charged particles speed is negligible with respect to light speed, so that the electromagnetic energy writes $\mathcal{E}_{EM} = \frac{\mathbf{B}^2}{2\mu_0}$ and undergoes the following equation:

$$(3) \quad \partial_t \mathcal{E}_{EM} + \nabla \cdot \left(\mathbf{E} \times \frac{\mathbf{B}}{\mu_0} \right) = -\mathbf{E} \cdot \mathbf{J}.$$

Therefore, adding (2) and (3) yields the equation of the total energy \mathcal{E}_T of the two-fluid MHD model:

$$(4) \quad \partial_t \mathcal{E}_T + \nabla \cdot \left[(\mathcal{E}_e + p_e) \mathbf{u}_e + (\mathcal{E}_i + p_i) \mathbf{u}_i + \mathbf{E} \times \frac{\mathbf{B}}{\mu_0} \right] + \nabla \cdot (\mathbf{\Pi}_e \mathbf{u}_e + \mathbf{\Pi}_i \mathbf{u}_i) + \nabla \cdot (\mathbf{Q}_e + \mathbf{Q}_i) = 0,$$

where the total energy, the sum of the mechanical and electromagnetic energies, is given by

$$(5) \quad \mathcal{E}_T = \mathcal{E}_i + \mathcal{E}_e + \frac{1}{2\mu_0} \mathbf{B}^2 = \frac{p_i + p_e}{\gamma - 1} + \frac{1}{2} \rho_i \mathbf{u}_i^2 + \frac{1}{2} \rho_e \mathbf{u}_e^2 + \frac{1}{2\mu_0} \mathbf{B}^2.$$

Inserting the definition of electron pressure p_e into (1.e) gives:

$$(6) \quad \partial_t p_e + \mathbf{u}_e \cdot \nabla p_e + \gamma p_e \nabla \cdot \mathbf{u}_e + (\gamma - 1) [\mathbf{\Pi}_e : \nabla \mathbf{u}_e + \nabla \cdot \mathbf{Q}_e] = (\gamma - 1) \mathcal{Q}_{ei}.$$

Now plugging the definition of electron entropy $S_e = p_e \rho_e^{-\gamma}$ into the electron pressure equation (6) leads to

$$(7) \quad \partial_t (\rho_e S_e) + \nabla \cdot (\rho_e S_e \mathbf{u}_e) + \rho_e^{1-\gamma} (\gamma - 1) [\mathbf{\Pi}_e : \nabla \mathbf{u}_e + \nabla \cdot \mathbf{Q}_e] = \rho_e^{1-\gamma} (\gamma - 1) \mathcal{Q}_{ei}.$$

Let us emphasize that for smooth (\mathcal{C}^2) solutions, it is mathematically equivalent to use in (1) instead of the two equations for the mechanical energies of the species, any two independent equations derived from any combination of these equations. However, for discontinuous solutions, these combinations are not equivalent. In the sequel, we will choose for one of these two equations, the total energy equation (4) since this one has a clear physical meaning. We must then supplement it by another equation. A rigorous procedure [5] would be to choose this equation based on the analysis of travelling wave solutions of the system (1). However, this analysis presents formidable mathematical difficulties that are far beyond the scope of this work. Instead we will complement equation (4) by an equation

Name	Notation	Formulae
Boltzmann constant	k_B	
Vacum permeability	μ_0	
Vacum permittivity	ε_0	
Electron mass	m_e	
Ion mass	m_i	
Electron charge	q_e	
Ion charge	q_i	
Electron number density	n_e	
Ion number density	n_i	
Electron mass density	ρ_e	$\rho_e = m_e n_e$
Ion mass density	ρ_i	$\rho_i = m_i n_i$
Mass density of mixture	ρ	$\rho = m_e n_e + m_i n_i$
Plasma charge	$\bar{\rho}$	$\bar{\rho} = q_e n_e + q_i n_i$
Electron velocity	\mathbf{u}_e	
Ion velocity	\mathbf{u}_i	
velocity of mixture	\mathbf{u}	$\mathbf{u} = \frac{m_e n_e \mathbf{u}_e + m_i n_i \mathbf{u}_i}{m_e n_e + m_i n_i}$
Plasma current	\mathbf{J}	$\mathbf{J} = q_e n_e \mathbf{u}_e + q_i n_i \mathbf{u}_i$
Electron temperature	T_e	
Ion temperature	T_i	
Electron pressure	p_e	$p_e = k_B n_e T_e$
Ion pressure	p_i	$p_i = k_B n_i T_i$
Electron traceless stress tensor	$\mathbf{\Pi}_e$	
Ion traceless stress tensor	$\mathbf{\Pi}_i$	
Electron energy	\mathcal{E}_e	$\mathcal{E}_e = \rho_e \mathbf{u}_e^2 / 2 + 3k_B n_e T_e / 2$
Ion energy	\mathcal{E}_i	$\mathcal{E}_i = \rho_i \mathbf{u}_i^2 / 2 + 3k_B n_i T_i / 2$
Electron heat flux	\mathbf{Q}_e	
Ion heat flux	\mathbf{Q}_i	
Electron/ion collision time	τ_{ei}	
Ion/electron collision time	τ_{ie}	
Electron/ion collision frequency	ν_{ei}	$\nu_{ei} = 1/\tau_{ei}$
Ion/electron collision frequency	ν_{ie}	$\nu_{ie} = 1/\tau_{ie}$
Electron/ion frictional force	\mathbf{F}_{ei}	$\mathbf{F}_{ei} = \frac{m_e m_i}{(\tau_{ie} m_e + \tau_{ei} m_i) e} \mathbf{J}$
Ion/electron frictional force	\mathbf{F}_{ie}	$\mathbf{F}_{ie} = -\mathbf{F}_{ei}$
Ion heat flux	\mathbf{q}_i	
Electron/ion energy exchange coefficient rate	$\nu_{ei}^{\mathcal{E}}$	$\nu_{ei}^{\mathcal{E}} = \frac{3}{2} k_B \frac{n_e n_i}{\nu_{ie} n_e + \nu_{ei} n_i}$
Ion/electron energy exchange coefficient rate	$\nu_{ie}^{\mathcal{E}}$	
	Q_{ei}	$Q_{ei} = \nu_{ei}^{\mathcal{E}} (T_i - T_e)$ $+ \frac{1}{2} \left[\frac{\tau_{ei} \rho_i}{\tau_{ie} \rho_e + \tau_{ei} \rho_i} + \frac{\tau_{ie} n_e}{\tau_{ie} n_e + \tau_{ei} n_i} \right] \mathbf{F}_{ei} \cdot (\mathbf{u}_i - \mathbf{u}_e)$
	Q_{ie}	$Q_{ie} = -\nu_{ie}^{\mathcal{E}} (T_i - T_e)$ $+ \frac{1}{2} \left[\frac{\tau_{ie} \rho_e}{\tau_{ie} \rho_e + \tau_{ei} \rho_i} + \frac{\tau_{ei} n_i}{\tau_{ie} n_e + \tau_{ei} n_i} \right] \mathbf{F}_{ei} \cdot (\mathbf{u}_i - \mathbf{u}_e)$
Electric field	\mathbf{E}	
Magnetic field	\mathbf{B}	

TABLE 1. Characteristic quantities of the two-fluid MHD model.

for the electron entropy. For discontinuous solutions, this implies (see the next section) that we assume that the electron entropy remains constant through a shock. This assumption is the translation of the Born-Oppenheimer approximation that decouples the plasma motion into frozen nuclei and free electrons that adjust adiabatically to nuclei background [11, 12, 26]. This is reasonable since the mass of the electrons is considerably smaller than the one of the ions. Thus one can expect that the changes in the electron entropy will have a minimal impact on the behaviour of the other macroscopic quantities. This assumption on entropy has also been used in different context than plasma physics for instance in the modelling of multiphase flows where the hypothesis that the entropy of the lighter species is constant has shown to give results in reasonable agreement with the experiments [21]. Thus, from

now on, the equations of the two-fluid MHD model to be considered are the following:

$$(8) \quad \left\{ \begin{array}{l} \partial_t \rho_e + \nabla \cdot (\rho_e \mathbf{u}_e) \\ \partial_t \rho_i + \nabla \cdot (\rho_i \mathbf{u}_i) \\ \partial_t (\rho_e \mathbf{u}_e) + \nabla \cdot (\rho_e \mathbf{u}_e \otimes \mathbf{u}_e) + \nabla p_e + \nabla \cdot \mathbf{\Pi}_e \\ \partial_t (\rho_i \mathbf{u}_i) + \nabla \cdot (\rho_i \mathbf{u}_i \otimes \mathbf{u}_i) + \nabla p_i + \nabla \cdot \mathbf{\Pi}_i \\ \\ \partial_t \mathcal{E}_T + \nabla \cdot \left[(\mathcal{E}_e + p_e) \mathbf{u}_e + (\mathcal{E}_i + p_i) \mathbf{u}_i + \mathbf{E} \times \frac{\mathbf{B}}{\mu_0} \right] + \nabla \cdot (\mathbf{\Pi}_e \mathbf{u}_e + \mathbf{\Pi}_i \mathbf{u}_i) + \nabla \cdot (\mathbf{Q}_e + \mathbf{Q}_i) \\ \partial_t (\rho_e S_e) + \nabla \cdot (\rho_e S_e \mathbf{u}_e) + \rho_e^{1-\gamma} (\gamma - 1) [\mathbf{\Pi}_e : \nabla \mathbf{u}_e + \nabla \cdot \mathbf{Q}_e] \\ \partial_t \mathbf{B} \\ \mu_0 \mathbf{J} \\ \varepsilon_0 \nabla \cdot \mathbf{E} \\ \nabla \cdot \mathbf{B} \end{array} \right. = \begin{array}{l} 0, \\ 0, \\ q_e n_e (\mathbf{E} + \mathbf{u}_e \times \mathbf{B}) + \mathbf{F}_{ei}, \\ q_i n_i (\mathbf{E} + \mathbf{u}_i \times \mathbf{B}) - \mathbf{F}_{ei}, \\ \\ 0, \\ \rho_e^{1-\gamma} (\gamma - 1) \mathcal{Q}_{ei}, \\ -\nabla \times \mathbf{E}, \\ \nabla \times \mathbf{B}, \\ \bar{\rho}, \\ 0. \end{array}$$

2.2. The two-temperature Euler plasma model. We are concerned in this section with the derivation of the two-temperature Euler plasma model. The quasi-neutrality assumption of the plasma is reviewed. After scaling the two-fluid equations, we show that two-temperature Euler plasma model is the limit of two-fluid equations for large plasma parameter β , meaning that dynamical pressure largely dominates the electromagnetic effects.

2.2.1. The quasi-neutral regime. As ε_0 is very small, it is reasonable to assume that the local charge of the plasma is near zero:

$$\varepsilon_0 \nabla \cdot \mathbf{E} \approx 0$$

leading to the plasma quasi-neutrality assumption:

$$0 = \bar{\rho} = q_e n_e + q_i n_i.$$

The quasi-neutrality hypothesis deserves itself a huge literature, recent studies could be found in [32]. With $q_e = -e$, where $e = 1.6022 \times 10^{-19} C$ is the elementary charge, and $q_i = Ze$, Z being the charge number of the ion, an immediate consequence of quasi-neutrality assumption is: $n_e = Zn_i$. Since we are concerned with Deuterium-Tritium plasma, $Z = 1$, we get:

$$n_e = n_i = n.$$

The mass densities ρ_i , ρ_e , and ρ are thus proportional:

$$c_i = \frac{\rho_i}{\rho} = \frac{m_i}{m_e + m_i}, \quad c_e = \frac{\rho_e}{\rho} = \frac{m_e}{m_e + m_i}.$$

The quantities c_e , c_i , are known as electron mass concentration, and ion mass concentration, respectively. As consequence, only one equation for mass density is needed, and in the sequel we retain the equation of ρ , the mass density of the mixture:

$$(9) \quad \partial_t \rho + \nabla \cdot (\rho \mathbf{u}) = 0.$$

Under the quasi-neutrality assumption, \mathbf{u} , and \mathbf{J} take the following form:

$$\left\{ \begin{array}{l} \mathbf{u} = c_i \mathbf{u}_i + c_e \mathbf{u}_e, \\ \mathbf{J} = ne (\mathbf{u}_i - \mathbf{u}_e), \end{array} \right.$$

that can be inverted into:

$$\left\{ \begin{array}{l} \mathbf{u}_i = \mathbf{u} + \frac{c_e}{ne} \mathbf{J}, \\ \mathbf{u}_e = \mathbf{u} - \frac{c_i}{ne} \mathbf{J}. \end{array} \right.$$

Next we substitute equations on $\rho \mathbf{u}$ and \mathbf{J} for equations on $\rho_e \mathbf{u}_e$ and $\rho_i \mathbf{u}_i$. Summing equations on $\rho_e \mathbf{u}_e$ and $\rho_i \mathbf{u}_i$, and using $\rho \mathbf{u} = \rho_e \mathbf{u}_e + \rho_i \mathbf{u}_i$, give:

$$(10) \quad \partial_t (\rho \mathbf{u}) + \nabla \cdot (\rho \mathbf{u} \otimes \mathbf{u}) + \nabla \cdot [\rho_e \mathbf{u}_e \otimes (\mathbf{u}_e - \mathbf{u}) + \rho_i \mathbf{u}_i \otimes (\mathbf{u}_i - \mathbf{u})] + \nabla p + \nabla \cdot \mathbf{\Pi} = \bar{\rho} \mathbf{E} + \mathbf{J} \times \mathbf{B},$$

where $p = p_e + p_i$ is the total pressure and $\mathbf{\Pi} = \mathbf{\Pi}_e + \mathbf{\Pi}_i$ is the traceless total stress tensor. Immediately, the total momentum equation turns to:

$$(11) \quad \partial_t (\rho \mathbf{u}) + \nabla \cdot (\rho \mathbf{u} \otimes \mathbf{u}) + \frac{m_i m_e}{m_i + m_e} \nabla \cdot \left(\frac{\mathbf{J} \otimes \mathbf{J}}{ne^2} \right) + \nabla p + \nabla \cdot \mathbf{\Pi} = \mathbf{J} \times \mathbf{B}.$$

Regarding the current equation, the momentum equations of electron and ions are rewritten in the following form

$$(12) \quad \partial_t (n_e \mathbf{u}_e) + \nabla \cdot (n_e \mathbf{u}_e \otimes \mathbf{u}_e) + \frac{1}{m_e} (\nabla p_e + \nabla \cdot \mathbf{\Pi}_e) = \frac{q_e n_e}{m_e} (\mathbf{E} + \mathbf{u}_e \times \mathbf{B}) + \frac{1}{m_e} \mathbf{F}_{ei},$$

$$(13) \quad \partial_t (n_i \mathbf{u}_i) + \nabla \cdot (n_i \mathbf{u}_i \otimes \mathbf{u}_i) + \frac{1}{m_i} (\nabla p_i + \nabla \cdot \mathbf{\Pi}_i) = \frac{q_i n_i}{m_i} (\mathbf{E} + \mathbf{u}_i \times \mathbf{B}) - \frac{1}{m_i} \mathbf{F}_{ei}.$$

By multiplying the equation (12) by q_e and the equation (13) by q_i and finally summing the results leads to the generalized Ohm's law

$$(14) \quad \begin{aligned} & \partial_t \mathbf{J} + \nabla \cdot [n_e q_e \mathbf{u}_e \otimes \mathbf{u}_e + n_i q_i \mathbf{u}_i \otimes \mathbf{u}_i] + \frac{n_e q_e}{\rho_e} (\nabla p_e + \nabla \cdot \mathbf{\Pi}_e) + \frac{n_i q_i}{\rho_i} (\nabla p_i + \nabla \cdot \mathbf{\Pi}_i) \\ &= \left(\frac{(n_e q_e)^2}{\rho_e} + \frac{(n_i q_i)^2}{\rho_i} \right) \mathbf{E} + \left(\frac{(n_e q_e)^2}{\rho_e} \mathbf{u}_e + \frac{(n_i q_i)^2}{\rho_i} \mathbf{u}_i \right) \times \mathbf{B} + \left(\frac{\rho_i}{\rho_e} - \frac{n_i q_i}{\rho_i} \right) \mathbf{F}_{ei}. \end{aligned}$$

Thanks to quasi-neutrality simplifications, the generalized Ohm's law becomes

$$(15) \quad \begin{aligned} & \frac{m_i m_e}{m_e + m_i} \left[\frac{1}{e} \left(\partial_t \mathbf{J} + \nabla \cdot (\mathbf{u} \otimes \mathbf{J} + \mathbf{J} \otimes \mathbf{u}) \right) \right] - \frac{m_e m_i (m_i - m_e)}{(m_e + m_i)^2} \nabla \cdot \left(\frac{1}{ne^2} \mathbf{J} \otimes \mathbf{J} \right) \\ & + c_e [\nabla p_i + \nabla \cdot \mathbf{\Pi}_i] - c_i [\nabla p_e + \nabla \cdot \mathbf{\Pi}_e] = ne \left[\mathbf{E} + \mathbf{u} \times \mathbf{B} - \eta \mathbf{J} \right] - \frac{m_i - m_e}{m_i + m_e} \mathbf{J} \times \mathbf{B}, \end{aligned}$$

where η is the isotropic resistivity of the plasma defined by

$$(16) \quad \eta = \frac{m_i m_e}{ne^2 (\tau_{ie} m_e + \tau_{ei} m_i)}.$$

Under the quasi-neutrality assumption, the equation of the total energy \mathcal{E}_T of the two-fluid model writes:

$$(17) \quad \begin{aligned} & \partial_t \mathcal{E}_T + \nabla \cdot \left[(\mathcal{E} + p_e + p_i) \mathbf{u} + \mathbf{E} \times \frac{\mathbf{B}}{\mu_0} \right] + \nabla \cdot \left[(c_e (\mathcal{E}_i + p_i) - c_i (\mathcal{E}_e + p_e)) \frac{\mathbf{J}}{ne} \right] \\ & + \nabla \cdot ((\mathbf{\Pi}_e + \mathbf{\Pi}_i) \mathbf{u}) + \nabla \cdot ((c_e \mathbf{\Pi}_i - c_i \mathbf{\Pi}_e) \frac{\mathbf{J}}{ne}) + \nabla \cdot (\mathbf{Q}_e + \mathbf{Q}_i) = 0. \end{aligned}$$

For the electron entropy, we simplify the expression of \mathcal{Q}_{ei} with the quasi-neutrality assumption

$$\mathcal{Q}_{ei} = \nu_{ei}^{\mathcal{E}} (T_i - T_e) + \zeta_{ei} \eta \mathbf{J}^2,$$

where

$$(18) \quad \zeta_{ei} = \frac{1}{2} \left[\frac{\tau_{ei} m_i}{\tau_{ie} m_e + \tau_{ei} m_i} + \frac{\tau_{ie}}{\tau_{ie} + \tau_{ei}} \right],$$

and finally, the electron entropy equation of system (8) becomes

$$\begin{aligned} & \partial_t (\rho_e S_e) + \nabla \cdot (\rho_e S_e \mathbf{u}) - c_i \nabla \cdot \left(\frac{1}{ne} \rho_e S_e \mathbf{J} \right) + \rho_e^{1-\gamma} (\gamma - 1) [\mathbf{\Pi}_e : \nabla \mathbf{u} + \nabla \cdot \mathbf{Q}_e] \\ & - c_i \rho_e^{1-\gamma} (\gamma - 1) \mathbf{\Pi}_e : \nabla \left(\frac{1}{ne} \mathbf{J} \right) = \rho_e^{1-\gamma} (\gamma - 1) [\nu_{ei}^{\mathcal{E}} (T_i - T_e) + \zeta_{ei} \eta \mathbf{J}^2]. \end{aligned}$$

As consequence, the two-fluid MHD equations in the quasi-neutral regime write:

$$\left\{ \begin{array}{l} \partial_t \rho + \nabla \cdot (\rho \mathbf{u}) = 0, \\ \partial_t (\rho \mathbf{u}) + \nabla \cdot (\rho \mathbf{u} \otimes \mathbf{u}) + \frac{m_e m_i}{m_e + m_i} \nabla \cdot \left(\frac{1}{ne^2} \mathbf{J} \otimes \mathbf{J} \right) + \nabla p + \nabla \cdot \mathbf{\Pi} = \mathbf{J} \times \mathbf{B}, \\ \frac{m_i m_e}{m_e + m_i} \left[\frac{1}{e} \left(\partial_t \mathbf{J} + \nabla \cdot (\mathbf{u} \otimes \mathbf{J} + \mathbf{J} \otimes \mathbf{u}) \right) \right] - \frac{m_e m_i (m_i - m_e)}{(m_e + m_i)^2} \nabla \cdot \left(\frac{1}{ne^2} \mathbf{J} \otimes \mathbf{J} \right) \\ + c_e [\nabla p_i + \nabla \cdot \mathbf{\Pi}_i] - c_i [\nabla p_e + \nabla \cdot \mathbf{\Pi}_e] = ne \left[\mathbf{E} + \mathbf{u} \times \mathbf{B} - \eta \mathbf{J} \right] - \frac{m_i - m_e}{m_i + m_e} \mathbf{J} \times \mathbf{B}, \\ \partial_t \mathcal{E}_T + \nabla \cdot \left[(\mathcal{E} + p_e + p_i) \mathbf{u} + \mathbf{E} \times \frac{\mathbf{B}}{\mu_0} \right] + \nabla \cdot \left[(c_e (\mathcal{E}_i + p_i) - c_i (\mathcal{E}_e + p_e)) \frac{1}{ne} \mathbf{J} \right] \\ + \nabla \cdot (\mathbf{\Pi}_e \mathbf{u}_e + \mathbf{\Pi}_i \mathbf{u}_i) + \nabla \cdot (\mathbf{Q}_e + \mathbf{Q}_i) = 0, \\ \partial_t (\rho_e S_e) + \nabla \cdot (\rho_e S_e \mathbf{u}) - c_i \nabla \cdot \left(\frac{1}{ne} \rho_e S_e \mathbf{J} \right) + \rho_e^{1-\gamma} (\gamma - 1) [\mathbf{\Pi}_e : \nabla \mathbf{u} + \nabla \cdot \mathbf{Q}_e] \\ - c_i \rho_e^{1-\gamma} (\gamma - 1) \mathbf{\Pi}_e : \nabla \left(\frac{1}{ne} \mathbf{J} \right) = \rho_e^{1-\gamma} (\gamma - 1) [\nu_{ei}^{\mathcal{E}} (T_i - T_e) + \zeta_{ei} \eta \mathbf{J}^2], \\ \partial_t \mathbf{B} = -\nabla \times \mathbf{E}, \\ \mu_0 \mathbf{J} = \nabla \times \mathbf{B}, \\ \nabla \cdot \mathbf{B} = 0. \end{array} \right.$$

In the sequel, we will neglect the dissipative effects in the previous system in order to concentrate on the first-order part of the system. Neglecting dissipative terms usually means that we are mainly interested in the short term behaviour of the system since dissipative phenomena are generally associated to large time scales. Therefore, the

system that we will consider from now on is

$$(19) \quad \left\{ \begin{array}{l} \partial_t \rho + \nabla \cdot (\rho \mathbf{u}) = 0, \\ \partial_t (\rho \mathbf{u}) + \nabla \cdot (\rho \mathbf{u} \otimes \mathbf{u}) + \frac{m_e m_i}{m_e + m_i} \nabla \cdot \left(\frac{1}{ne^2} \mathbf{J} \otimes \mathbf{J} \right) + \nabla (p_e + p_i) = \mathbf{J} \times \mathbf{B}, \\ \frac{m_i m_e}{m_e + m_i} \left[\frac{1}{e} \left(\partial_t \mathbf{J} + \nabla \cdot (\mathbf{u} \otimes \mathbf{J} + \mathbf{J} \otimes \mathbf{u}) \right) \right] - \frac{m_e m_i (m_i - m_e)}{(m_e + m_i)^2} \nabla \cdot \left(\frac{1}{ne^2} \mathbf{J} \otimes \mathbf{J} \right) \\ + c_e \nabla p_i - c_i \nabla p_e = ne \left[\mathbf{E} + \mathbf{u} \times \mathbf{B} - \eta \mathbf{J} \right] - \frac{m_i - m_e}{m_i + m_e} \mathbf{J} \times \mathbf{B}, \\ \partial_t \mathcal{E}_T + \nabla \cdot \left[(\mathcal{E} + p_e + p_i) \mathbf{u} + \mathbf{E} \times \frac{\mathbf{B}}{\mu_0} \right] + \nabla \cdot \left[\left(c_e (\mathcal{E}_i + p_i) - c_i (\mathcal{E}_e + p_e) \right) \frac{1}{ne} \mathbf{J} \right] = 0, \\ \partial_t (\rho_e S_e) + \nabla \cdot (\rho_e S_e \mathbf{u}) - c_i \nabla \cdot \left(\frac{1}{ne} \rho_e S_e \mathbf{J} \right) = \rho_e^{1-\gamma} (\gamma - 1) [\nu_{ei}^{\mathcal{E}} (T_i - T_e) + \zeta_{ei} \eta \mathbf{J}^2], \\ \partial_t \mathbf{B} = -\nabla \times \mathbf{E}, \\ \mu_0 \mathbf{J} = \nabla \times \mathbf{B}, \\ \nabla \cdot \mathbf{B} = 0. \end{array} \right.$$

2.2.2. *The scalings.* The system (19) contains two momentum equations: one for the total momentum $\rho \mathbf{u}$ and one for the current density \mathbf{J} . Our goal now is to eliminate the fast part of the dynamics related to the movement of the electrons while keeping the possibility for the ions and electrons to have different temperatures. To establish the range of validity of this simplification, we introduce non-dimensional parameters and to this end, we first begin by setting the reference quantities in order to express (19) in non-dimensional form. First, we denote respectively, L_0 , n_0 , $T_{e,0}$, $T_{i,0}$, and B_0 the reference length, density, electron temperature, ion temperature, and magnetic field strength. Then, since we are interested in phenomena where the velocities can be large, we introduce a reference velocity u_0 defined as:

$$(20) \quad u_0 = \sqrt{\frac{k_B (T_{e,0} + T_{i,0})}{m_e + m_i}}.$$

Later on, we will see that this velocity corresponds to the speed of sound of the ion-electron mixture. Thus, this choice of velocity scale means that we are interested in phenomena where the material velocity is comparable to the speed of sound. The time scale is chosen such that

$$t_0 = \frac{L_0}{u_0},$$

and this implies as usual that this choice of scales leaves unchanged the continuity equation and the material derivatives. Then from the state laws $n_\alpha k_B T_\alpha = p_\alpha$, the pressure scales are defined by

$$p_{\alpha,0} = n_0 k_B T_{\alpha,0},$$

where $\alpha = e$ for electron, and $\alpha = i$ for ion.

From the Maxwell-Ampère equation, we will also use the following scaling to define the reference current:

$$J_0 = \frac{B_0}{L_0 \mu_0}.$$

Then each variable is re-defined in term of reference quantities and non-dimensional variables as:

$$\tilde{t} = \frac{t}{t_0}, \quad \tilde{\mathbf{x}} = \frac{1}{L_0} \mathbf{x}, \quad \tilde{\mathbf{u}} = \frac{1}{u_0} \mathbf{u}, \quad \tilde{\rho} = \frac{\rho}{(m_e + m_i) n_0}, \quad \tilde{T}_\alpha = \frac{T_\alpha}{T_{\alpha,0}}, \quad \alpha = e, i, \quad \tilde{\mathbf{B}} = \frac{1}{B_0} \mathbf{B},$$

where a super tilde $\tilde{\cdot}$ denotes a non-dimensional variable.

We recall the following parameters which are important for the analysis that we will be conducted later. The total plasma β parameter:

$$(21) \quad \beta = \frac{(m_e + m_i) n_0 u_0^2}{B_0^2 / \mu_0} = \frac{n_0 k_B (T_{e,0} + T_{i,0})}{B_0^2 / \mu_0}$$

measures the ratio between the dynamic pressure and the magnetic pressure. It is worthwhile to mention that our definition is different from the usual plasma parameter $\frac{(m_e + m_i) n_0 u_0^2}{B_0^2 / 2 \mu_0}$, by a factor 2, that is no importance since in the sequel we are considering the asymptotic form of the equation obtained when $\beta \rightarrow +\infty$.

The plasma electron frequency ω_{pe} is given by:

$$(22) \quad \omega_{pe}^2 = \frac{n_0 e^2}{\varepsilon_0 m_e} = \frac{n_0 e^2 c^2 \mu_0}{m_e}.$$

The electron skin depth δ_e represents the distance travelled by the light with speed c in the plasma at electron frequency ω_{pe} and is defined by:

$$(23) \quad \delta_e^2 = \frac{c^2}{\omega_{pe}^2} = \frac{m_e}{n_0 e^2 \mu_0}.$$

Similarly, the plasma ion frequency ω_{pi} and the electron skin depth δ_i are defined by:

$$(24) \quad \omega_{pe}^2 = \frac{n_0 e^2}{\varepsilon_0 m_e} = \frac{n_0 e^2 c^2 \mu_0}{m_e}, \quad \delta_i^2 = \frac{c^2}{\omega_{pi}^2} = \frac{m_i}{n_0 e^2 \mu_0},$$

so that:

$$(25) \quad \frac{\delta_i}{\delta_e} = \sqrt{\frac{m_i}{m_e}} \approx 40.$$

According to [18] the value of the plasma frequency ω_{pe} varies between 6.10^{11} in tokamaks and 6.10^{15} in inertial confinement experiments while [28] gives the value of 6.10^{14} for laser plasma. Thus the electron skin depths range from 2.5×10^{-15} to 2.5×10^{-7} while the ion skin depths take values between 10^{-14} and 10^{-6} , correspondingly. Therefore the **electron and ion skin depths are always small in fusion plasma**.

Now let us introduce the non-dimensional version of the skin depths defined by:

$$(26) \quad \delta_e^* = \frac{\delta_e}{L_0}, \quad \delta_i^* = \frac{\delta_i}{L_0}.$$

Along these parameters and the choice (20) of the velocity scale, the non-dimensional momentum equation writes

$$(27) \quad \tilde{\partial}_t(\tilde{\rho}\tilde{\mathbf{u}}) + \tilde{\nabla} \cdot (\tilde{\rho}\tilde{\mathbf{u}} \otimes \tilde{\mathbf{u}}) + c_i \frac{(\delta_e^*)^2}{\beta} \tilde{\nabla} \cdot \left[\frac{1}{\tilde{n}} \tilde{\mathbf{J}} \otimes \tilde{\mathbf{J}} \right] + \frac{T_{e,0}}{T_{e,0} + T_{i,0}} \tilde{\nabla} \tilde{p}_e + \frac{T_{i,0}}{T_{e,0} + T_{i,0}} \tilde{\nabla} \tilde{p}_i = \frac{1}{\beta} \tilde{\mathbf{J}} \times \tilde{\mathbf{B}}.$$

This expression establishes that except for small β the factor in front of the quadratic term in the current in the equation (27) is small and therefore the current term can be neglected in this equation. Note that this result is valid independently of the mass ratio between electrons and ions. In particular, this result does not rely on the usual assumption that the electrons can be considered as massless. Actually, in the sequel, as we will consider large plasma β parameter, we do not need any assumption on the non-dimensional electron skin depth except that it is bounded.

The equation for the non-dimensional electron entropy variable $\tilde{S}_e = \tilde{\rho}_e^{-\gamma} \tilde{p}_e$, is given by

$$(28) \quad \tilde{\partial}_t(\tilde{\rho}_e \tilde{S}_e) + \tilde{\nabla} \cdot (\tilde{\rho}_e \tilde{S}_e \tilde{\mathbf{u}}) - \sqrt{c_i} \frac{\delta_i^*}{\sqrt{\beta}} \tilde{\nabla} \cdot \left[\frac{\tilde{\rho}_e \tilde{S}_e}{\tilde{n}} \tilde{\mathbf{J}} \right] = \tilde{\rho}_e^{1-\gamma} \left[\left(\frac{T_{i,0}}{T_{e,0}} \tilde{T}_i - \tilde{T}_e \right) \tilde{\nu}_{ei}^{\mathcal{E}} + (\gamma - 1) \zeta_{ei} \left(1 + \frac{T_{i,0}}{T_{e,0}} \right) \frac{(\delta_e^*)^2}{\beta} \tilde{\eta} \tilde{\mathbf{J}}^2 \right],$$

where the non-dimensional temperature relaxation coefficient is defined as

$$\tilde{\nu}_{ei}^{\mathcal{E}} = \frac{\tilde{n}}{\tilde{\tau}_{ei} + \tilde{\tau}_{ie}},$$

with $\tilde{\tau}_{ei} = \tau_{ei} u_0 / L_0$, and $\tilde{\tau}_{ie} = \tau_{ie} u_0 / L_0$ denoting the non-dimensional temperature relaxation times while the non-dimensional resistivity is

$$\tilde{\eta} = \frac{m_i}{\tilde{n}(\tilde{\tau}_{ie} m_e + \tilde{\tau}_{ei} m_i)}.$$

Its worth noticing that in this equation, ζ_{ei} does not change since it is dimensionless according its definition (18).

We now consider the total energy equation. With the choice of the velocity scaling (20), the kinetic energy is of the same order as the thermal energy and therefore we choose to define the non-dimensional total energy and the non-dimensional total energy by species by:

$$\mathcal{E} = n_0(m_e + m_i)u_0^2 \tilde{\mathcal{E}}, \quad \mathcal{E}_\alpha = n_0 k_B T_{\alpha,0} \tilde{\mathcal{E}}_\alpha, \quad \alpha = e, i.$$

The choice of a scale for the electric field is delicate. Faraday's law favours the use of the scaling

$$\mathbf{E} = B_0 u_0 \tilde{\mathbf{E}},$$

and this is the choice that is usually done in MHD. However, since Faraday's law involves the curl of \mathbf{E} , we see that the gradient part of \mathbf{E} (if it exists) has no reason to scale with $B_0 u_0$. To take this possibility into account, we will set

$$\mathbf{E} = \kappa B_0 u_0 \tilde{\mathbf{E}},$$

leaving for the present time the parameter κ unspecified.

With these choices, we obtain:

$$(29) \quad \begin{aligned} & \tilde{\partial}_t \left(\tilde{\mathcal{E}} + \frac{\tilde{\mathbf{B}}^2}{2\beta} \right) + \tilde{\nabla} \cdot \left[\left(\tilde{\mathcal{E}} + \frac{T_{e,0}}{T_{e,0} + T_{i,0}} \tilde{p}_e + \frac{T_{i,0}}{T_{e,0} + T_{i,0}} \tilde{p}_i \right) \tilde{\mathbf{u}} + \frac{\kappa \tilde{\mathbf{E}} \times \tilde{\mathbf{B}}}{\beta} \right] + \\ & \frac{1}{\sqrt{\beta}} \tilde{\nabla} \cdot \left[\left(\sqrt{c_e} \delta_e^* \frac{T_{i,0}}{T_{e,0} + T_{i,0}} (\tilde{p}_i + \tilde{\mathcal{E}}_i) - \sqrt{c_i} \delta_i^* \frac{T_{e,0}}{T_{e,0} + T_{i,0}} (\tilde{p}_e + \tilde{\mathcal{E}}_e) \right) \frac{\tilde{\mathbf{J}}}{\tilde{n}} \right] = 0. \end{aligned}$$

Once again, the terms containing the current are multiplied by expressions involving the skin depths.

It remains to consider the equation governing the evolution of the current. For the generalized Ohm's law, the same scaling procedure gives:

$$(30) \quad \begin{aligned} & \kappa \tilde{\mathbf{E}} + \tilde{\mathbf{u}} \times \tilde{\mathbf{B}} = (\delta_e^*)^2 \tilde{\eta} \tilde{\mathbf{J}} + \frac{\sqrt{c_i} \delta_i^* - \sqrt{c_e} \delta_e^*}{\sqrt{\beta}} \frac{\tilde{\mathbf{J}} \times \tilde{\mathbf{B}}}{\tilde{n}} \\ & - \sqrt{c_i} \delta_i^* \sqrt{\beta} \frac{T_{e,0}}{T_{e,0} + T_{i,0}} \frac{1}{\tilde{n}} \tilde{\nabla} \tilde{p}_e + \sqrt{c_e} \delta_e^* \sqrt{\beta} \frac{T_{i,0}}{T_{e,0} + T_{i,0}} \frac{1}{\tilde{n}} \tilde{\nabla} \tilde{p}_i \\ & + c_i (\delta_e^*)^2 \frac{1}{\tilde{n}} \left[\tilde{\partial}_t \tilde{\mathbf{J}} + \tilde{\nabla} \cdot (\tilde{\mathbf{u}} \otimes \tilde{\mathbf{J}} + \tilde{\mathbf{J}} \otimes \tilde{\mathbf{u}}) \right] + \sqrt{c_i} (c_i - c_e) \frac{(\delta_e^*)^2 \delta_i^*}{\sqrt{\beta}} \frac{1}{\tilde{n}} \tilde{\nabla} \cdot \left[\frac{1}{\tilde{n}} \tilde{\mathbf{J}} \otimes \tilde{\mathbf{J}} \right]. \end{aligned}$$

2.2.3. *Derivation of the two-temperature Euler plasma model.* We are now ready to show that the two-temperature Euler plasma model is an asymptotic limit of the two-fluid MHD model.

Although two different temperatures $T_{i,0}$ and $T_{e,0}$ are considered in the non-dimensional equations (27), (28), (29), we assume that these temperatures remain comparable and that the ratio $T_{i,0}/T_{e,0}$ remains bounded. We also assume that the non-dimensional parameters δ_i^* , δ_e^* and κ are bounded. When formally β tends to $+\infty$, in (27), (28), (29), we get:

$$(31) \quad \begin{aligned} & \tilde{\partial}_t (\tilde{\rho} \tilde{\mathbf{u}}) + \tilde{\nabla} \cdot (\tilde{\rho} \tilde{\mathbf{u}} \otimes \tilde{\mathbf{u}}) + \frac{T_{e,0}}{T_{e,0} + T_{i,0}} \tilde{\nabla} \tilde{p}_e + \frac{T_{i,0}}{T_{e,0} + T_{i,0}} \tilde{\nabla} \tilde{p}_i = 0, \\ & \tilde{\partial}_t (\tilde{\rho}_e \tilde{S}_e) + \tilde{\nabla} \cdot (\tilde{\rho}_e \tilde{S}_e \tilde{\mathbf{u}}) = \tilde{\rho}_e^{1-\gamma} \left[\left(\frac{T_{i,0}}{T_{e,0}} \tilde{T}_i - \tilde{T}_e \right) \tilde{v}_{ei}^{\mathcal{E}} \right], \\ & \tilde{\partial}_t \tilde{\mathcal{E}} + \tilde{\nabla} \cdot \left[\left(\tilde{\mathcal{E}} + \frac{T_{e,0}}{T_{e,0} + T_{i,0}} \tilde{p}_e + \frac{T_{i,0}}{T_{e,0} + T_{i,0}} \tilde{p}_i \right) \tilde{\mathbf{u}} \right] = 0. \end{aligned}$$

Immediately we recover the two-temperature Euler plasma model:

$$(32) \quad \begin{cases} \partial_t \rho + \nabla \cdot (\rho \mathbf{u}) = 0, \\ \partial_t (\rho \mathbf{u}) + \nabla \cdot (\rho \mathbf{u} \otimes \mathbf{u}) + \nabla (p_e + p_i) = 0, \\ \partial_t \mathcal{E} + \nabla \cdot [(\mathcal{E} + p_e + p_i) \mathbf{u}] = 0, \\ \partial_t (\rho_e S_e) + \nabla \cdot (\rho_e S_e \mathbf{u}) = \rho_e^{1-\gamma} (\gamma - 1) [v_{ei}^{\mathcal{E}} (T_i - T_e)]. \end{cases}$$

The system (32) has been obtained with the assumption that $\kappa/\beta \rightarrow 0$. In this case, we emphasize that (32) is a *closed* system: corresponding to the hypothesis of large β the electromagnetic energy becomes negligible with respect to the mechanical one. Moreover in the definition of the mechanical energy

$$(33) \quad \mathcal{E} = \frac{p_i + p_e}{\gamma - 1} + \frac{1}{2} \rho_i \mathbf{u}_i^2 + \frac{1}{2} \rho_e \mathbf{u}_e^2 = \frac{p_i + p_e}{\gamma - 1} + \frac{1}{2} \rho \mathbf{u}^2 + \frac{1}{2} \frac{m_e m_i}{m_e + m_i} \frac{\mathbf{J}^2}{ne^2},$$

the last term is of order $\mathcal{O}(c_i (\delta_e^*)^2 / \beta)$ and thus must be neglected.

Let us remark that to obtain (32), we do not need to consider Ohm's law (30). In this sense, (32) is independent of the precise form of Ohm's law that is used. However, if we check for consistency the behaviour of Ohm's law in the limit $\beta \rightarrow +\infty$, we will get at the higher order in β :

$$(34) \quad \kappa \tilde{\mathbf{E}} = -\sqrt{c_i} \delta_i^* \sqrt{\beta} \frac{T_{e,0}}{T_{e,0} + T_{i,0}} \frac{1}{\tilde{n}} \tilde{\nabla} \tilde{p}_e + \sqrt{c_e} \delta_e^* \sqrt{\beta} \frac{T_{i,0}}{T_{e,0} + T_{i,0}} \frac{1}{\tilde{n}} \tilde{\nabla} \tilde{p}_i,$$

and this relation establishes that the parameter κ (ratio between the electric field and the product $u_0 B_0$) has to scale with $\delta_i^* \sqrt{\beta}$ in the $\beta \rightarrow +\infty$ limit. Therefore the ratio $\kappa/\beta \rightarrow 0$ when $\beta \rightarrow +\infty$ and the scaling is self-consistent. For completeness, the non-dimensional version of (34) is given:

$$(35) \quad \mathbf{E} = \frac{1}{ne} (c_e \nabla p_i - c_i \nabla p_e).$$

Note also that in this derivation of (32), we have never used any assumption on the electron mass. This system is therefore also relevant in the case where instead of electrons, a mixture of positive and negative ions is considered. However, in this case, there is no definite reason to choose the electron entropy equation to close the system and

another choice can be more physically relevant.

The system (32) can be also established using different assumptions. In [1], a two-fluid model in the absence of any magnetic field is considered with the assumption that the two species have the same velocity. Then the comparison of the momentum equations from (1) (with $\mathbf{u}_e = \mathbf{u}_i = \mathbf{u}$) implies Ohm's law (35) from which a non-conservative system equivalent for smooth solutions to (32) is derived. The same assumptions (with in addition $m_e = 0$) is also used in [13].

System (32) is also considered in [32], with the assumption that the electron mass is small. The derivation we have presented here seems more general and does not rely on the strong assumptions of the absence of current and magnetic field, nor that the two species have the same velocities. It only requires quasi-neutrality and that the magnetic effects are weak.

2.3. Mathematical properties of the two-temperature Euler plasma model. We now turn to address mathematical properties of the two-temperature Euler plasma model. A mathematical study of the multi-fluid system with the equation on the electron entropy was also presented in [13]. Since the two-temperature Euler plasma system is Galilean invariant, we restrict our study to its 1D version in the x -direction, which reads:

$$(36) \quad \begin{cases} \partial_t \rho + \partial_x(\rho u) & = 0, \\ \partial_t(\rho u) + \partial_x(\rho u^2 + p_e + p_i) & = 0, \\ \partial_t(\rho v) + \partial_x(\rho uv) & = 0, \\ \partial_t(\rho w) + \partial_x(\rho uw) & = 0, \\ \partial_t \mathcal{E} + \partial_x[(\mathcal{E} + p_e + p_i)u] & = 0, \\ \partial_t(\rho_e S_e) + \partial_x(\rho_e S_e u) & = (\gamma - 1)\nu_{ei}^\mathcal{E} \rho_e^{1-\gamma}(T_i - T_e), \end{cases}$$

where the velocity is given by: $\mathbf{u} = (u, v, w)^T$ in the canonical base of \mathbb{R}^3 .

Introducing the notations

$$\mathcal{W} = \begin{pmatrix} \rho \\ \rho u \\ \rho v \\ \rho w \\ \mathcal{E} \\ \rho_e S_e \end{pmatrix}, \quad \mathcal{F}(\mathcal{W}) = \begin{pmatrix} \rho u \\ \rho u^2 + p_i + p_e \\ \rho uv \\ \rho w \\ (\mathcal{E} + p_i + p_e)u \\ \rho_e S_e u \end{pmatrix}, \quad \mathcal{S}(\mathcal{W}) = \begin{pmatrix} 0 \\ 0 \\ 0 \\ 0 \\ 0 \\ (\gamma - 1)\nu_{ei}^\mathcal{E} \rho_e^{1-\gamma}(T_i - T_e) \end{pmatrix},$$

allows to write the system (36) as:

$$(37) \quad \partial_t \mathcal{W} + \partial_x \mathcal{F}(\mathcal{W}) = \mathcal{S}(\mathcal{W}).$$

Let us note that the solution \mathcal{W} of either (36) or (37) belongs to the set of *physically admissible states* \mathcal{O} defined by:

$$\mathcal{O} = \left\{ \mathcal{W} = (\rho, \rho \mathbf{u}, \mathcal{E}, \rho_e S_e)^T \in \mathbb{R}^6, \quad \rho > 0, \quad \mathcal{E} - \frac{1}{2}\rho \mathbf{u}^2 > 0, \quad S_e > 0, \quad \rho_e = c_e \rho \right\}.$$

The Jacobian matrix $A(\mathcal{W}) = \partial_{\mathcal{W}} F(\mathcal{W})$, important to determine the eigenstructure of (37), is given by:

$$A(\mathcal{W}) = \begin{pmatrix} 0 & 1 & 0 & 0 & 0 & 0 \\ \frac{\gamma-3}{2}u^2 + \frac{\gamma-1}{2}(v^2 + w^2) & (3-\gamma)u & (1-\gamma)v & (1-\gamma)w & \gamma-1 & 0 \\ -uw & v & u & 0 & 0 & 0 \\ -uw & w & 0 & u & 0 & 0 \\ u \left[-\frac{c_s^2}{\gamma-1} + \frac{\gamma-2}{2}(u^2 + v^2 + w^2) \right] & \frac{c_s^2}{\gamma-1} + \frac{3-2\gamma}{2}u^2 + \frac{v^2+w^2}{2} & (1-\gamma)uv & (1-\gamma)uw & \gamma u & 0 \\ -c_e S_e u & c_e S_e & 0 & 0 & 0 & u \end{pmatrix}.$$

A direct computation shows that the matrix $A(\mathcal{W})$ owns the eigenvalues $\lambda_1 = u - c_s$, $\lambda_2 = \lambda_3 = \lambda_4 = \lambda_5 = u$, $\lambda_6 = u + c_s$, where c_s is the sound speed of the mixture

$$c_s = \sqrt{\gamma \frac{p_e + p_i}{\rho}}.$$

The associated eigenvectors are given by

$$(38) \quad \left\{ \begin{array}{l} R_1 = \begin{pmatrix} 1 \\ u - c_s \\ v \\ w \\ \frac{c_s^2}{\gamma - 1} + \frac{u^2 + v^2 + w^2}{2} - uc_s \\ c_e S_e \end{pmatrix}, \\ R_2 = \begin{pmatrix} 1 \\ u \\ v \\ \frac{u^2 + v^2 + w^2}{2} \\ 1 \end{pmatrix}, \\ R_6 = \begin{pmatrix} 1 \\ u + c_s \\ v \\ w \\ \frac{c_s^2}{\gamma - 1} + \frac{u^2 + v^2 + w^2}{2} + uc_s \\ c_e S_e \end{pmatrix}. \end{array} \right. \quad R_3 = \begin{pmatrix} 0 \\ 0 \\ 1 \\ 0 \\ v \\ 1 \end{pmatrix}, \quad R_4 = \begin{pmatrix} 0 \\ 0 \\ 0 \\ 1 \\ w \\ 1 \end{pmatrix}, \quad R_5 = \begin{pmatrix} 0 \\ 0 \\ 0 \\ 0 \\ 0 \\ 1 \end{pmatrix},$$

The system $\partial_t \mathcal{U} + \partial_x \mathcal{F}(\mathcal{U}) = 0$ is hyperbolic. Straightforward computations prove that the characteristic fields associated to the eigenvalues $u \pm c_s$ are genuinely nonlinear while the characteristic fields associated to the eigenvalue u are linearly degenerated [24, 33, 13].

3. NUMERICAL APPROXIMATION OF THE TWO-TEMPERATURE EULER EQUATIONS

We aim in this section at presenting a numerical approximation to simulate the two-temperature Euler model in a toroidal geometry. This numerical strategy is finite volume-type where a relaxation scheme is designed to compute the corresponding numerical flux.

3.1. The two-temperature Euler equations in a toroidal geometry. In either tokamak device plasmas or astrophysical ones the charged particles move in a torus, so that choosing a toroidal geometry for the investigation of their dynamics is realist. A torus can be practically considered as a solid of revolution generated by a rotation of a poloidal plane about an axis. The axisymmetric feature of a torus then makes pertinent to use cylindrical coordinates for describing plasma properties. The designed numerical method suggested in the paper exploits this feature and will be exposed later on. For the moment, we set the analytical foundation of the proposed numerical approximation that consists in writing the two-temperature Euler equations in cylindrical coordinates and addressing the consequences of this choice.

Let us recall that the Cartesian coordinates of a torus point $\mathbf{x} = (x, y, z)^T$ are linked to its cylindrical coordinates $(R, Z, \varphi)^T$ by:

$$(39) \quad \begin{cases} x = R \cos \varphi, \\ y = R \sin \varphi, \\ z = Z, \end{cases}$$

where: $R > 0$, $0 \leq \varphi < 2\pi$, and $Z \in \mathbb{R}$. The mapping $\Psi : \mathbb{R}^3 \rightarrow \mathbb{R}^3$, $\mathbf{x} = (x, y, z)^T \mapsto (R, Z, \varphi)^T$ leads to the following covariant basis:

$$(40) \quad \begin{cases} \mathbf{e}_R = \frac{\partial x}{\partial R} \mathbf{i} + \frac{\partial y}{\partial R} \mathbf{j} + \frac{\partial z}{\partial R} \mathbf{k}, \\ \mathbf{e}_\varphi = \frac{\partial x}{\partial \varphi} \mathbf{i} + \frac{\partial y}{\partial \varphi} \mathbf{j} + \frac{\partial z}{\partial \varphi} \mathbf{k}, \\ \mathbf{e}_Z = \frac{\partial x}{\partial Z} \mathbf{i} + \frac{\partial y}{\partial Z} \mathbf{j} + \frac{\partial z}{\partial Z} \mathbf{k}, \end{cases}$$

where $(\mathbf{i}, \mathbf{j}, \mathbf{k})$ is the canonical base of \mathbb{R}^3 . The Jacobian determinant of Ψ is: $\mathbf{e}_R \cdot (\mathbf{e}_\varphi \times \mathbf{e}_Z) = R > 0$, which means that the transformation Ψ is one-to-one. The scaled covariant basis is useful and is given by:

$$(41) \quad \widetilde{\mathbf{e}}_R = \mathbf{e}_R / |\mathbf{e}_R| = \mathbf{e}_R, \quad \widetilde{\mathbf{e}}_\varphi = \mathbf{e}_\varphi / |\mathbf{e}_\varphi| = \mathbf{e}_\varphi / R, \quad \widetilde{\mathbf{e}}_Z = \mathbf{e}_Z / |\mathbf{e}_Z| = \mathbf{e}_Z.$$

It is also worthwhile to define the contravariant basis associated to the transformation Ψ . The contravariant basis $(\mathbf{e}^R, \mathbf{e}^Z, \mathbf{e}^\varphi)$ is defined by duality relations:

$$(42) \quad \mathbf{e}_k \cdot \mathbf{e}^\ell = \delta_k^\ell,$$

where δ_k^ℓ is the Kronecker's symbol, and: $k, \ell = R, Z, \varphi$.

If one writes the equations of system (36) in cylindrical coordinates without precautions, their conservative form is susceptible to being lost, leading to artificial source terms which numerical approximation could be difficult. However, in [9], it is proved that it is possible to write the equations of system (36) in cylindrical coordinates in order to keep their conservative form. Typically, following the procedure suggested in [9], the equations of system (36) in cylindrical coordinates now write:

$$(43) \quad \begin{cases} \partial_t(R\rho) + \partial_{\xi_k}(R\rho\mathbf{u} \cdot \mathbf{e}^k) & = & 0, \\ \partial_t(R\rho\mathbf{u}) + \partial_{\xi_k}(R\mathbf{T} \cdot \mathbf{e}^k) & = & 0, \\ \partial_t(R\mathcal{E}) + \partial_{\xi_k}(R(\mathcal{E} + p_i + p_e)\mathbf{u} \cdot \mathbf{e}^k) & = & 0, \\ \partial_t(R\rho_e S_e) + \partial_{\xi_k}(R\rho_e S_e \mathbf{u} \cdot \mathbf{e}^k) & = & R(\gamma - 1)\nu_{ei}^\mathcal{E} \rho_e^{1-\gamma_e}(T_i - T_e), \end{cases}$$

where Einstein's convention on repetitive summation is assumed, and ∂_{ξ_k} represents derivatives with respect to R , Z , and φ variables, accordingly. The tensor \mathbf{T} is defined by: $\mathbf{T} = T^{k\ell} \widetilde{\mathbf{e}}_k \otimes \widetilde{\mathbf{e}}_\ell$, where: $T^{k\ell} = \rho u_k u_\ell + (p_i + p_e) \delta_k^\ell$. Obviously, (43) retains the conservative form of the two-temperature Euler plasma model in cylindrical coordinates. The equations of system (43) can be cast in the following compact form:

$$(44) \quad \partial_t(R\mathcal{U}) + \partial_{\xi_k}(R\mathcal{G}(\mathcal{U}) \cdot \mathbf{e}^k) = R\mathcal{S}(\mathcal{U}),$$

where

$$\mathcal{G}(\mathcal{U}) \cdot \mathbf{e}^k = \begin{pmatrix} \rho\mathbf{u} \cdot \mathbf{e}^k \\ \mathbf{T} \cdot \mathbf{e}^k \\ (\mathcal{E} + p_i + p_e)\mathbf{u} \cdot \mathbf{e}^k \\ \rho_e S_e \mathbf{u} \cdot \mathbf{e}^k \end{pmatrix}.$$

3.2. Adaptation of finite volume method in toroidal geometry. We are ready to present the numerical method designed in this work to approximate the numerical solution of the two-temperature Euler equations in cylindrical coordinates for a toroidal geometry (44). It is an adaptation of finite volume method based on our previous works [9, 8].

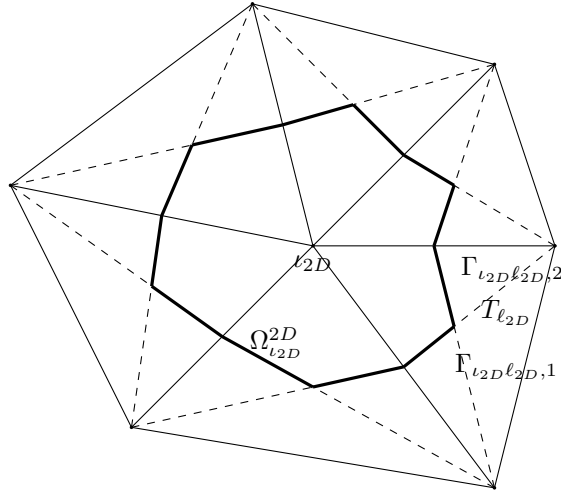
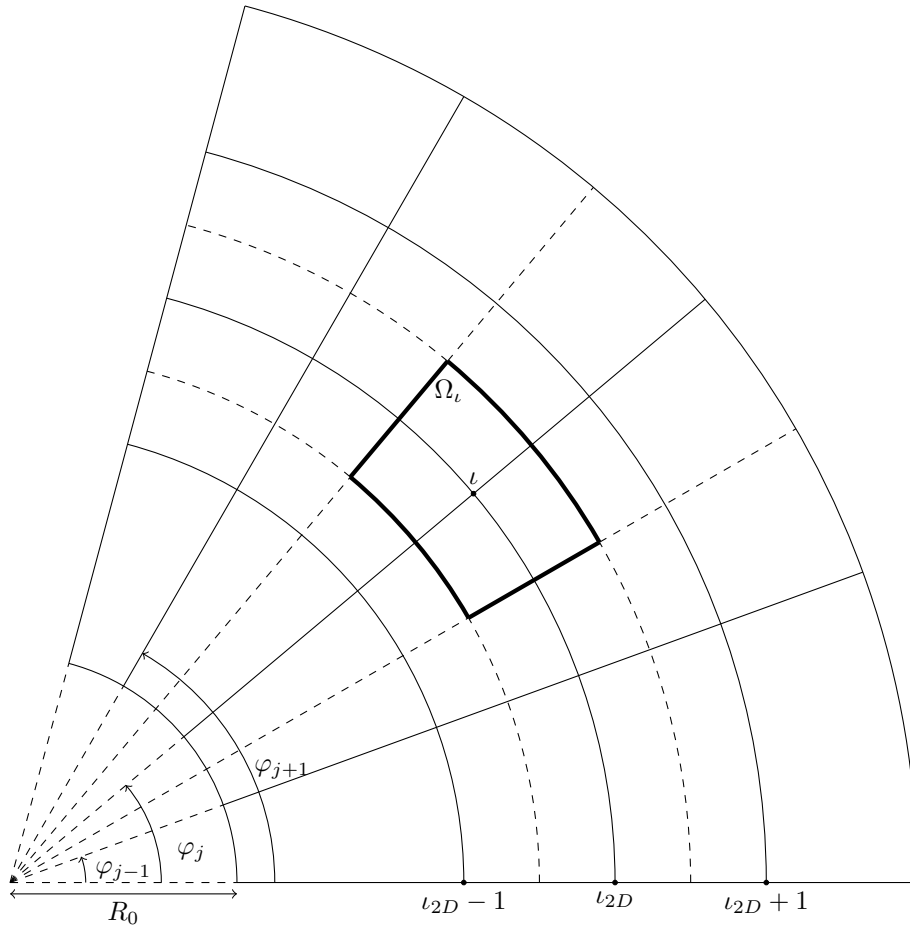
Now, we are concerned with the mesh used in the suggested numerical method that takes into account the axisymmetric feature of the tokamak geometry thanks to cylindrical coordinates. The generation of such a mesh proceeds as follows. First, an unstructured 2D dual mesh is generated for the poloidal plane (R, Z) , whose geometry could be quite complex. The tessellation of the considered poloidal plane consists of N_t triangles.

Let $T_{\iota_{2D}}$ be the ι_{2D} th triangle. The ι_{2D} th control cell $\Omega_{\iota_{2D}}^{2D}$, associated to ι_{2D} th vertex is given by

$$(45) \quad \Omega_{\iota_{2D}}^{2D} = \bigcup_{\ell_{2D}} \Omega_{\ell_{2D}}^{2D(\ell_{2D})},$$

where the union covers to all the triangles sharing the ι_{2D} th vertex and $\Omega_{\ell_{2D}}^{2D(\ell_{2D})}$ denotes the subset of $T_{\ell_{2D}}$ which is defined by further dividing $T_{\ell_{2D}}$ into six sub-triangles by means of its medians and subsequently considering those two sub-triangles which share the ι_{2D} th vertex (see Figure 1). As shown in Figure 1, the interface between the ι_{2D} th cell and the ℓ_{2D} th cell is made up of two segments $\Gamma_{\iota_{2D}\ell_{2D},1}$ and $\Gamma_{\iota_{2D}\ell_{2D},2}$. Second, once a 2D mesh is constructed, the 3D mesh is obtained by the revolution of the poloidal tessellation about the axis of revolution. Practically, the interval $[0, \Phi_0]$ where $0 < \Phi_0 \leq 2\pi$ is divided into N_{plan} segments defined by the endpoints $(\varphi_{1/2}, \varphi_{3/2}, \dots, \varphi_{N_{plan}+1/2})$ (the angle Φ_0 represents the end of the section of the torus in the φ -direction to discretize, and we implicitly assume that $\varphi_{N_{plan}+1/2} = \varphi_{1/2}$ in the case $\Phi_0 = 2\pi$). Then each 2D control cell $\Omega_{\iota_{2D}}^{2D}$ yields N_{plan} 3D control cells Ω_ι obtained as the rotations about the revolution axis between the angles $\varphi_{j-1/2}, \varphi_{j+1/2}$, where $j = 1, \dots, N_{plan}$. A similar construction holds true for the triangles of the 2D mesh. It is worth noticing that the boundary of the generic control cell Ω_ι can be split into two kinds of surfaces, the poloidal surfaces S^{pol} and the toroidal ones, S^{tor} . The poloidal surfaces are obtained by the revolution of the segments $\Gamma_{\iota_{2D}\ell_{2D},1}$ and $\Gamma_{\iota_{2D}\ell_{2D},2}$ of the poloidal mesh. The toroidal surfaces are always two and are the images of the revolved 2D control cell. From now on, a 3D control cell Ω_ι is uniquely referred by the integers ι_{2D} and $j = 1, \dots, N_{plan}$ such that Ω_ι is obtained as the rotations about the revolution axis between the angles $\varphi_{j-1/2}, \varphi_{j+1/2}$ of the 2D control cell $\Omega_{\iota_{2D}}^{2D}$. The integer ι_{2D} belongs to the set $\{1, \dots, N_{2D}\}$ where N_{2D} is the total number of 2D control cells. In particular, given the integers ι_{2D} in $\{1, \dots, N_{2D}\}$ and j in $\{1, \dots, N_{plan}\}$, the integer ι is determined by a global numbering procedure of the 3D control cells, for instance:

$$(46) \quad \iota = (\iota_{2D} - 1)N_{plan} + j.$$

FIGURE 1. Representation of a control cell $\Omega_{\ell_{2D}}^{2D}$ in the (R, Z) -plane.FIGURE 2. Projection of the Ω_{ℓ} cell control on $\tilde{\mathbf{e}}_{\varphi}$.

We now focus on the finite volume method devised to compute the numerical solution of (44) on the above tessellation describing the tokamak geometry. We use the finite volume method addressed in [9, 8], known as discretization-projection method. This method proceeds as follows.

Equations (44) are integrated over the 3D control cell Ω_{ℓ} with respect to the Lebesgue measure $d\Omega = dR dZ d\varphi$. The results can be cast into two kinds of equations. The first one concerned scalar equations such as those of mass, energy, and entropy. Its generic form is the following:

$$(47) \quad |\Omega_{\ell}| \partial_t V_{\ell} + \int_{\Omega_{\ell}} \partial_{\xi^k} (\mathbf{G} \cdot \mathbf{e}^k) d\Omega = \int_{\Omega_{\ell}} R \mathcal{S}_V d\Omega,$$

where $V_\iota = \frac{1}{|\Omega_\iota|} \int_{\Omega_\iota} RV \, d\Omega$, and V is both the mass, energy, and entropy, and \mathbf{G} is its physical flux accordingly.

The source term \mathcal{S}_V vanishes when V is either the mass or the energy while $\mathcal{S} = \nu_{ei}^\mathcal{E} \rho_e^{1-\gamma_e} (T_i - T_e)$ if V is the entropy. The quantity $|\Omega_\iota|$ represents the volume of the 3D control cell Ω_ι , and is given in the appendix A.

The second kind of equations deals with the vectorial one, the momentum equation is typically an example. It writes:

$$(48) \quad |\Omega_\iota| \partial_t \left(\frac{1}{|\Omega_\iota|} \int_{\Omega_\iota} R \rho \mathbf{u} \, d\Omega \right) + \int_{\Omega_\iota} \partial_{\xi^k} (R \mathbf{T} \cdot \mathbf{e}^k) \, d\Omega = 0.$$

From practical issue, we are then lead to choose which kind of components of the vector $\frac{1}{|\Omega_\iota|} \int_{\Omega_\iota} R \rho \mathbf{u} \, d\Omega$ will be stored in order to represent it. According to [9], the components of the vector \mathbf{u}_ι with respect to the local basis $(\widetilde{\mathbf{e}}_R(\iota), \widetilde{\mathbf{e}}_Z(\iota), \widetilde{\mathbf{e}}_\varphi(\iota))$ of the control cell Ω_ι are stored, which automatically lead to:

$$(49) \quad \frac{1}{|\Omega_\iota|} \int_{\Omega_\iota} R \rho \mathbf{u} \, d\Omega = \rho_\iota \left(\tilde{\eta}_\iota u_{R,\iota} \widetilde{\mathbf{e}}_R(\iota) + u_{Z,\iota} \widetilde{\mathbf{e}}_Z(\iota) + \tilde{\eta}_\iota u_{\varphi,\iota} \widetilde{\mathbf{e}}_\varphi(\iota) \right),$$

with: $\mathbf{u}_\iota = u_{R,\iota} \widetilde{\mathbf{e}}_R(\iota) + u_{Z,\iota} \widetilde{\mathbf{e}}_Z(\iota) + u_{\varphi,\iota} \widetilde{\mathbf{e}}_\varphi(\iota)$, $\tilde{\eta}_\iota = \frac{\sin\left(\frac{\varphi_{\iota+1/2} - \varphi_{\iota-1/2}}{2}\right)}{\varphi_{\iota+1/2} - \varphi_{\iota-1/2}}$, where $\varphi_{\iota-1/2}$ and $\varphi_{\iota+1/2}$ are the angles

that bound the cell Ω_ι in the φ -direction. We recall that $(\widetilde{\mathbf{e}}_R(\iota), \widetilde{\mathbf{e}}_Z(\iota), \widetilde{\mathbf{e}}_\varphi(\iota))$ is the covariant basis at the center ι of the control cell Ω_ι referred by i_{2D} and j , and where $\widetilde{\mathbf{e}}_Z(\iota) = \mathbf{e}_Z(\iota) = \mathbf{e}_Z = \mathbf{e}_z$ since the unit vector along the Z -direction remains unchanged.

Defining the vectorial quantity: $\eta_\iota \mathbf{u}_\iota = \tilde{\eta}_\iota u_{R,\iota} \widetilde{\mathbf{e}}_R(\iota) + u_{Z,\iota} \widetilde{\mathbf{e}}_Z(\iota) + \tilde{\eta}_\iota u_{\varphi,\iota} \widetilde{\mathbf{e}}_\varphi(\iota)$, enables us to rewrite equation (48) as:

$$(50) \quad |\Omega_\iota| \partial_t (\rho_\iota \eta_\iota \mathbf{u}_\iota) + \int_{\Omega_\iota} \partial_{\xi^k} (R \mathbf{T} \cdot \mathbf{e}^k) \, d\Omega = 0.$$

It follows that the above discretization-projection finite volume method leads to the following semi-discrete scheme:

$$(51) \quad |\Omega_\iota| \partial_t \begin{pmatrix} \rho_\iota \\ \rho_\iota \eta_\iota \mathbf{u}_\iota \\ \mathcal{E}_\iota \\ \rho_{e,\iota} \mathcal{S}_{e,\iota} \end{pmatrix} + \sum_{S_{i\ell} \in \mathcal{S}^{pol}} \int_{S_{i\ell}} (R \mathcal{G}(\mathcal{U}) \cdot \mathbf{e}^k) (\mathbf{n} \cdot \mathbf{e}^k) \, d\partial\Omega_{i\ell} + \sum_{S_{i\ell} \in \mathcal{S}^{tor}} \int_{S_{i\ell}} (R \mathcal{G}(\mathcal{U}) \cdot \mathbf{e}^k) (\mathbf{n} \cdot \mathbf{e}^k) \, d\partial\Omega_{i\ell} \\ = \int_{\Omega_\iota} \begin{pmatrix} 0 \\ \mathbf{0} \\ 0 \\ R(\gamma - 1) \nu_{ei}^\mathcal{E} \rho_e^{1-\gamma_e} (T_i - T_e) \end{pmatrix} \, d\Omega,$$

where \mathcal{S}^{pol} and \mathcal{S}^{tor} are the set of the poloidal and toroidal surfaces that constitute the boundary faces of Ω_ι . The face $S_{i\ell}$ is the interface between the control cells ι and ℓ . The physical flux $\int_{S_{i\ell}} (R \mathcal{G}(\mathcal{U}) \cdot \mathbf{e}^k) (\mathbf{n} \cdot \mathbf{e}^k) \, d\partial\Omega_{i\ell}$ are approached as follows:

$$(52) \quad \int_{S_{i\ell}} (R \mathcal{G}(\mathcal{U}) \cdot \mathbf{e}^k) (\mathbf{n} \cdot \mathbf{e}^k) \, d\partial\Omega \approx |S_{i\ell}| \mathbf{F}(\mathcal{U}_\iota, \mathcal{U}_\ell, \mathbf{n}_{i\ell}) \cdot \left[\frac{1}{|S_{i\ell}|} \int_{S_{i\ell}} R \mathbf{e}^k (\mathbf{n} \cdot \mathbf{e}^k) \, d\partial\Omega_{i\ell} \right],$$

where $\mathbf{F}(\mathcal{U}_\iota, \mathcal{U}_\ell, \mathbf{n}_{i\ell})$ is the numerical flux across the interface $S_{i\ell}$, $\mathcal{U}_\iota = \begin{pmatrix} \rho_\iota \\ \rho_\iota \mathbf{u}_\iota \\ \mathcal{E}_\iota \\ \rho_{e,\iota} \mathcal{S}_{e,\iota} \end{pmatrix}$ and $\mathcal{U}_\ell = \begin{pmatrix} \rho_\ell \\ \rho_\ell \mathbf{u}_\ell \\ \mathcal{E}_\ell \\ \rho_{e,\ell} \mathcal{S}_{e,\ell} \end{pmatrix}$ are

the vector states in the control cells Ω_ι and Ω_ℓ respectively, and $\mathbf{n}_{i\ell}$ is a local unit outward normal of the interface $S_{i\ell}$, pointing from ι to ℓ . For the sake of self-consistency and the clarity of the paper, the computations of the normals $\mathbf{n}_{i\ell} = \frac{\int_{S_{i\ell}} \mathbf{e}^k R (\mathbf{n} \cdot \mathbf{e}^k) \, d\partial\Omega_{i\ell}}{\|\int_{S_{i\ell}} \mathbf{e}^k R (\mathbf{n} \cdot \mathbf{e}^k) \, d\partial\Omega_{i\ell}\|}$, and the quantities $\mathbf{N}_{i\ell} = \frac{\int_{S_{i\ell}} \mathbf{e}^k R (\mathbf{n} \cdot \mathbf{e}^k) \, d\partial\Omega_{i\ell}}{|S_{i\ell}|}$ are addressed in the appendix A. Since $\mathbf{e}^k (\mathbf{n} \cdot \mathbf{e}^k) = \mathbf{n}$, actually $\mathbf{n}_{i\ell}$ is an average unit outward normal of the interface $S_{i\ell}$:

$$(53) \quad \mathbf{n}_{i\ell} = \frac{\int_{S_{i\ell}} \mathbf{n} R \, d\partial\Omega_{i\ell}}{\|\int_{S_{i\ell}} \mathbf{n} R \, d\partial\Omega_{i\ell}\|}, \quad \mathbf{N}_{i\ell} = \frac{\int_{S_{i\ell}} \mathbf{n} R \, d\partial\Omega_{i\ell}}{|S_{i\ell}|}.$$

The calculation of the numerical flux $\mathbf{F}(\mathcal{U}_\iota, \mathcal{U}_\ell, \mathbf{n}_{i\ell})$ is provided by a relaxation scheme, that constitutes the matter of the next section as well as the right hand side of (51). In order to illustrate the scheme (51), we give its declination

for the explicit time integration:

$$(54) \quad \begin{pmatrix} \rho_\iota^{n+1} \\ \rho_\iota^{n+1} \eta_\iota \mathbf{u}_\iota^{n+1} \\ \mathcal{E}_\iota^{n+1} \\ \rho_{e,\iota}^{n+1} S_{e,\iota}^{n+1} \end{pmatrix} = \begin{pmatrix} \rho_\iota^n \\ \rho_\iota^n \eta_\iota \mathbf{u}_\iota^n \\ \mathcal{E}_\iota^n \\ \rho_{e,\iota}^n S_{e,\iota}^n \end{pmatrix} - \frac{\Delta t}{|\Omega_\iota|} |\Omega_{\iota 2D}^{2D}| \left(\mathbf{F}(\mathcal{U}_\iota^n, \mathcal{U}_{\iota_+}^n, \widetilde{\mathbf{e}_\varphi(\iota_+)}) \cdot \widetilde{\mathbf{e}_\varphi(\iota_+)} - \mathbf{F}(\mathcal{U}_{\iota_-}^n, \mathcal{U}_\iota^n, \widetilde{\mathbf{e}_\varphi(\iota_-)}) \cdot \widetilde{\mathbf{e}_\varphi(\iota_-)} \right) \\ - \frac{\Delta t}{|\Omega_\iota|} \sum_{S_{i\ell} \in \mathcal{S}^{pol}} |S_{i\ell}| \mathbf{F}(\mathcal{U}_\iota^n, \mathcal{U}_\ell^n, \mathbf{n}_{i\ell}) \cdot \mathbf{N}_{i\ell} + \frac{\Delta t}{|\Omega_\iota|} \int_{\Omega_\iota} \begin{pmatrix} 0 \\ \mathbf{0} \\ 0 \\ R(\gamma - 1) \nu_{ei}^\mathcal{E} (\rho_e^n)^{1-\gamma_e} (T_i^n - T_e^n) \end{pmatrix} d\Omega,$$

where ι_- and ι_+ are the left and right neighbours of ι in the φ -direction. For example, assume ι is determined by the global numbering (46), then $\iota_+ = \iota + Nplan$, and $\iota_- = \iota - Nplan$.

3.3. A relaxation scheme for the two-temperature Euler equations. Consider two control cells ι and ℓ sharing the interface $S_{i\ell}$ whose unit normal pointing from ι to ℓ is denoted by $\mathbf{n}_{i\ell}$. The numerical flux $\mathbf{F}(\mathcal{U}_\iota, \mathcal{U}_\ell, \mathbf{n}_{i\ell})$ across the interface $S_{i\ell}$ along $\mathbf{n}_{i\ell}$, that intervenes in (52), could be computed by considering a Riemann problem of the projection of system (44) onto the vector $\mathbf{n}_{i\ell}$, which writes:

$$(55) \quad \partial_t(R\mathcal{U}) + \partial_\zeta(R\mathcal{H}(\mathcal{U})) = R\mathcal{S},$$

where $\zeta = \xi \cdot \mathbf{n}_{i\ell}$, with $\xi = \xi_k \mathbf{e}^k$, and

$$(56) \quad \mathcal{H}(\mathcal{U}) = (\mathcal{G}(\mathcal{U}) \cdot \mathbf{e}^k) \cdot \mathbf{n}_{i\ell}.$$

The initial data is constant on either side of the straight line $\zeta = 0$.

The resulting system is 1D in the $\mathbf{n}_{i\ell}$ -direction. According to Galilean invariance of the system (44), it is deemed appropriate to compute the numerical solution of the 1D problem (32). A relaxation scheme is then proposed in this framework.

3.3.1. A relaxation scheme for the two-temperature Euler equations in 1D. Following [1, 6, 10], a Suliciu relaxation-type model of the 1D system (32) is introduced, which writes:

$$(57) \quad \left\{ \begin{array}{l} \partial_t \rho + \partial_x(\rho u) = 0, \\ \partial_t(\rho u) + \partial_x(\rho u^2 + (\pi_e + \pi_i)) = 0, \\ \partial_t(\rho v) + \partial_x(\rho uv) = 0, \\ \partial_t(\rho w) + \partial_x(\rho uw) = 0, \\ \partial_t(\mathcal{E}) + \partial_x((\mathcal{E} + \pi_i + \pi_e)u) = 0, \\ \partial_t(\rho_e S_e) + \partial_x(\rho_e S_e u) = (\gamma - 1) \nu_{ei}^\mathcal{E} \rho_e^{1-\gamma_e} (T_i - T_e), \\ \partial_t(\rho \pi_e + c_e a^2) + \partial_x(\rho \pi_e u + c_e a^2 u) = \frac{1}{\tau} \rho (p_e - \pi_e), \\ \partial_t(\rho \pi_i + c_i a^2) + \partial_x(\rho \pi_i u + c_i a^2 u) = \frac{1}{\tau} \rho (p_i - \pi_i), \\ \partial_t(\rho a) + \partial_x(\rho a u) = 0, \end{array} \right.$$

where π_i and π_e are the relaxed pressures, τ is the relaxed parameter. As soon as τ tends to 0, the pressures p_i and p_e are recovered. The parameter a allows to bound adequately the Riemann problem wave velocities coming from the Suliciu relaxation model (57). The parameter a is submitted to the so-called Whitham subcharacteristic condition that will be given later on. The presence of the source term $(\gamma - 1) \nu_{ei}^\mathcal{E} \rho_e^{1-\gamma_e} (T_i - T_e)$ in (57) is its main difference with the other Suliciu relaxation models encountered in the literature.

For simplicity, the following state, flux, relaxation and source vectors are introduced:

$$(58) \quad \mathbb{U} = \begin{pmatrix} \rho \\ \rho u \\ \rho v \\ \rho w \\ \mathcal{E} \\ \rho_e S_e \\ \rho \pi_i + c_i a^2 \\ \rho \pi_e + c_e a^2 \\ \rho a \end{pmatrix}, \quad \mathbb{F}(\mathbb{U}) = \begin{pmatrix} \rho u \\ \rho u^2 + \pi_i + \pi_e \\ \rho v u \\ \rho w u \\ (\mathcal{E} + \pi_i + \pi_e) u \\ \rho_e S_e u \\ \rho \pi_i u + c_i a^2 u \\ \rho \pi_e u + c_e a^2 u \\ \rho a u \end{pmatrix}, \quad \mathbb{T}_\tau(\mathbb{U}) = \begin{pmatrix} 0 \\ 0 \\ 0 \\ 0 \\ 0 \\ (\gamma - 1) \nu_{ei}^\mathcal{E} \rho_e^{1-\gamma_e} (T_i - T_e) \\ \frac{1}{\tau} \rho (p_i - \pi_i) \\ \frac{1}{\tau} \rho (p_e - \pi_e) \\ 0 \end{pmatrix}.$$

The model (57) then writes in the following compact form:

$$(59) \quad \partial_t \mathbb{U} + \partial_x \mathbb{F}(\mathbb{U}) = \mathbb{T}_\tau(\mathbb{U}).$$

The following result can be then stated.

Theorem 1. *The system (59) without the relaxation $\mathbb{T}_\tau(\mathbb{U})$, is hyperbolic. The eigenvalues are given by the set*

$$(60) \quad \Lambda = \left\{ u - \frac{a}{\rho}, u, u, u, u, u, u + \frac{a}{\rho} \right\}.$$

All the associated characteristic fields are linearly degenerated.

Proof. Straightforward computations [1, 24, 33, 13, 6] lead to the proof of the above theorem. \square

For simplicity, we introduce the following space:

$$\mathcal{V} = \left\{ \mathbb{U} = (\rho, \rho u, \rho v, \rho w, \mathcal{E}, \rho_e S_e, \rho \pi_i + c_i a^2, \rho \pi_e + c_e a^2, \rho a)^T \in \mathbb{R}^9, \rho > 0, \rho_e = c_e \rho \right\}.$$

It is related to the space \mathcal{O} by: $\mathcal{N}\mathcal{V} \supseteq \mathcal{O}$, where \mathcal{N} is the projection matrix of rank 6 defined by:

$$\mathcal{N} = \begin{pmatrix} 1 & 0 & 0 & 0 & 0 & 0 & 0 & 0 & 0 \\ 0 & 1 & 0 & 0 & 0 & 0 & 0 & 0 & 0 \\ 0 & 0 & 1 & 0 & 0 & 0 & 0 & 0 & 0 \\ 0 & 0 & 0 & 1 & 0 & 0 & 0 & 0 & 0 \\ 0 & 0 & 0 & 0 & 1 & 0 & 0 & 0 & 0 \\ 0 & 0 & 0 & 0 & 0 & 1 & 0 & 0 & 0 \end{pmatrix}.$$

We are now concerned with solving the Riemann problem associated to the relaxation model (59) without $\mathbb{T}_\tau(\mathbb{U})$. All characteristics fields are linearly degenerated, as a consequence the exact Riemann solution consists of four constant states separated by three contact discontinuities. This is summarized in the following result.

Lemma 1. *Assume \mathbb{U}_l and \mathbb{U}_r are constant states in \mathcal{V} and consider*

$$(61) \quad \mathbb{U}_0(x) = \begin{cases} \mathbb{U}_l & \text{if } x < 0, \\ \mathbb{U}_r & \text{if } x > 0, \end{cases}$$

as the initial data for the system (59) without $\mathbb{T}_\tau(\mathbb{U})$. Let a_l and a_r be positive numbers $a_l > 0$, $a_r > 0$, and assume the following condition is satisfied

$$(62) \quad b_l = u_l - \frac{a_l}{\rho_l} < u^* < u_r + \frac{a_r}{\rho_r} = b_r,$$

where

$$(63) \quad u^* = \frac{a_l u_l + a_r u_r}{a_l + a_r} - \frac{(\pi_{i,r} + \pi_{e,r}) - (\pi_{i,l} + \pi_{e,l})}{a_l + a_r}.$$

Then the weak solution of system (59) without $\mathbb{T}_\tau(\mathbb{U})$ and supplemented by the initial data defined by (61) is given by

$$(64) \quad \mathbb{U}_{\mathcal{R}} \left(\frac{x}{t}, \mathbb{U}_l, \mathbb{U}_r \right) = \begin{cases} \mathbb{U}_l, & \text{if } b_l > \frac{x}{t}, \\ \mathbb{U}_l^*, & \text{if } b_l \leq \frac{x}{t} \leq u^*, \\ \mathbb{U}_r^*, & \text{if } u^* \leq \frac{x}{t} \leq b_r, \\ \mathbb{U}_r, & \text{if } b_r < \frac{x}{t}. \end{cases}$$

With g standing for either l or r , let us introduce the following notations,

$$(65) \quad \left\{ \begin{array}{l} u^* = \frac{a_l u_l + a_r u_r}{a_l + a_r} - \frac{\pi_{i,r} + \pi_{e,r} - \pi_{i,l} - \pi_{e,l}}{a_l + a_r}, \\ v^* = \frac{a_l v_l + a_r v_r}{a_r + a_l}, \\ w^* = \frac{a_l w_l + a_r w_r}{a_r + a_l}, \\ \pi_{i,l}^* = \pi_{i,l} + c_i a_l \frac{\pi_{i,r} + \pi_{e,r} - \pi_{i,l} - \pi_{e,l} - a_r(u_r - u_l)}{a_l + a_r}, \\ \pi_{e,l}^* = \pi_{e,l} + c_e a_l \frac{\pi_{i,r} + \pi_{e,r} - \pi_{i,l} - \pi_{e,l} - a_r(u_r - u_l)}{a_l + a_r}, \\ \pi_{i,r}^* = \pi_{i,r} + c_i a_r \frac{\pi_{i,l} + \pi_{e,l} - \pi_{i,r} - \pi_{e,r} - a_l(u_r - u_l)}{a_l + a_r}, \\ \pi_{e,r}^* = \pi_{e,r} + c_e a_r \frac{\pi_{i,l} + \pi_{e,l} - \pi_{i,r} - \pi_{e,r} - a_l(u_r - u_l)}{a_l + a_r}, \\ \frac{1}{\rho_g^*} = \frac{1}{\rho_g} - \frac{\pi_{i,g}^* + \pi_{e,g}^* - \pi_{i,g} - \pi_{e,g}}{(a_g)^2}, \\ \varepsilon_{e,l}^* = \varepsilon_{e,l} + \frac{(\pi_{e,l}^* + \pi_{i,l}^*)^2 - (\pi_{e,l} + \pi_{i,l})^2}{2(c_e a_l)^2}, \\ \varepsilon_{i,l}^* = \varepsilon_{i,l} + \frac{(\pi_{e,l}^* + \pi_{i,l}^*)^2 - (\pi_{e,l} + \pi_{i,l})^2}{2(c_i a_l)^2}, \\ \varepsilon_{e,r}^* = \varepsilon_{e,r} + \frac{(\pi_{e,r}^* + \pi_{i,r}^*)^2 - (\pi_{e,r} + \pi_{i,r})^2}{2(c_e a_r)^2}, \\ \varepsilon_{i,r}^* = \varepsilon_{i,r} + \frac{(\pi_{e,r}^* + \pi_{i,r}^*)^2 - (\pi_{e,r} + \pi_{i,r})^2}{2(c_i a_r)^2}, \\ S_{e,g}^* = S_{e,g}, \\ a_g^* = a_g. \end{array} \right.$$

Then the star intermediate states \mathbb{U}_l^* and \mathbb{U}_r^* , belonging to \mathcal{V} , are given by

$$(66) \quad \mathbb{U}_g^* = \begin{pmatrix} \rho_g^* \\ \rho_g^* u^* \\ \rho_g^* v^* \\ \rho_g^* w^* \\ \frac{1}{2} \rho_g^* (u^*)^2 + c_i \rho_g^* \varepsilon_{i,g}^* + c_e \rho_g^* \varepsilon_{e,g}^* \\ c_e \rho_g^* S_{e,g}^* \\ \rho_g^* \pi_{i,g}^* + c_i (a_g^*)^2 \\ \rho_g^* \pi_{e,g}^* + c_e (a_g^*)^2 \\ \rho_g^* a_g^* \end{pmatrix}.$$

Proof. After straightforward computations (see also [24]), the Riemann invariants associated to the eigenvalue u are

$$(67) \quad u, v, w, \pi_i + \pi_e,$$

while those coming from the eigenvalue $u - a/\rho$ are

$$(68) \quad u - a/\rho, \quad v, \quad w, \quad a, \quad \varepsilon_e - \frac{(\pi_e)^2}{2(c_e a)^2}, \quad \varepsilon_i - \frac{(\pi_i)^2}{2(c_i a)^2}, \quad \pi_i + \frac{c_i a^2}{\rho}, \quad \pi_e + \frac{c_e a^2}{\rho}.$$

Finally, the Riemann invariants associated to the eigenvalue $u + a/\rho$ are

$$(69) \quad u + a/\rho, \quad v, \quad w, \quad a, \quad \varepsilon_e - \frac{(\pi_e)^2}{2(c_e a)^2}, \quad \varepsilon_i - \frac{(\pi_i)^2}{2(c_i a)^2}, \quad \pi_i + \frac{c_i a^2}{\rho}, \quad \pi_e + \frac{c_e a^2}{\rho}.$$

Involving the continuity of the Riemann invariants across their associated linearly fields immediately imposes the intermediate states \mathbb{U}_l^* and \mathbb{U}_r^* to be defined by (67)–(69). The proof is thus achieved. \square

Let us note that the hypothesis (62) is essential and it is always satisfied for a sensible choice of positive real numbers a_l and a_r , as stated in the following result.

Lemma 2. For all \mathbb{U}_l and \mathbb{U}_r given in \mathcal{V} with $\mathcal{N}\mathbb{U}_l, \mathcal{N}\mathbb{U}_r \in \mathcal{O}$, there exist two real numbers $a_l > 0$, and $a_r > 0$ with $\frac{a_l}{a_r} = O(1)$ such that the intermediate states \mathbb{U}_l^* and \mathbb{U}_r^* , defined in Lemma 1, belong to \mathcal{V} , and $\mathcal{N}\mathbb{U}_l^*, \mathcal{N}\mathbb{U}_r^* \in \mathcal{O}$.

Proof. The proof, similar to those of [6], done in [1], is not reproduced in this paper. However, we recall the bounds of positive real numbers a_l , and a_r :

$$(70) \quad \begin{cases} a_l \geq \rho_l \max \left(\sqrt{\frac{\gamma p_{i,l}}{c_i \rho_l}}, \sqrt{\frac{\gamma p_{e,l}}{c_e \rho_l}} \right), \\ a_r \geq \rho_r \max \left(\sqrt{\frac{\gamma p_{i,r}}{c_i \rho_r}}, \sqrt{\frac{\gamma p_{e,r}}{c_e \rho_r}} \right). \end{cases}$$

This relation is known as *Whitham subcharacteristic condition*. \square

As usual, a description of a relaxation scheme terminates by the time marching of the numerical method based on this scheme. It consists of two steps:

First step: Evolution step. It consists in solving the hyperbolic part of (59) without $\mathbb{T}_\tau(\mathbb{U})$. This is what is just described in Lemma 1.

Second step: Relaxation step. At this level, the relaxation term $\mathbb{T}_\tau(\mathbb{U})$ is taken into account, that is, here the relaxation system (59) is solved in the limit τ tending to 0 and ρ , \mathbf{u} , \mathcal{E} are frozen:

$$(71) \quad \begin{cases} \partial_t \rho & = & 0, \\ \partial_t \mathbf{u} & = & 0, \\ \partial_t \mathcal{E} & = & 0, \\ \partial_t S_e & = & (\gamma - 1) \nu_{ei}^\mathcal{E} \rho_e^{-\gamma} (T_i - T_e), \\ \pi_e & = & p_e, \\ \pi_i & = & p_i. \end{cases}$$

The presentation of this time marching for the relaxation system (59) has no interest here. We postpone it to the next section where we apply the relaxation system to the model (44).

3.3.2. Implementation of the relaxation scheme for the two-temperature Euler model in toroidal geometry. We are now concerned with advancing in time the numerical method based on the above relaxation scheme devised for computing the numerical solutions of the model (44). At time t^n , we consider a piecewise constant approximation of the solution of the initial model (44) given by,

$$(72) \quad \mathcal{U}^\Delta(R, Z, \varphi, t^n) = \mathcal{U}_\iota^n, \quad (R, Z, \varphi) \in \Omega_\iota,$$

where

$$(73) \quad \mathcal{U}_\iota^n = \begin{pmatrix} \rho_\iota^n \\ \rho_\iota^n \mathbf{u}_\iota^n \\ \frac{1}{2} \rho_\iota^n \mathbf{u}_\iota^n \cdot \mathbf{u}_\iota^n + c_i \rho_\iota^n \varepsilon_{i,\iota}^n + c_e \rho_\iota^n \varepsilon_{e,\iota}^n \\ \rho_{e,\iota}^n S_{e,\iota}^n \end{pmatrix},$$

with $\rho_\iota^n \varepsilon_{i,\iota}^n = \frac{p_{i,\iota}^n}{\gamma - 1}$, $\rho_\iota^n \varepsilon_{e,\iota}^n = \frac{p_{e,\iota}^n}{\gamma - 1}$, $S_{e,\iota}^n = p_{e,\iota}^n (\rho_{e,\iota}^n)^{-\gamma}$, $\rho_{e,\iota}^n = c_e \rho_\iota^n$.

To evolve in time this approximation, we proceed in two steps:

First step: Evolution step. We set the relaxation state as:

$$(74) \quad \mathbb{U}_\iota^n = \begin{pmatrix} \rho_\iota^n \\ \rho_\iota^n \mathbf{u}_\iota^n \\ \frac{1}{2} \rho_\iota^n \mathbf{u}_\iota^n \cdot \mathbf{u}_\iota^n + c_i \rho_\iota^n \varepsilon_{i,\iota}^n + c_e \rho_\iota^n \varepsilon_{e,\iota}^n \\ \rho_{e,\iota}^n S_{e,\iota}^n \\ \rho_\iota^n p_{i,\iota}^n + c_i (a_\iota^n)^2 \\ \rho_\iota^n p_{e,\iota}^n + c_e (a_\iota^n)^2 \\ \rho_\iota^n a_\iota^n \end{pmatrix}$$

where the positive real numbers a_ι^n satisfy Lemma 2.

Then the numerical fluxes $\mathbf{F}(\mathcal{U}_\iota, \mathcal{U}_\ell, \mathbf{n}_{\iota\ell})$ along the interfaces $S_{\iota\ell}$ that constitute the control cell ι are computed with the 1D relaxation scheme (61)-(66). The vector $\mathbf{n}_{\iota\ell}$ is a local unit outward normal of the interface $S_{\iota\ell}$, pointing from ι to ℓ . To get the numerical flux $\mathbf{F}(\mathcal{U}_\iota, \mathcal{U}_\ell, \mathbf{n}_{\iota\ell})$, we first determine the state $\tilde{\mathbb{U}}_\iota^n$ provided by the relaxation scheme (61)-(66) for the corresponding projected Riemann problem of (44) onto $\mathbf{n}_{\iota\ell}$ which is (64).

Second, $\mathbf{F}(\mathcal{U}_\iota, \mathcal{U}_\ell, \mathbf{n}_{\iota\ell})$ is reconstructed as the physical flux of the state $\mathcal{N}\tilde{\mathbb{U}}_\iota^n$ of the projection of (44) onto $\mathbf{n}_{\iota\ell}$, that is: $\mathbf{F}(\mathcal{U}_\iota, \mathcal{U}_\ell, \mathbf{n}_{\iota\ell}) = \mathcal{H}(\mathcal{N}\tilde{\mathbb{U}}_\iota^n)$, where \mathcal{H} is defined in (56). Then using the updating procedure

$$(75) \quad \begin{pmatrix} \hat{\rho}_\iota^{n+1} \\ \hat{\rho}_\iota^{n+1} \hat{\eta}_\iota \hat{\mathbf{u}}_\iota^{n+1} \\ \hat{\mathcal{E}}_\iota^{n+1} \\ \hat{\rho}_{e,\iota}^{n+1} \hat{S}_{e,\iota}^{n+1} \end{pmatrix} = \begin{pmatrix} \rho_\iota^n \\ \rho_\iota^n \eta_\iota \mathbf{u}_\iota^n \\ \mathcal{E}_\iota^n \\ \rho_{e,\iota}^n S_{e,\iota}^n \end{pmatrix} - \frac{\Delta t}{|\Omega_\iota|} \sum_{S_{\iota\ell} \in \mathcal{S}^{\text{pol}} \cup \mathcal{S}^{\text{tor}}} |S_{\iota\ell}| \mathcal{H}(\mathcal{N}\tilde{\mathbb{U}}_\iota^n) \cdot \mathbf{N}_{\iota\ell},$$

the following system, $\partial_t(R\mathcal{U}) + \partial_\zeta(R\mathcal{H}(\mathcal{U})) = 0$, extracted from (55)-(56), is solved at time t^{n+1} with the initial data \mathcal{U}_l^n . The choice of the time-step Δt will be discussed at the end of this section.

Second step: Relaxation. The following system is solved at time t^{n+1} :

$$(76) \quad \begin{cases} \partial_t \rho & = & 0, \\ \partial_t \mathbf{u} & = & 0, \\ \partial_t \mathcal{E} & = & 0, \\ \partial_t S_e & = & (\gamma - 1) \nu_{ei}^\mathcal{E} \rho_e^{-\gamma} (T_i - T_e), \\ \pi_e & = & p_e, \\ \pi_i & = & p_i. \end{cases}$$

with the data $\widehat{\mathcal{U}}_l^{n+1} = \begin{pmatrix} \widehat{\rho}_l^{n+1} \\ \widehat{\rho}_l^{n+1} \widehat{\mathbf{u}}_l^{n+1} \\ \widehat{\mathcal{E}}_l^{n+1} \\ \widehat{\rho}_{e,\ell}^{n+1} \widehat{S}_{e,\ell}^{n+1} \end{pmatrix}$ at time t^n . Thanks to Appendix B, it amounts to solve at time t^{n+1} the system:

$$(77) \quad \begin{cases} \partial_t \rho & = & 0, \\ \partial_t \mathbf{u} & = & 0, \\ \partial_t T_e & = & \nu_{ei} (T_i - T_e), \\ \partial_t T_i & = & \nu_{ei} (T_e - T_i), \end{cases}$$

with the data $\widehat{\mathcal{U}}_l^{n+1}$ at time t^n and temperatures $T_{i,\ell}^n$ and $T_{e,\ell}^n$, and $\nu_{ei} = \frac{\gamma - 1}{k_B n} \nu_{ei}^\mathcal{E}$. System (77) could be solved exactly, yielding:

$$(78) \quad \begin{cases} \rho_l^{n+1} & = & \widehat{\rho}_l^{n+1}, \\ \mathbf{u}_l^{n+1} & = & \widehat{\mathbf{u}}_l^{n+1}, \\ T_{e,\ell}^{n+1} & = & \frac{T_{i,\ell}^n + T_{e,\ell}^n}{2} - \frac{T_{i,\ell}^n - T_{e,\ell}^n}{2} e^{-2\nu_{ei}\Delta t}, \\ T_{i,\ell}^{n+1} & = & \frac{T_{i,\ell}^n + T_{e,\ell}^n}{2} + \frac{T_{i,\ell}^n - T_{e,\ell}^n}{2} e^{-2\nu_{ei}\Delta t}, \end{cases}$$

where $\Delta t = t_{n+1} - t_n$ is the time increment. Then the energy \mathcal{E}_l^{n+1} and entropy state $S_{e,\ell}^{n+1}$ are reconstructed:

$$(79) \quad \begin{aligned} \mathcal{E}_l^{n+1} &= \frac{1}{2} \rho_l^{n+1} \mathbf{u}_l^{n+1} \cdot \mathbf{u}_l^{n+1} + \frac{k_B}{(\gamma - 1)(m_e + m_i)} \rho_l^{n+1} (T_{i,\ell}^{n+1} + T_{e,\ell}^{n+1}), \\ S_{e,\ell}^{n+1} &= \left(\frac{k_B \rho_l^{n+1}}{m_e + m_i} T_{e,\ell}^{n+1} \right) (c_e \rho_l^{n+1})^{-\gamma}. \end{aligned}$$

The state $\mathcal{U}_l^{n+1} = \begin{pmatrix} \rho_l^{n+1} \\ \rho_l^{n+1} \mathbf{u}_l^{n+1} \\ \mathcal{E}_l^{n+1} \\ \rho_{e,\ell}^{n+1} S_{e,\ell}^{n+1} \end{pmatrix}$ at time t^{n+1} is thus determined.

To complete the presentation of our scheme, we now turn to the computation of the time-step Δt . Consider the 2D control cell $\Omega_{\ell_{2D}}^{2D}$ that generates the 3D control cell Ω_ℓ . Let $T_{\ell_{2D}}$ be any generic triangle that enters in the construction of $\Omega_{\ell_{2D}}^{2D}$ as in the formula (45). Let $h_{\ell_{2D}}$ be the minimum of the heights of the triangle $T_{\ell_{2D}}$. We set:

$$(80) \quad \begin{cases} \widehat{\lambda}_\ell = \max \left\{ |u_{\varphi,\ell}^n + c_{s,\ell}|, |u_{\varphi,\ell}^n - c_{s,\ell}|, |u_{\varphi,\ell}^n - \widehat{c}_{ei,\ell}|, |u_{\varphi,\ell}^{next} + \widehat{c}_{ei,\ell}| \right\}, \\ \widehat{\lambda}_{\ell(\ell_{2D})} = \max \left\{ |\mathbf{u}_l^n \cdot \mathbf{n}_{\ell(\ell_{2D})} + c_{ei,\ell}|, |\mathbf{u}_l^n \cdot \mathbf{n}_{\ell(\ell_{2D})} - c_{ei,\ell}|, |\mathbf{u}_l^n \cdot \mathbf{n}_{\ell(\ell_{2D})} - \widehat{c}_{ei,\ell}|, |\mathbf{u}_{\ell_{2D}}^n \cdot \mathbf{n}_{\ell(\ell_{2D})} + \widehat{c}_{ei,\ell(\ell_{2D})}| \right\}, \end{cases}$$

where:

$$(81) \quad \begin{cases} c_{s,\ell} = \sqrt{\gamma \frac{p_{i,\ell}^n + p_{e,\ell}^n}{\rho_l^n}}, & \widehat{c}_{ei,\ell} = \max \left(\sqrt{\frac{\gamma p_{i,\ell}^n}{c_i \rho_l^n}}, \sqrt{\frac{\gamma p_{e,\ell}^n}{c_e \rho_l^n}} \right), \\ \widehat{c}_{ei,\ell_+} = \max \left(\sqrt{\frac{\gamma p_{i,\ell_+}^n}{c_i \rho_{\ell_+}^n}}, \sqrt{\frac{\gamma p_{e,\ell_+}^{next}}{c_e \rho_{\ell_+}^n}} \right), & \widehat{c}_{ei,\ell(\ell_{2D})} = \max \left(\sqrt{\frac{\gamma p_{i,\ell}^n}{c_i \rho_{\ell(\ell_{2D})}^n}}, \sqrt{\frac{\gamma p_{e,\ell}^n}{c_e \rho_{\ell(\ell_{2D})}^n}} \right). \end{cases}$$

The ι_+ th vertex represents the right neighbour of the ι th vertex in the φ -direction. The integer $\ell(\ell_{2D})$ is defined from ℓ_{2D} through:

$$(82) \quad \Omega_\iota = \prod_{\varphi \in [\varphi_{j-1/2}, \varphi_{j+1/2}]} \mathcal{R}_\varphi(\Omega_{\iota_{2D}}^{2D}), \quad \Omega_{\ell(\ell_{2D})} = \prod_{\varphi \in [\varphi_{j-1/2}, \varphi_{j+1/2}]} \mathcal{R}_\varphi(\Omega_{\ell_{2D}}^{2D}),$$

where \mathcal{R}_φ stands for the rotation around φ about the Z -axis. We define:

$$(83) \quad \Delta t_\iota = \min \left\{ \frac{\Delta \varphi_\iota}{\lambda_\iota}, \min_{\ell(\ell_{2D})} \left(\frac{h_{\iota_{2D}} \ell_{2D}}{\lambda_{\iota \ell(\ell_{2D})}} \right) \right\},$$

where the minimum on ℓ_{2D} covers all triangles $T_{\ell_{2D}}$ that share the ι_{2D} th vertex. The length in the φ -direction of the 3D control cell Ω_ι is: $\Delta \varphi_\iota = \varphi_{j+1/2} - \varphi_{j-1/2}$. The time-step is then given by:

$$(84) \quad \Delta t = \text{CFL} \min_\iota \Delta t_\iota$$

where ι covers all the vertices of the tessellation and CFL stands for the CLF number belonging to $(0, 1]$. The presentation of our scheme is thus achieved.

Finally, assume $\rho_\iota^n > 0$, $\mathcal{E}_\iota^n - \frac{1}{2} \rho_\iota^n (\mathbf{u}_\iota^n)^2 > 0$, $S_{e,\iota}^n > 0$, and the bounds (70) as well as the time-step satisfies (84). Then $\rho_\iota^{n+1} > 0$, in performing the same proof as those done in [6]. According to Appendix B, $T_{e,\iota}^{n+1} > 0$, $T_{i,\iota}^{n+1} > 0$, leading then to: $\varrho_\iota^{n+1} > 0$, $\mathcal{E}_\iota^{n+1} - \frac{1}{2} \rho_\iota^{n+1} (\mathbf{u}_\iota^{n+1})^2 > 0$, $S_{e,\iota}^{n+1} > 0$, *i.e.* \mathcal{U}_ι^{n+1} is in \mathcal{O} . The following result on robustness of the suggested relaxation scheme can be thus stated.

Theorem 2. *Let \mathcal{U}_ι^n be in \mathcal{O} for ι covering all the vertices of the tessellation. Assume the time-step Δt is chosen according to (84) while each local relaxation parameters a_l and a_r fulfill the bounds (70) set in the proof of Lemma 2. Then \mathcal{U}_ι^{n+1} defined by (78)-(79) belong to \mathcal{O} for all ι .*

Entropy preservation and minimum principle preservation of the proposed relaxation scheme could be established in the same fashion as [6], ensuring its stability. This is postponed to a future paper, in order to lighten this present report of our work.

3.4. A second order extension. Modifications can be implemented in the above relaxation scheme to achieve a second order accurate method both in time and space. Second order accuracy in time can be got by using the Runge-Kutta 2 method. We use a MUSCL-type approach to reach a second order accurate scheme in space [24, 33]. According to the features of the mesh, the gradient used to devise reconstructed states is obtained in dealing with two subproblems: a gradient in (R, Z) coordinates is got in the triangular mesh fashion [25, 24]. A 1D gradient in the φ -direction is then devised, leading to the design of the full gradient. However, one has to care about the fact that the gradient to approximate in the φ -direction for the velocity $(u_R, u_Z, u_\varphi)^T$ is the following vector:

$$(85) \quad \begin{pmatrix} \frac{1}{R} \frac{\partial u_R}{\partial \varphi} - \frac{u_\varphi}{R} \\ \frac{1}{R} \frac{\partial u_Z}{\partial \varphi} \\ \frac{1}{R} \frac{\partial u_\varphi}{\partial \varphi} + \frac{u_R}{R} \end{pmatrix}.$$

4. NUMERICAL TESTS

We now turn to the experiments with the numerical strategies designed in this work to some pertinent test cases.

4.1. Shock tube problem. The robustness of the relaxation scheme proposed in this paper to handle different waves motivates this test case. The initial data, given in Table 2, is such that the usual ratio 10 between left and right pressures is fulfilled. This test case is a shock tube-type in 1D setting on the interval $[0, 1]$ along the x -axis and the discontinuity is located at $x = 0.5$. However, it has been run in a 2D setting on a square $[0, 1] \times [0, 1]$ meshed with 200×5 points while the computation is carried out until $t = 8.6289 \times 10^{-8}$ s.

	ρ	\mathbf{u}	$T_e(\text{K})$	$T_i(\text{K})$
Left state	1	0	1.04436×10^8	1.27644×10^8
Right state	0.125	0	8.1228×10^7	1.04436×10^8

TABLE 2. Initial data for the shock tube problem.

First we set $\nu_{ei} = 0$ meaning that source term is ignored during the simulation in order to check the robustness of the transport step of the relaxation scheme suggested in this work. In order to test the transport part of the numerical method, the simulation is first realized without any source term: $\nu_{ei} = 0$. The results are given in Figure 3. As expected, the solution is 1D, and although the simulation has been done on a 2D mesh, the numerical scheme does not generate transverse velocities. The density is well-captured. An overshoot of temperatures at the beginning of the contact discontinuity around $x = 0.64$ is observed. The electron entropy is constant across the shock wave at $x \approx 0.84$ as expected, while on the opposite the ion entropy jumps across the shock.

Second, we turn on temperature relaxation source terms, that is ν_{ei} is no longer null, given in [28] according to:

$$\nu_{ei} = 1.8 \times 10^{-19} \frac{\sqrt{m_e m_i} \lambda_{ei}}{(m_i T_e + m_e T_i)^{3/2}} s^{-1},$$

and λ_{ei} is the Coulomb logarithm defined in [28] by

$$\lambda_{ei} = \begin{cases} 23 - \ln\left(\frac{\sqrt{n_e}}{T_e^{3/2}}\right), & \frac{m_e}{m_i} T_i < T_e < 10eV, \\ 24 - \ln\left(\frac{\sqrt{n_e}}{T_e}\right), & \frac{m_e}{m_i} T_i < 10eV < T_e, \end{cases}$$

where the temperatures T_e , and T_i are in eV, the masses m_e , and m_i are expressed in g , and the electron density n_e is in cm^{-3} . The results are shown in Figure 4 at the time $t = 8.6289 \times 10^{-8}$ s. According to the initial data 2 the temperatures T_i and T_e are expected to reach a common value at the following thermal equilibrium times or thermal relaxation times:

$$t_{eq,Left} = 2.39 \times 10^{-8} s, \quad t_{eq,Right} = 1.21 \times 10^{-7} s.$$

The results show that on the left side where the relaxation time is smaller, the thermal equilibrium is reached before the contact discontinuity. At the same time, the two temperatures are still significantly different on the right side. The presence of the temperature relaxation source terms modifies the entropies of electrons and ions, as it should be. The electron entropy is no longer constant across the shock wave, while the deviation of ion entropy is small compared to the results displayed in Figure 3.

4.2. Implosion test case. This test case is inspired from [15] and adapted to the two-temperature Euler equations. Indeed, the density and velocity initial data are the same as the ones used in [15]. The physical motivation of this test is to simulate a laser beam shooting a target in order to initiate a fusion reaction. Then, for this test, the temperatures are chosen in order to be in the laser plasma domain [28]. From a computational point of view, we test in this simulation the capability of the numerical scheme to handle shock focusing and reflection leading to a large and fast increase of the density. The initial data is given in Table 3, where Inner stands for the points (x, y) of the disc whose radial coordinate r satisfies $r = \sqrt{x^2 + y^2} \leq 0.5$, and Outer represents points with $r = \sqrt{x^2 + y^2} \geq 0.5$. This test has been computed in a 2D Cartesian geometry on a simulation domain equal to a quarter of disc of radius

	ρ	\mathbf{u}	T_e (K)	T_i (K)
Inner	1	0	2.3×10^6	1.7406×10^6
Outer	1	0	2.3×10^7	1.7406×10^7

TABLE 3. Initial data for the implosion problem.

equal to 1 meshed by 33153 points. The mesh is a refined version of the mesh presented in Figure 5. Since we want to compute the reflection of the shock wave at the origin, it has not been possible to use a polar grid that contains very small cells at the origin and thus implies the use of very small time steps. The mesh used is a good approximation of a polar mesh: the constant radius lines are almost mesh lines. However, this is not exactly true and will lead to some numerical artefacts.

This problem contains three cylindrical waves propagating towards the origin: first a shock, followed by a contact discontinuity leaving behind it a rarefaction wave. After interacting with the origin the shock will be reflected back and will propagate towards the exterior. Eventually, the reflected shock will interact with the contact discontinuity that is still propagating towards the center. At the initial time, the equilibrium temperature times for the Inner and the Outer states are

$$t_{eq,Inner} = 1.34 \times 10^{-10} s, \quad t_{eq,Outer} = 2.97 \times 10^{-9} s,$$

that are quite small. Figures 6 and 7 present the results obtained at the time $t_1 = 4.0901 \times 10^{-7}$ s before the interaction of the shock with the origin. Since t_1 is significantly larger than the temperature relaxation times, the electron and ion temperatures had time to relax to a common value as shown on the colour plot of Figure 6 and the 1D plot of Figure 7 where the electron and ion pressures and temperatures are the same.

Since the initial data depends only on r , we expect a 1D solution in a cylindrical coordinates system r, θ . As shown in Figures 6 and 8, this property is satisfied by the simulation except on the contact discontinuity where small wiggles appears. These wiggles grow with time. This loss of the 1D character of the solution is not seen on the propagation of the shock wave but appears on the contact discontinuity. It is likely that these wiggles are initiated

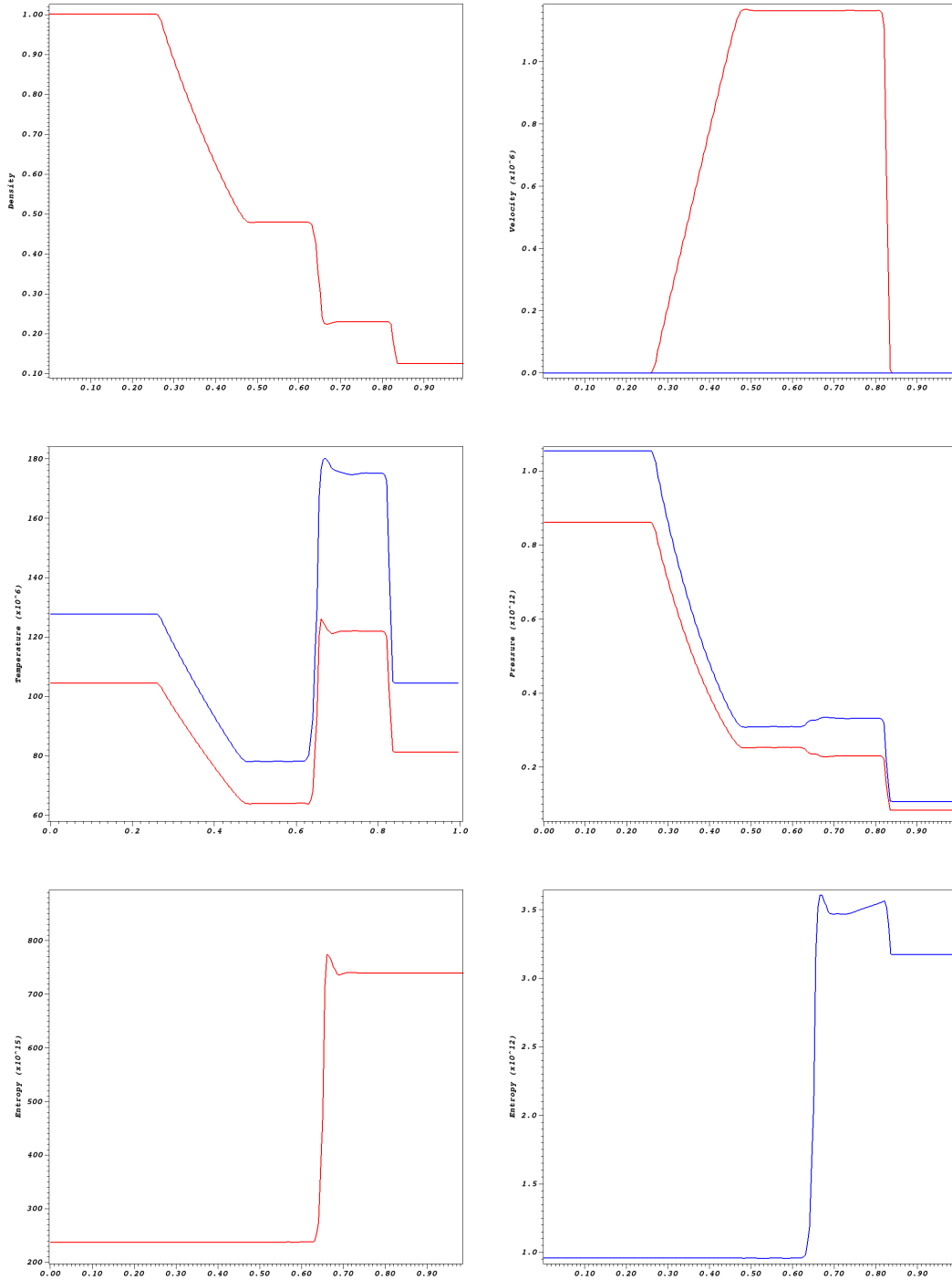


FIGURE 3. Shock tube problem at $t = 8.6289 \times 10^{-8}$ s with $v_{ei}^e = 0$. Solution at $y = 0.5$. Left-Top: Density, Right-Top: x -velocity in red, and y -velocity in blue, Left-Center: Electron (red) and ion (blue) temperatures, Right-Center: Electron (red) and ion (blue) pressures, Left-Bottom: Electron entropy, Right-Bottom: Ion entropy.

by the fact that the mesh is not exactly aligned with the initial data and that they are amplified by some kind of Richtmyer-Meshkov type instability although we do not claim that they have a physical origin.

Figures 8 and 9 present the results at $t = t_2 = 6.22 \times 10^{-7}$ s shortly after the reflection of the shock. The density and pressure at the origin have increased by a factor ten and a zone of positive velocity can be noticed while the contact discontinuity is still moving towards the center.

Finally at $t = t_3 = 8.4973 \times 10^{-7}$ s the shock begins to interact with the contact discontinuity. In Figure 10 are displayed the evolution of the density contours at times t_1, t_2, t_3 , that show the development of instabilities on the contact discontinuity with mushroom shapes. However the mesh resolution for this computation is too coarse to pretend to capture a true physical instability and the contact is smeared over several cells. This is a well-know

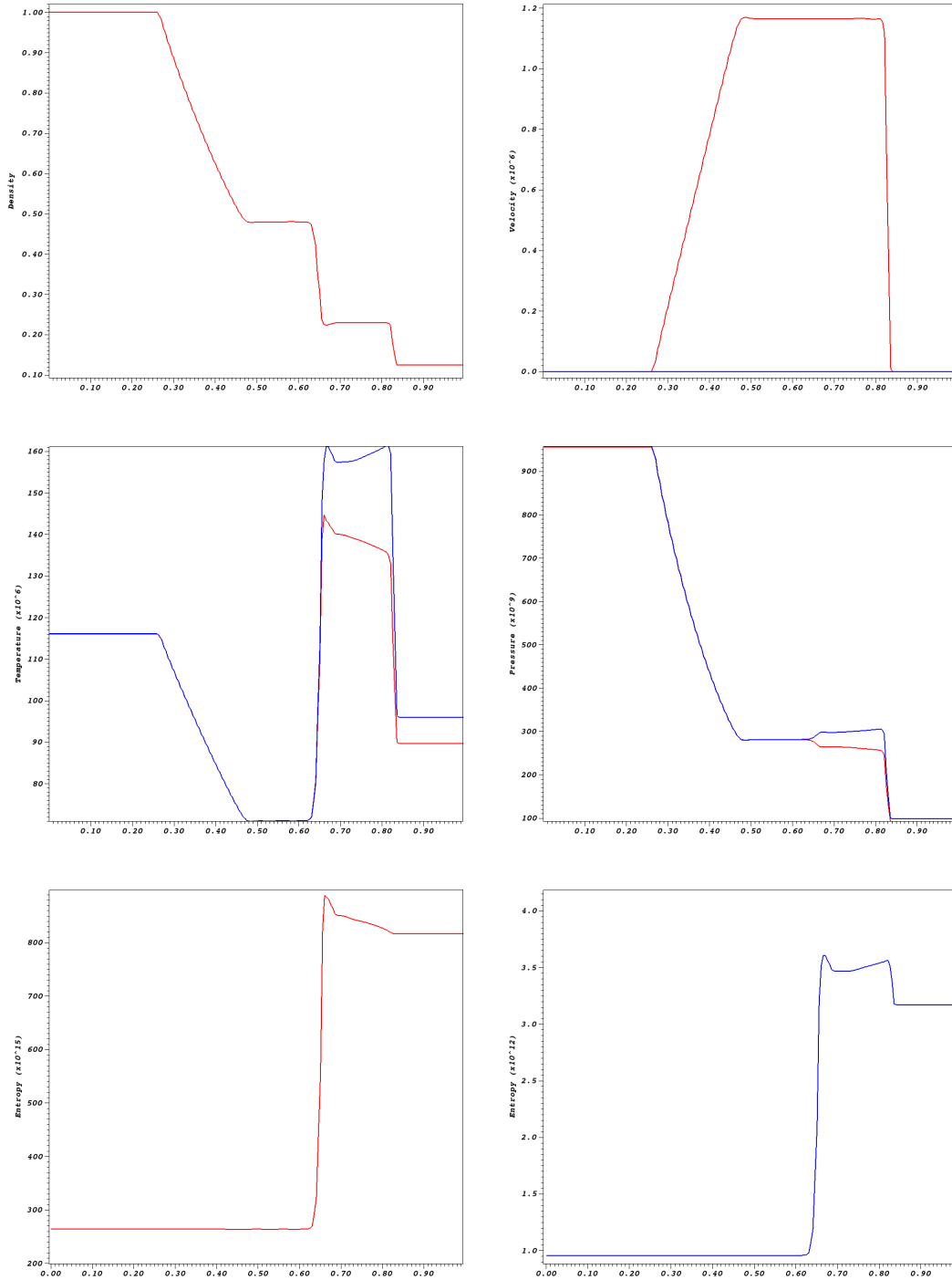


FIGURE 4. Shock tube problem at $t = 8.6289 \times 10^{-8}$ s with $v_{ei}^e \neq 0$. Solution at $y = 0.5$. Left-Top: Density, Right-Top: x -velocity in red, and y -velocity in blue, Left-Center: Electron (red) and ion (blue) temperatures, Right-Center: Electron (red) and ion (blue) pressures, Left-Bottom: Electron entropy, Right-Bottom: Ion entropy.

problem in the computation of linearly degenerate-waves by Eulerian methods and is often taken as an argument to prefer Lagrangian methods for multi-material problems and specially for ICF simulations [30, 31, 22].

4.3. Sedov injection in 2D Cartesian geometry. A Sedov problem is considered in a uniform medium with cylindrical axisymmetry [22]. It consists in depositing an intense energy spot in the center of the disc of the uniform medium and following its evolution. Here, we adapt this test from [22, 30, 31] to the two-temperature Euler model by prescribing

$$T_e = 1.7406 \times 10^7 \text{K}, \quad T_i = 5.802 \times 10^6 \text{K}$$

for the temperatures of the electrons and the ions that are injected in the center of the disc. The temperatures of the rest of the uniform domain are $T_e = T_i = 2.901 \times 10^4 \text{K}$ while the density and velocity are $\rho = 1$, $\mathbf{u} = 0$,

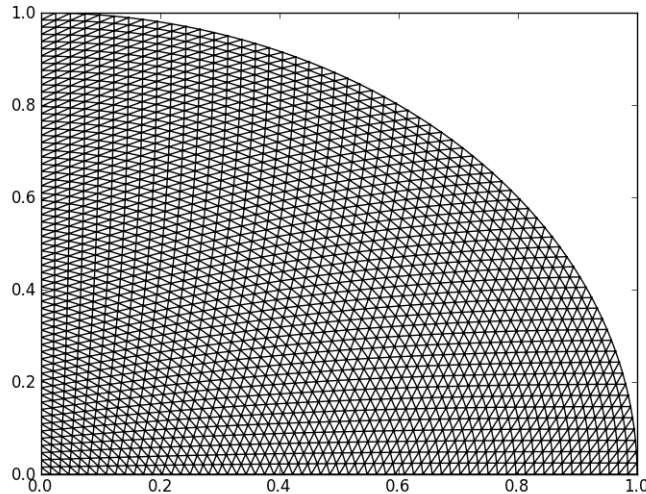


FIGURE 5. Implosion problem, similar mesh with 2145 points as the one used in numerical simulation. The mesh used in Section 4.2 has been obtained by a refinement of a factor 4 from the present one and contains 33153 ($\approx 4 \times 4 \times 2145$).

respectively.

In [30, 31], the domain is a quarter of disc of radius equal to 1. In the present simulation, the computational domain is a complete disc of radius equal to 1 meshed with 8321 points with a tessellation similar to the one of Figure 5. Such a mesh has the property that the points are almost aligned in the R -direction but avoid small cells at the center of the domain. Note also that in contrast with polar meshes, the origin is not a singular point and therefore, since the computation is done on the whole disc, there is no boundary conditions to enforce at the center of the disc which is an interior point. The injection of energy takes place in the cell containing the disc center. The final time of the computation is chosen in order to compare the results to the ones obtained in [30]. Figure 11 shows the computed results at $t = 9.7634 \times 10^{-6}$ s that consists of an expanding shock wave. Likewise the implosion problem, the initialization is 2D in the Cartesian coordinates and the expected solution is 1D in cylindrical coordinates. As shown in Figure 11, the numerical solution respects this property. This is what was expected from the previous test since the loss of the cylindrical symmetry of the computation was shown to occur on contact discontinuity but not on propagating shock waves. Figure 12 presents the results of the density and temperatures at three different times. In Figure 12, at the final time, the maximum of density is about 1.2, whereas in [31] the density reaches a maximum around 3.5. It is shown in [22] that the exact density reaches a maximum of 6. This is due to the fact that the mesh used here is not fine enough.

At the initialization, the relaxation time to reach the temperature at the injection cell is 1.3×10^{-9} s while at the end of the simulation it is 2.2×10^{-9} s. Therefore, the equilibrium is reached soon after the beginning of the simulation. Figure 12 gives a zoom near the origin of the 1D profile of the two temperatures at two different times in the beginning of the simulation: the two temperatures attain rapidly a common value on the whole domain as the expanding shock propagates from the disc center.

This test has shown that the numerical method is able to compute a strong expanding shock wave on a 2D Cartesian mesh with no loss of the 1D cylindrical character of the solution.

4.4. Sedov injection in a poloidal plane of a torus with axisymmetry initialization. We are now interested in testing the 3D numerical method in cylindrical (R, Z, φ) geometry that has been devised in this paper to the previous Sedov experiment where the considered disc is contained in the poloidal plane of a torus. The major radius of the torus is 5. According to the asymmetric feature of the medium and the torus, two types of experiment are envisaged. The first one is a 2D one where we assume that all derivatives in the φ -direction are zero and therefore we use only one poloidal plane to define the computational domain. The second experiment is a true 3D computation where 20 poloidal planes have been used to discretize the toroidal direction. In this case, the initial conditions are axisymmetric in the φ -direction, and do not depend on φ . Therefore, we expect the solution to be axisymmetric for all $t > 0$. The goal of this test is to check that the numerical method does not generate artificial toroidal velocities and does not destroy the axisymmetric character of the solution.

The results are displayed at $t = 9.7634 \times 10^{-6}$ s in Figures 13. With respect to the previous simulation, we observe that in a toroidal geometry, the solution is no longer 1D in the R, φ -coordinate system. In particular, the wave is moving faster on the center of the torus side than on the exterior side. Small differences appear on the maximum values of the density which 1.168 for Cartesian coordinates, and 1.145 for the axisymmetric case. The thermal equilibrium of temperatures also slightly changed, 5.5×10^{-8} s for the axisymmetric case instead of 5×10^{-8} s in

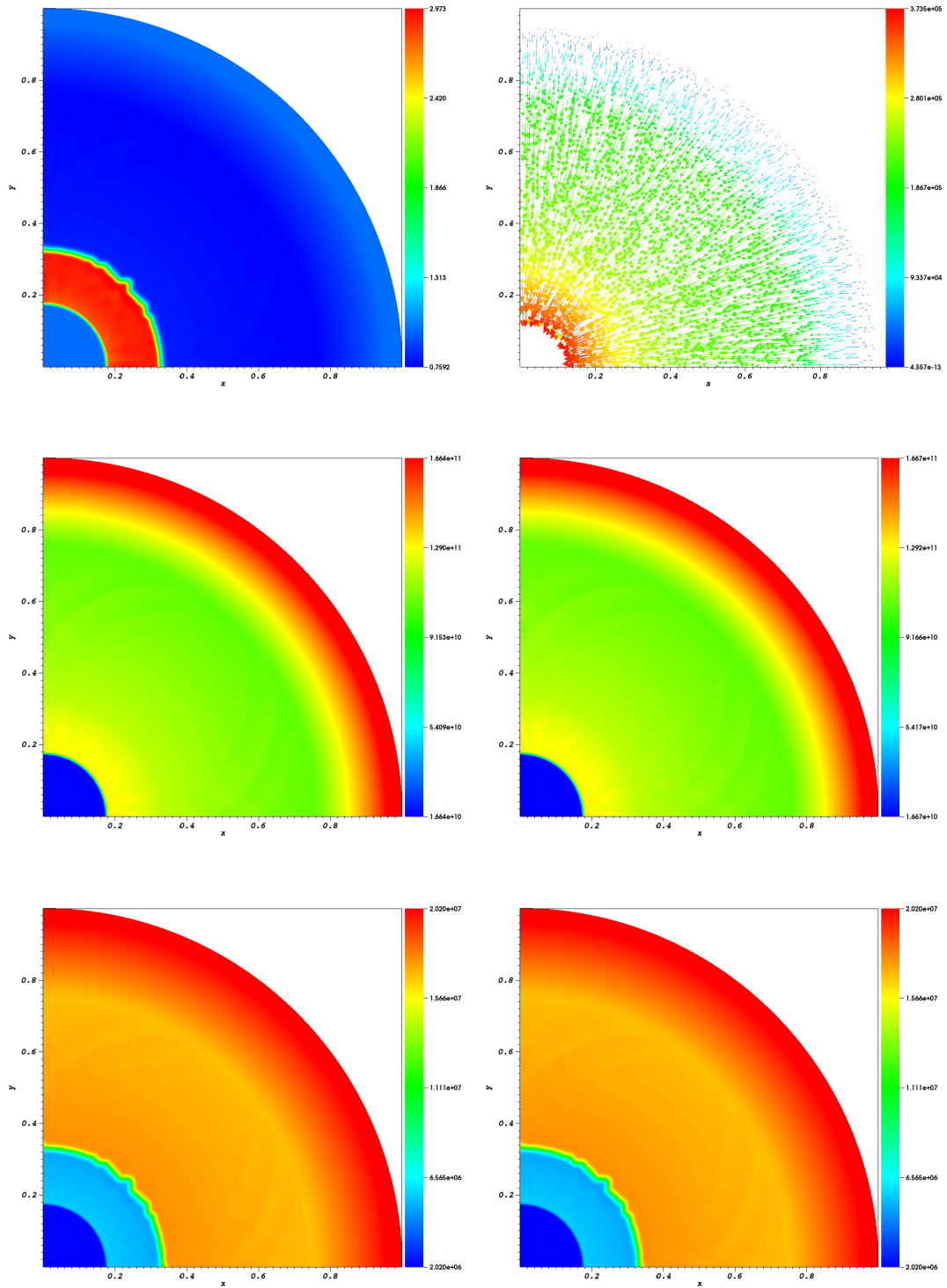


FIGURE 6. Implosion problem at $t_1 = 4.0901 \times 10^{-7}$ s. 2D fields of Density: Left-Top, Velocity: Right-Top, Electron pressure: Left-Center, Ion pressure: Right-Center, Electron temperature: Left-Bottom, Ion temperature: Right-Bottom.

the Cartesian case.

As shown in Figure 13, the 3D results are extremely close to the 2D ones. Moreover, no toroidal velocity has been generated in the 3D as shown in Figure 14 and the solution remains axisymmetric. Therefore, our numerical method yields good agreement with the goal of this test-case.

4.5. Triple point problem in a rectangular computational domain. The goal of this next experiment is to emphasize that in absence of temperature relaxation, the solution of the two-temperature model is not identical to the solution of a single temperature model even if the electron and ion temperatures are initially equal. Then, we consider a three state problem, inspired by the test case carried out in [22] and compare their results to the ones of the relaxation scheme. The electron and ion pressures are chosen to be equal and correspond to the same

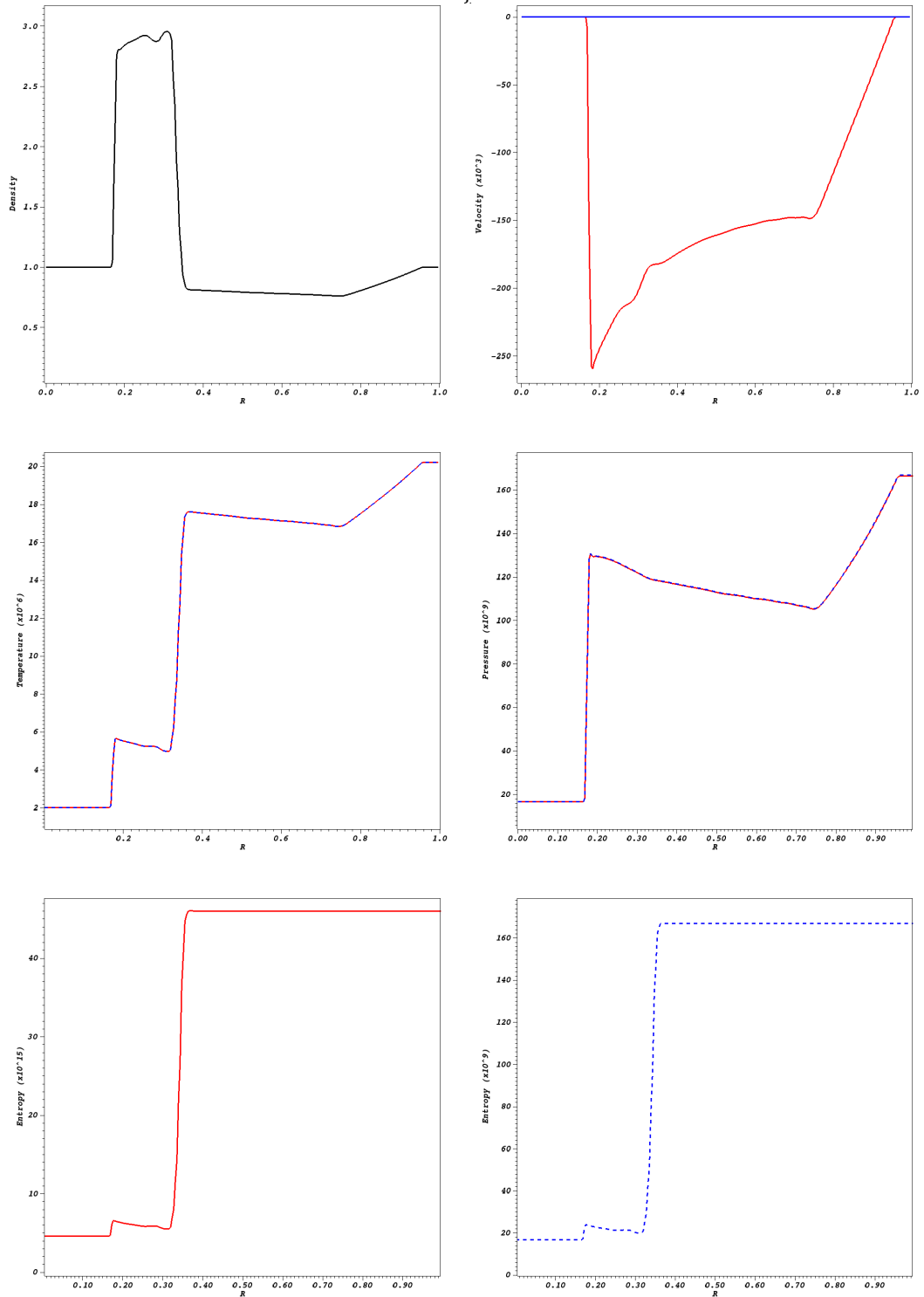


FIGURE 7. Implosion problem at $t_1 = 4.0901 \times 10^{-7}$ s. 1D fields at $y = x$ of Density:Left-Top, Radial (red) and tangential (blue) velocities: Right-Top, Electron (red) and ion (blue) temperatures: Left-Center, Electron (red) and ion (blue) pressures: Right-Center, Electron entropy: Left-Bottom, Ion entropy: Right-Bottom.

total pressure as the one fixed in [22]. The other difference between the two tests is that in our test, the adiabatic index γ is uniform and set equal to $5/3$.

The computational domain is the rectangle $[0, 7] \times [-3, 3]$ meshed with 70×60 points with symmetric elements around the x -axis. The domain is divided in three different sub-domains Ω_1 , Ω_2 , and Ω_3 . The sub-domain Ω_1 is given by the rectangle $[1, 7] \times [-1.5, 1.5]$ and contains a high-density and low-pressure fluid. The sub-domain Ω_2 corresponds to the rectangle $[0, 1] \times [-3, 3]$ and is composed of a high-density and high-pressure fluid. Finally, the sub-domain Ω_3 is the rest of the domain and contains a low-density and low-pressure fluid. This description is summarized in Figure 15.

In [22], the evolution of this three-state problem is described: the intersections of the three sub-domains Ω_1 , Ω_2 , and Ω_3 are located at $(1, -1.5)^T$ and $(1, 1.5)^T$, those two points are named triple points. Let us first consider a

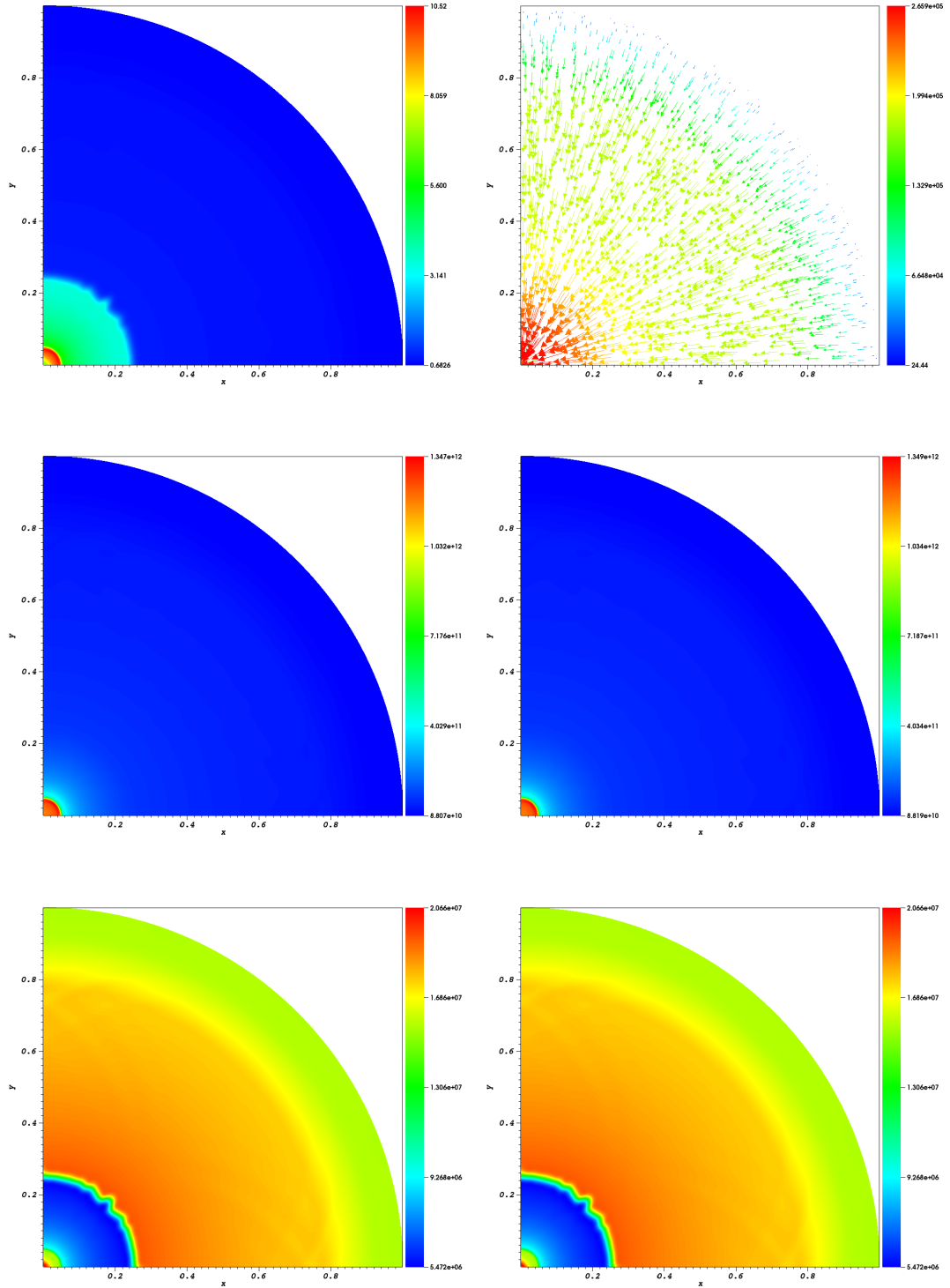


FIGURE 8. Implosion problem at $t_2 = 6.22 \times 10^{-7}$ s. 2D fields of Density: Left-Top, Velocity: Right-Top, Electron pressure: Left-Center, Right-Center: Ion pressure, Left-Bottom: Electron temperature, Ion temperature: Right-Bottom.

point located on the interface between Ω_2 and Ω_1 far from the triple points, the initial data generate three waves which are a contact discontinuity, a rightward shock, and a leftward rarefaction. This is also the case for a point on the interface between Ω_2 and Ω_3 far from the triple points. In the case of the interface between Ω_1 and Ω_3 , it produces a contact discontinuity. Around the triple points, the situation is quite tricky. Since the different waves are interacting together it leads to a complex 2D fluid flow. As it is pointed out in [22], the two rightward shock waves of Ω_1 and Ω_3 are not moving at the same sound speed due to their difference of density. Indeed we have $\rho_3 c_{s,3} < \rho_1 c_{s,1}$, then the rightward shock of Ω_3 is moving faster than the Ω_1 one. This creates a strong shear leading to a Kelvin-Helmholtz instability and to the formation of a vortex.

In our simulation, we set $\nu_{ei} = 0$ and leave the ion and electron temperature evolve independently. In Figure 16, we

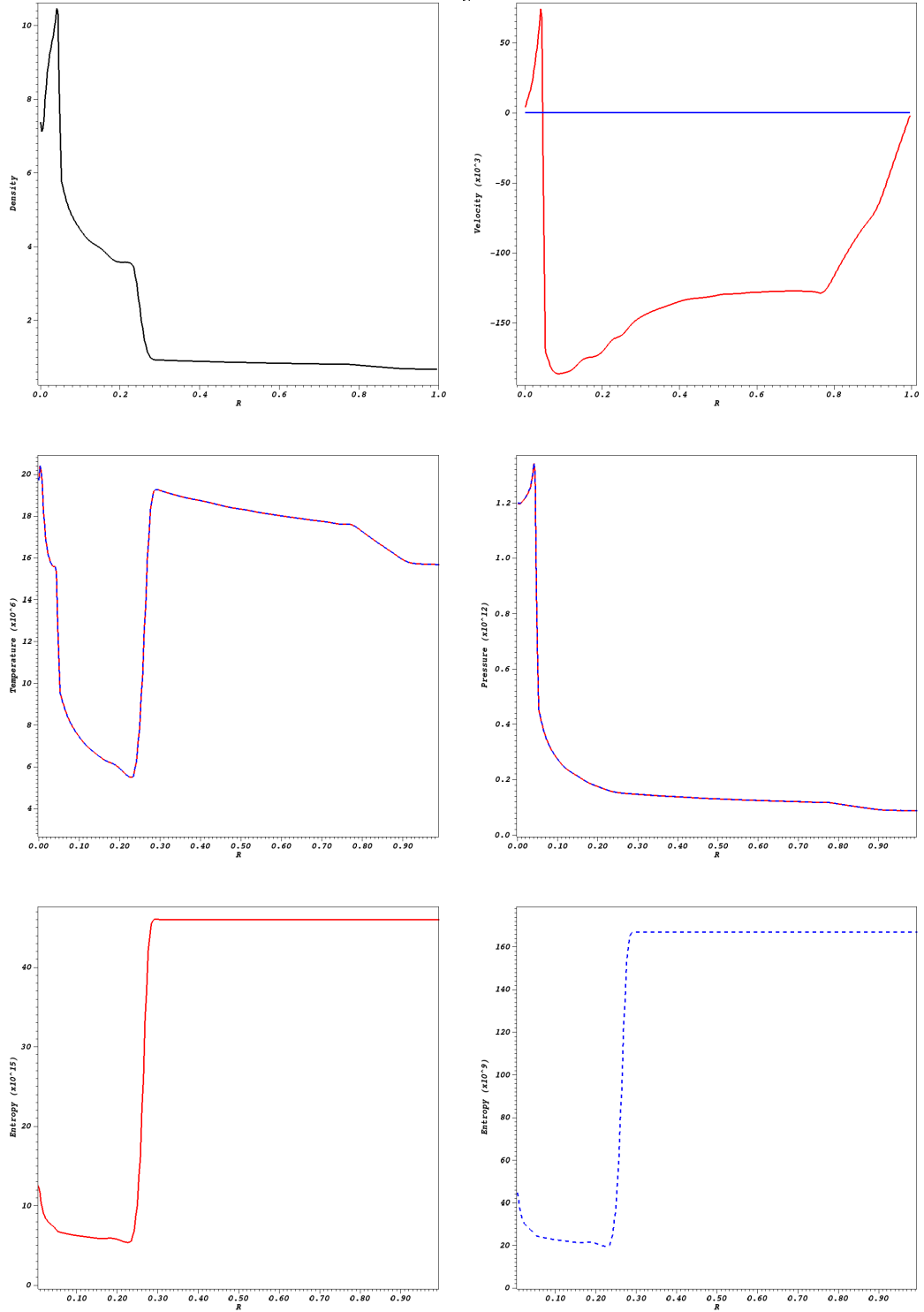


FIGURE 9. Implosion problem at $t_2 = 6.22 \times 10^{-7}$ s. 1D fields at $y = x$ of Density:Left-Top, Radial (red) and tangential (blue) velocities: Right-Top, Electron (red) and ion (blue) temperatures: Left-Center, Electron (red) and ion (blue) pressures: Right-Center, Electron entropy: Left-Bottom, Ion entropy: Right-Bottom.

compare the results of the internal energy of the mixture given by

$$\varepsilon = \frac{1}{\gamma - 1} \frac{p_e + p_i}{\rho},$$

at the time 3.5 s and 5 s with the results of [22]. We can see that at $t = 3.5$ s the results obtained with the relaxation scheme for the two-temperature Euler equations are quite different from the ones of [22] (note that in Figure 16 the results of [22] are obtained by two different numerical methods, this is why their results are not symmetric with respect to the $y = 0$ axis). Indeed, Figure 17 displays the ratio $\frac{T_i - T_e}{T_e}$ at two successive times which shows that the temperatures do not remain identical although $T_i = T_e$ at the initialization, and without the use of thermal exchange

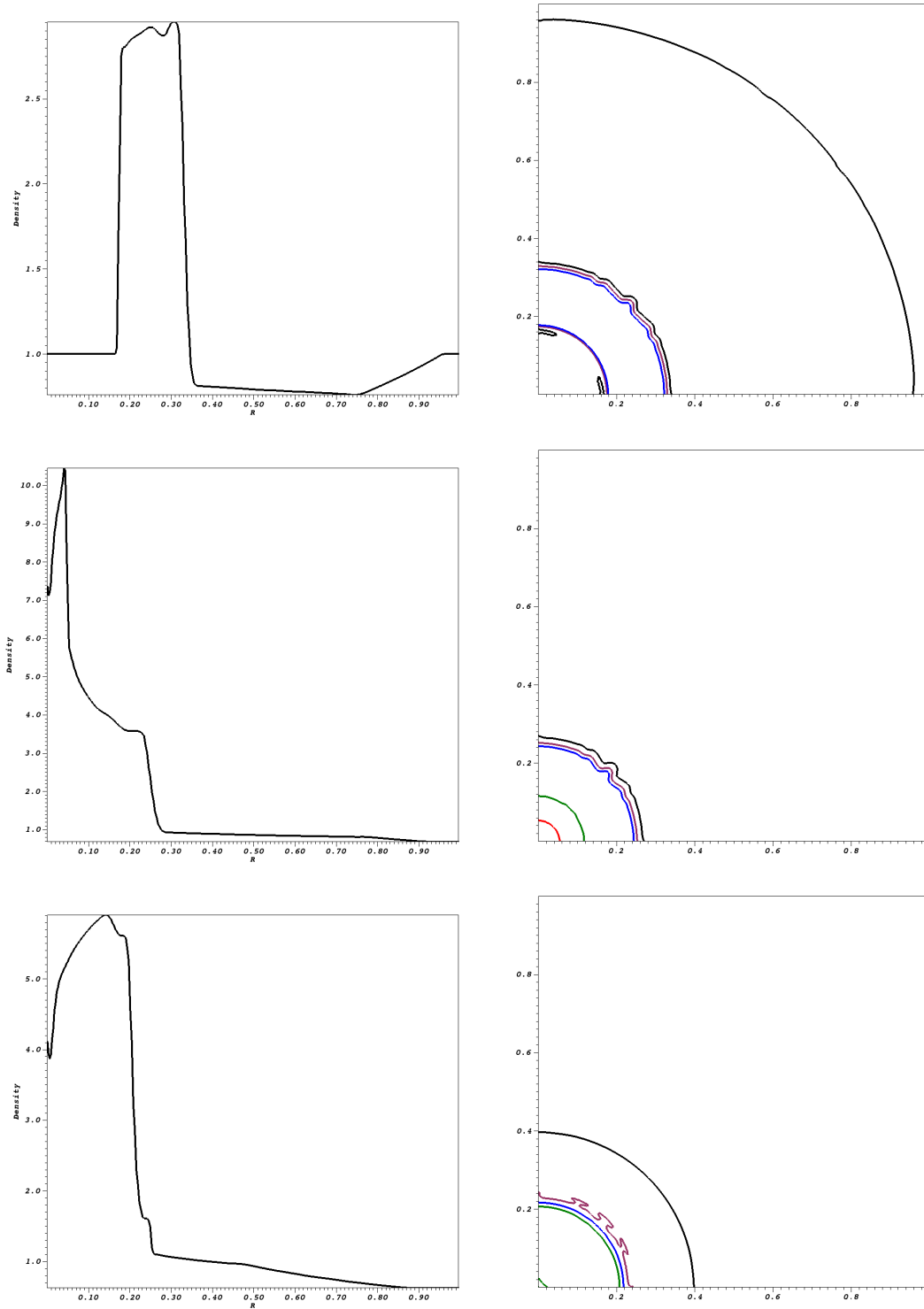


FIGURE 10. Implosion problem, Density, Left: 1D fields at $y = x$, Right: 2D isolines at $\rho = 1$ (black), $\rho = 1.585$ (violet), $\rho = 2.369$ (blue), $\rho = 4.259$ (green), and $\rho = 6.047$ (red). Top: $t_1 = 4.0901 \times 10^{-7}$ s, Middle: $t_2 = 6.22 \times 10^{-7}$ s, Bottom: $t_3 = 8.4973 \times 10^{-7}$ s.

in the equations The same result can be inferred from Figure 18 that shows the density, the electron temperature, and the ion one at $t = 3.5$ s and $t = 5.0$ s. This is due to the fact that in the transport step, the electron entropy jump is assumed to be zero across a shock. Therefore the discontinuous solutions of the two-temperature model are not the same than the ones of the mono-fluid Euler equations and even if the initial temperatures are equal, in the presence of discontinuous solutions, the two-temperature Euler model is not equivalent to the mono-fluid Euler model.

4.6. Triple point problem in a disc in 2D Cartesian geometry. Here we consider a triple point problem in a different geometry as a preliminary test for studying some problems of injection in tokamaks where very cold and dense cryogenic Deuterium/Tritium mixtures known as pellets are injected in a hot plasma. We first consider a problem in Cartesian geometry. The computational domain is now a disc of radius 1 meshed with 1435 cells.

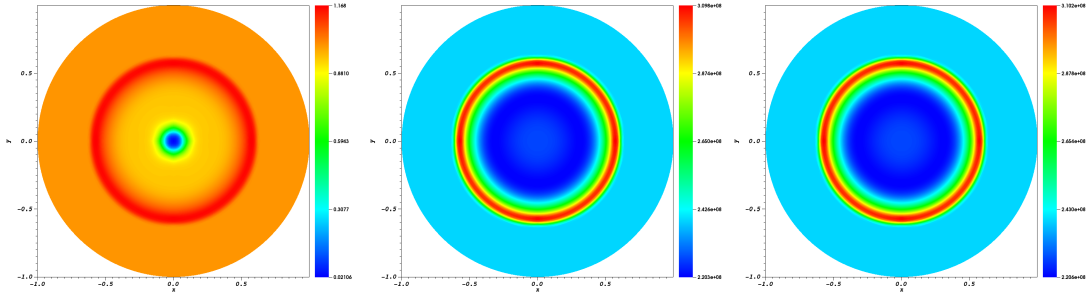


FIGURE 11. Sedov injection in 2D Cartesian geometry at $t = 9.7634 \times 10^{-6}$ s. Left: Density, Center: Electron pressure, Right: Ion pressure.

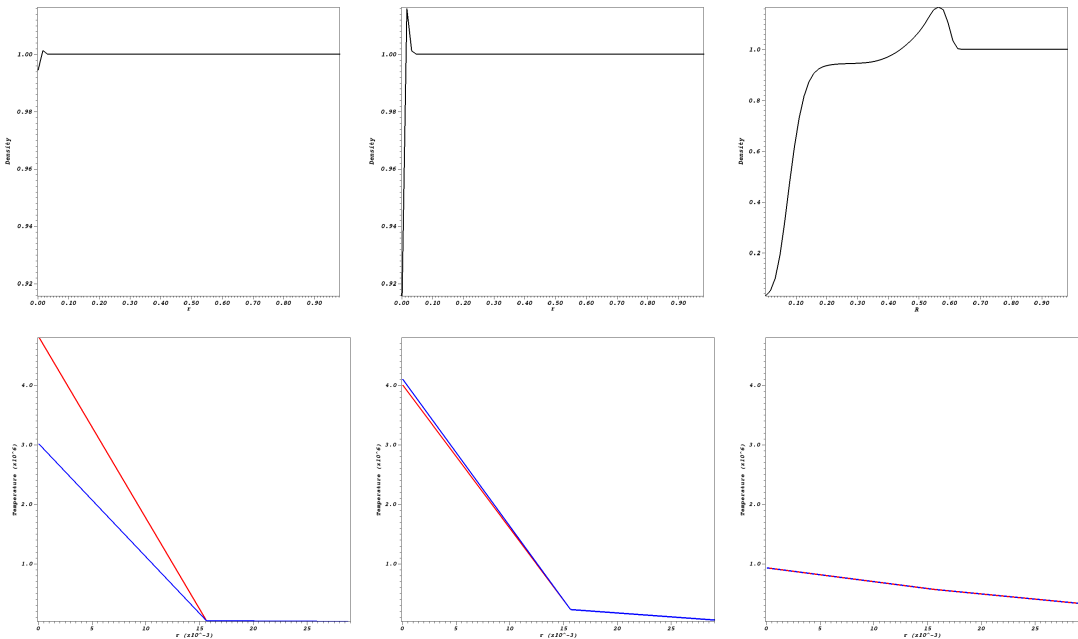


FIGURE 12. Sedov injection in 2D Cartesian geometry. 1D profile at Left: $t = 6.73 \times 10^{-10}$ s, Middle: $t = 6.73 \times 10^{-9}$ s, Right: $t = 9.7634 \times 10^{-6}$ s, Top: Density. Bottom: Electron (red) and Ion (blue) temperatures.

Figure 19 and Table 4 summarize the setting of the problem: the sub-domain Ω_1 is initially a domain of high density and low temperatures, it is given by the disc of radius 0.1414 of center point $(0.5, -0.5)$. The sub-domain Ω_3 is characterized by a low density and high temperatures and defined by the disc of center $(0, 0)$ and radius equal to 0.707 without the part Ω_1 of this disc. Finally, the sub-domain Ω_2 is the rest of the computational domain and its average density and temperatures are chosen to be between the density and temperatures of the other two domains. We first comment on the differences in ion and electron temperatures for this test case. According to the

	ρ	\mathbf{u}	$T_e(\text{K})$	$T_i(\text{K})$	$p_e + p_i(\text{Pa})$
Ω_1	3	0	3.4812×10^6	2.3208×10^6	1.4348×10^{11}
Ω_2	1	0	2.78496×10^7	1.85664×10^7	3.8262×10^{11}
Ω_3	0.5	0	3.4812×10^7	2.3208×10^7	2.3914×10^{11}

TABLE 4. Initial data of the three states of the triple points problem.

formula (4.1) giving the temperature relaxation times, the equilibrium time varies as $T^{3/2}$. More precisely, at time $t = 0$, the temperature relaxation times in the three domains are

$$(86) \quad t_{\Omega_1} = 8.51 \times 10^{-11} \text{ s}, \quad t_{\Omega_2} = 3.86 \times 10^{-9} \text{ s}, \quad t_{\Omega_3} = 1.00 \times 10^{-8} \text{ s}.$$

Hence we expect temperature equilibrium to be reached rapidly in domain Ω_1 while domain Ω_3 will be the last one where temperature equilibrium will occur.

Figure 20 displays the ratio $\frac{T_i - T_e}{T_e}$ at three different times. At $t = 2.1 \times 10^{-9}$ s, we can see that only the sub-domain

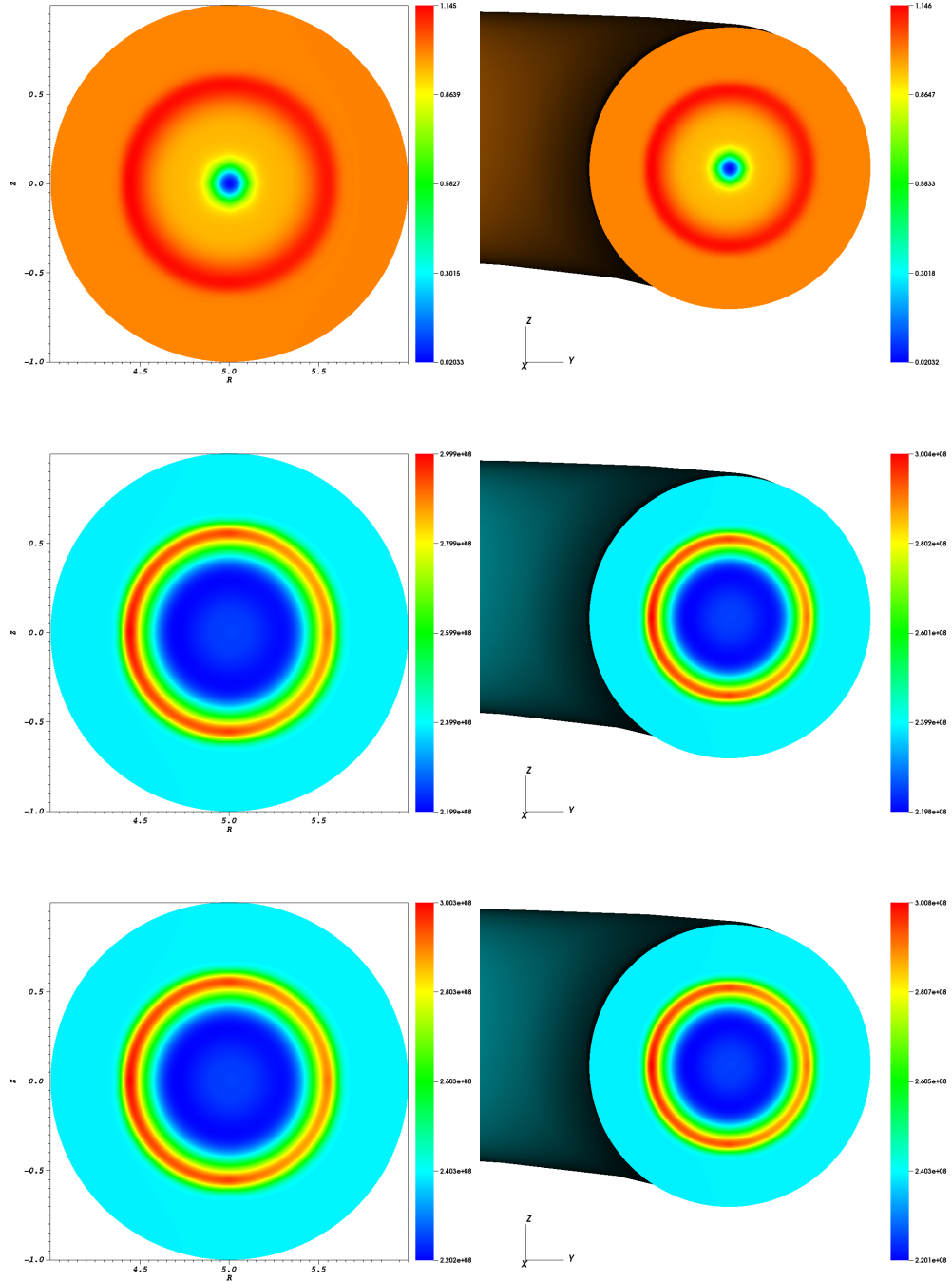


FIGURE 13. Sedov injection in axisymmetric toroidal geometry at $t = 9.7634 \times 10^{-6}$ s. Comparison of the 2D axisymmetric and 3D computations. Left: 2D run, Right: 3D run, Top: Density, Center: Electron pressure, Bottom: Ion pressure.

Ω_1 gets equal temperatures. Then, at $t = 4.7 \times 10^{-9}$ s, the cold and the intermediate sub-domains have reached the equilibrium. Finally, after $t = 1.35 \times 10^{-8}$ s, the electron and the ion temperatures are equal in all the domain.

The results are at $t = 1.1574 \times 10^{-5}$ s, and are given in Figure 21. The initial cold and dense domain Ω_1 corresponds to a zone of low pressure. Therefore it has been crushed by the high pressure neighbouring zones and has expanded mainly in the angular direction. Another noticeable result is that at this time, the density and temperatures have been smoothed out: while the initial density was in the interval $[0.5, 3]$, it is now between 0.5321 and 2.032 and the same smoothing effect can be noticed for the temperature. This effect is mainly due to pressure reflection on the boundary of the domain. Indeed, a rough estimate of the sound speed at time $t = 0$ ($c_s \approx 8.92816 \times 10^5$ m.s $^{-1}$) shows that at $t = 1.1574 \times 10^{-5}$ s, pressure waves have crossed the domain around 5 times leading to a smoothing of the density and temperature fields.

4.7. Triple point problem in the plane of a torus with axisymmetry initialization. As in Section 4.4 we now reproduce the previous test case in the geometry of a torus. The aim of this test case is to see the influence

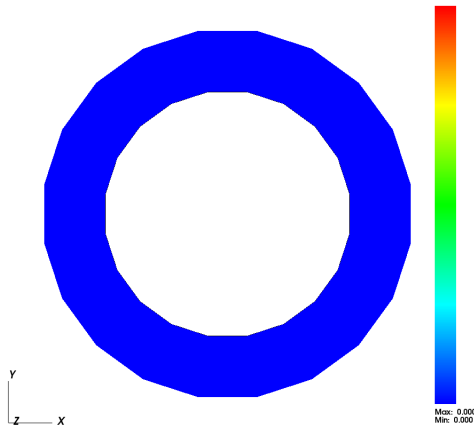


FIGURE 14. Sedov injection in 3D toroidal geometry, toroidal velocity u_φ at $t = 9.7634 \times 10^{-6}$ s along $Z = 0$.

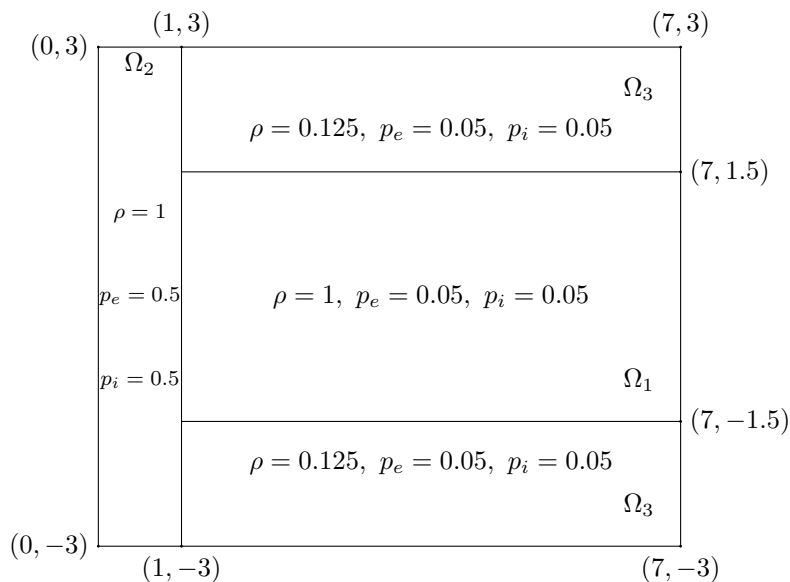


FIGURE 15. Initialization of the triple point problem in a rectangle.

of the geometry. We set the major radius of the torus at 3. We have also performed two simulations: the first one is a pure 2D axisymmetric computation while the second is a true 3-D one where the toroidal direction has been discretized with 20 planes. We have checked that the 3D runs maintain the 2D axisymmetric character of the solution and that no toroidal velocity has been created.

Since the results between the 3D and the 2D axisymmetric are extremely close, we present only the ones of the 2D axisymmetric simulation.

The results are given in Figure 22. We see that the average domain Ω_2 expands more to the initial hot domain in the area closer to the center of the torus. This phenomenon can be due to centripetal or centrifugal forces. Moreover, the final temperatures are quite different of the 2D Cartesian case. Indeed, for the cold domain, we obtain 8.738×10^6 K for the electron and ion temperatures of the cold domain instead of 9.055×10^6 K. Then, we can suppose that the evolution is slower in the cylindrical case than in the Cartesian one. We also remark, that the final shape of the cold domain Ω_1 is not anymore symmetric and the temperature is hotter closer to torus center than to the exterior side. Likewise, the density is higher in the torus center zone than the exterior, and the final value of the domain Ω_1 is 2.092 instead of 2.032. In fact, the cold domain seems to move to the exterior of the torus. At the end of the simulation, as expected the electron and ion temperatures are balanced. In Figure 23, we compare the velocity in the poloidal plane (R, Z) to the one of the Cartesian run. We can see that for the cylindrical geometry, the velocity is around twice the maximum of velocity of the Cartesian run. Indeed, around the border between the hot domain and the average domain closer to the center of the torus, the velocity of the axisymmetric run is about four times the one of the Cartesian geometry.

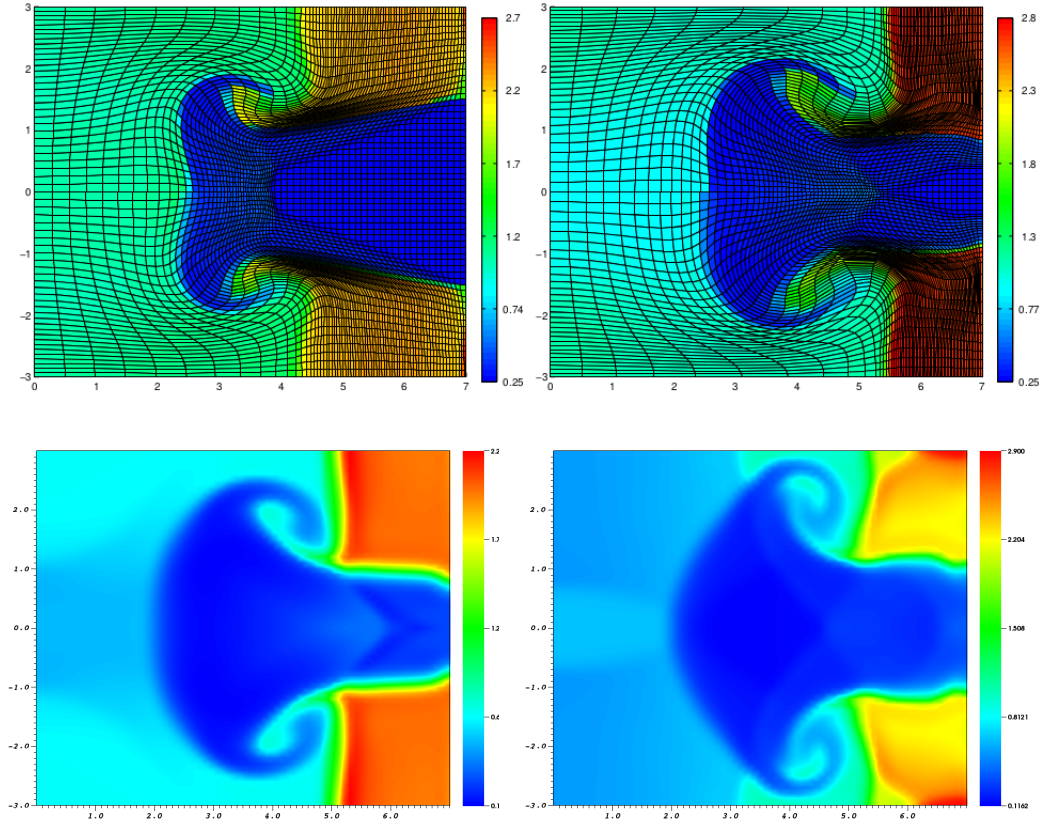


FIGURE 16. Triple point problem total internal energy at $t = 3.5$ s (left) and at $t = 5.0$ s, Top: Results from [22] for mono-temperature Euler equations where the top of the domain is obtained with the Volume of Fluid method and the bottom of the domain with the concentration equations, Bottom: Relaxation scheme for two-temperature Euler equations.

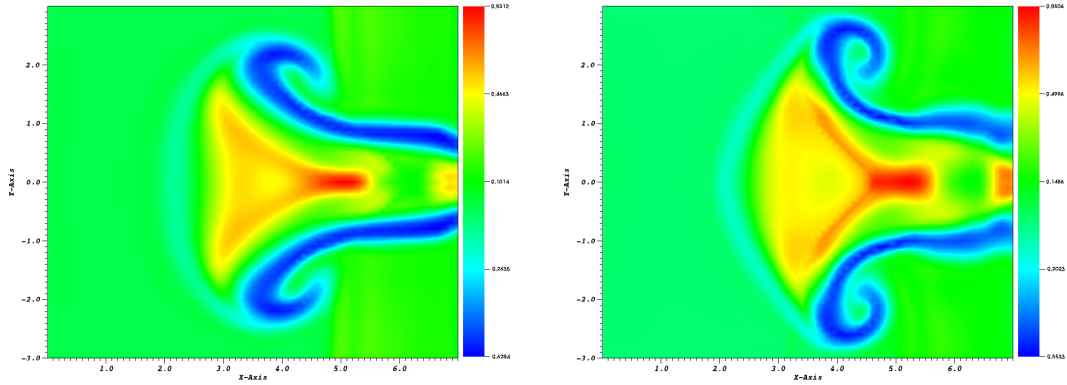


FIGURE 17. Triple point problem, $\frac{T_i - T_e}{T_e}$ 2D field at $t = 3.5$ s (Left), and $t = 5.0$ s (Right).

It follows from the above two last numerical tests that the geometry is an important input, since it largely modifies quantitatively and qualitatively the behaviour of the velocity field.

4.8. Triple point problem in 3-D toroidal geometry. Here, we propose a fully 3D numerical test in toroidal geometry. This test is based on the two previous cases, but instead of having an axisymmetric initialization, we consider that the initial cold and dense zone is a small cylinder. The periodic toroidal direction is meshed in a regular manner with 20 points and we assume that the zone where the cylinder is localized corresponds to the angular domain $[0, 3 \times 2\pi/20]$. In the domain where the cylinder is localized, a three state initialization is used while in the rest of the domain the fields are described by two different states. The different domains of the poloidal planes are described in Figure 24, and the initialization used for the domain Ω_1 , Ω_2 , and Ω_3 is given in Table 4. The three poloidal planes that intersect the cylinder as numbered as the poloidal planes 1, 2, and 3 while the two neighbouring planes are numbered the planes 4 and 20.

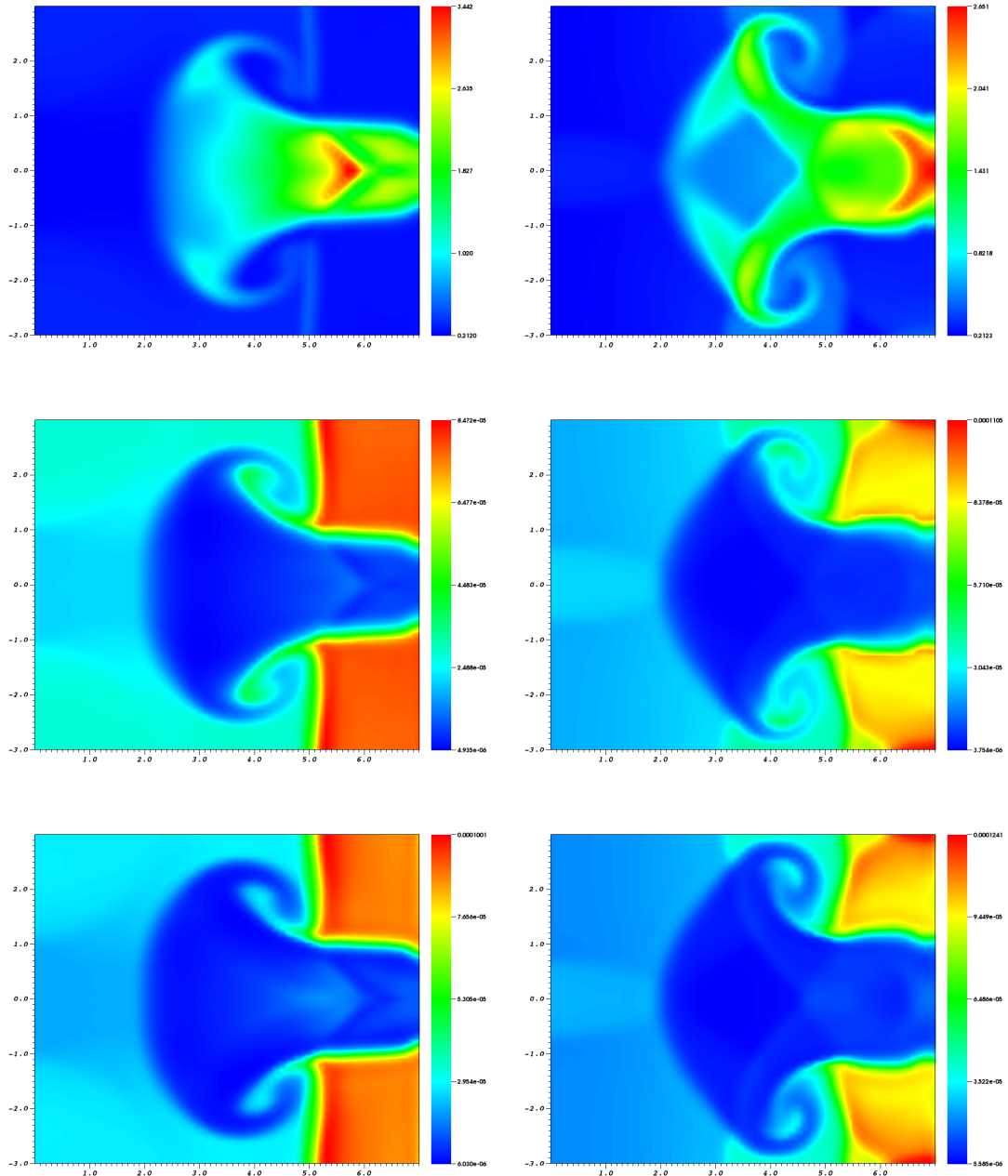
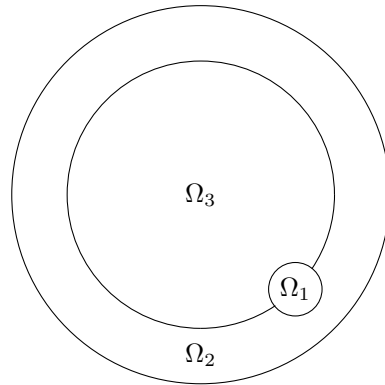
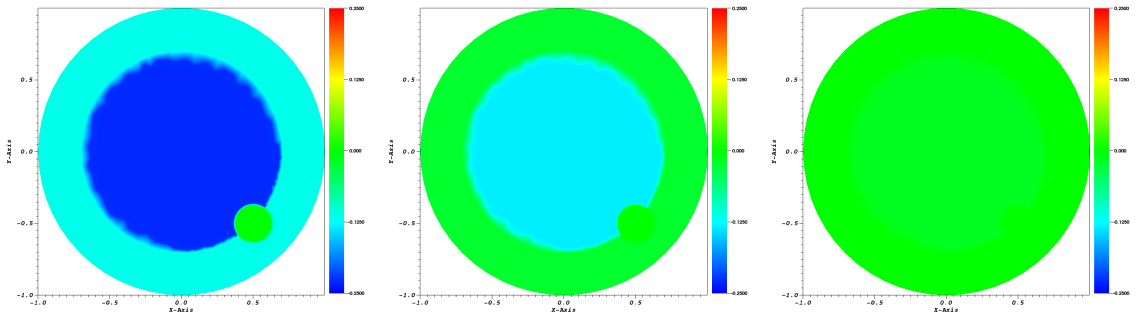


FIGURE 18. Triple point problem at $t = 3.5$ s (Left), and $t = 5$ s (Right). 2D fields of Top: Density, Middle: Electron temperature, Bottom: Ion temperature.

Figs. 25, 26, 27 and 28 display the results in the planes 1 to 3, 4, 20 and 10. They show that the extrema are reduced with respect to the 2D case. For instance, in the 3D case, the extrema are 0.46 and 1.867 instead of 0.5051 and 2.092 in the 2D axisymmetric case. But, globally, the evolution of the solution is similar to the one described for an axisymmetric initial state except for the total pressure. We can however note that we have a 3 dimensional effect in the toroidal direction leading to a increased smoothing of the extrema in the 3D case although this effect seems to be weak, up to this time. Such a computation would require a much denser mesh in the toroidal direction to give meaningful results.

5. CONCLUSION

In this work, the two-temperature Euler plasma model has been derived from the two-fluid MHD model. The two-temperature Euler plasma model considers the ion-electron mixture as a single fluid that retains two temperature or energy equations to describe the thermodynamics of the mixture. The two-temperature Euler model is identified as a limit for large plasma β parameter of the two-fluid model. Along this study, we have shown that assumptions in previous derivations in literature are straightforward consequences of our work. For smooth solutions, this model can be written under several different forms. Here, we have used a conservative form of the equations where instead

FIGURE 19. The three domain of the triple point problem in the (R, Z) plane.FIGURE 20. Triple point problem in Cartesian geometry. $\frac{T_i - T_e}{T_e}$ 2-D fields at $t = 2.1 \times 10^{-9}$ s (left), $t = 4.7 \times 10^{-9}$ s (middle), and $t = 1.35 \times 10^{-8}$ s (right).

of the two non-conservative temperature equations, we preferred the conservative total energy equation complemented by a conservative equation for the electron entropy. While the preservation of the total energy equation must be respected by any model, other choices than the conservative form for the electron entropy can be used and our choice is only motivated by the fact that due to the light mass of the electrons, the variations of electron entropies can be large without affecting too much the total internal energy. With this choice, a relaxation scheme is suggested to solve the two-temperature Euler plasma model in Cartesian as well that in cylindrical coordinates by a finite volume method. The interest for cylindrical coordinate system is motivated by possible future applications to Magnetic Confinement Fusion and tokamaks.

Finally, we have addressed several different numerical tests using the two coordinate systems and different geometries. The results have shown that the numerical scheme is able to simulate problems with large densities and pressure differences as well as fast phenomena. In the geometry of a torus, the suggested finite volume method has been tested on 3D test cases and has demonstrated its capability to keep the axisymmetric character of the solutions which is an important feature for MCF applications. Future work on this topic will involve its extension to bounded plasma β parameter and the introduction of magnetic field and dissipative terms.

APPENDIX A. PRACTICAL TOOLS FOR NUMERICAL IMPLEMENTATION: NORMALS, SURFACES

A.1. Measure of the surface of the control cell in (R, Z) -coordinates. Consider a tessellation of the poloidal plane composed of N_t triangles in (R, Z) -coordinates. The ι_{2D} th control cell $\Omega_{\iota_{2D}}^{2D}$, associated to ι_{2D} th vertex is given by

$$(87) \quad \Omega_{\iota_{2D}}^{2D} = \cup_{\ell_{2D}} \Omega_{\ell_{2D}}^{2D(\ell_{2D})},$$

where the union covers to all the triangles sharing the ι_{2D} th vertex and $\Omega_{\ell_{2D}}^{2D(\ell_{2D})}$ denotes the subset of the triangle $T_{\ell_{2D}}$ that enters in the construction a vertex-cell approach as defined in section 3.2 and displayed in Figure 1. The measure of surface of the control cell $\Omega_{\iota_{2D}}^{2D(\ell_{2D})}$ is given by

$$(88) \quad |\Omega_{\iota_{2D}}^{2D}| = \int_{\Omega_{\iota_{2D}}^{2D}} R dR dZ.$$

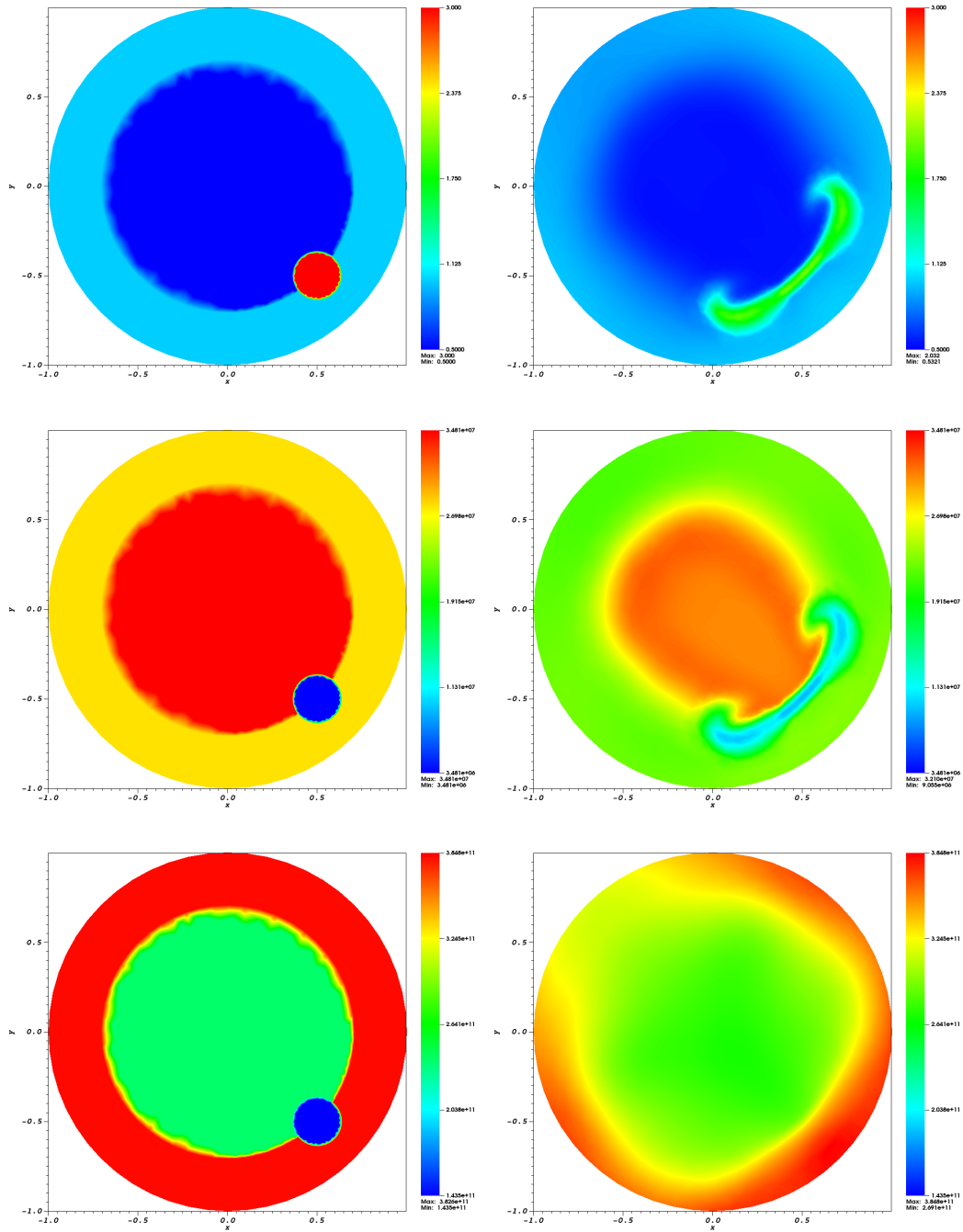


FIGURE 21. Triple point problem in Cartesian geometry. Initial data (Left) and solution at $t = 1.1574 \times 10^{-5}$ s (Right). Top: Density, Center: Electron temperature, Bottom: Total pressure.

From (87), we get:

$$(89) \quad |\Omega_{\iota_{2D}}^{2D}| = \sum_{\ell_{2D}} |\Omega_{\ell_{2D}}^{2D(\ell_{2D})}|,$$

where

$$(90) \quad |\Omega_{\ell_{2D}}^{2D(\ell_{2D})}| = \int_{\Omega_{\ell_{2D}}^{2D(\ell_{2D})}} R dR dZ.$$

Let the triangle $T_{\ell_{2D}}$ that enters in the construction of $\Omega_{\ell_{2D}}^{2D(\ell_{2D})}$, and ι_{2D} , q_{2D} , k_{2D} its vertices. The coordinates of the center of gravity $G_{\iota_{2D}, T_{\ell_{2D}}}$ of the triangle $T_{\ell_{2D}}$ are given by

$$\begin{cases} R_{G_{\iota_{2D}, T_{\ell_{2D}}}} = \frac{R_{\iota_{2D}} + R_{q_{2D}} + R_{k_{2D}}}{3}, \\ Z_{G_{\iota_{2D}, T_{\ell_{2D}}}} = \frac{Z_{\iota_{2D}} + Z_{q_{2D}} + Z_{k_{2D}}}{3}, \end{cases}$$

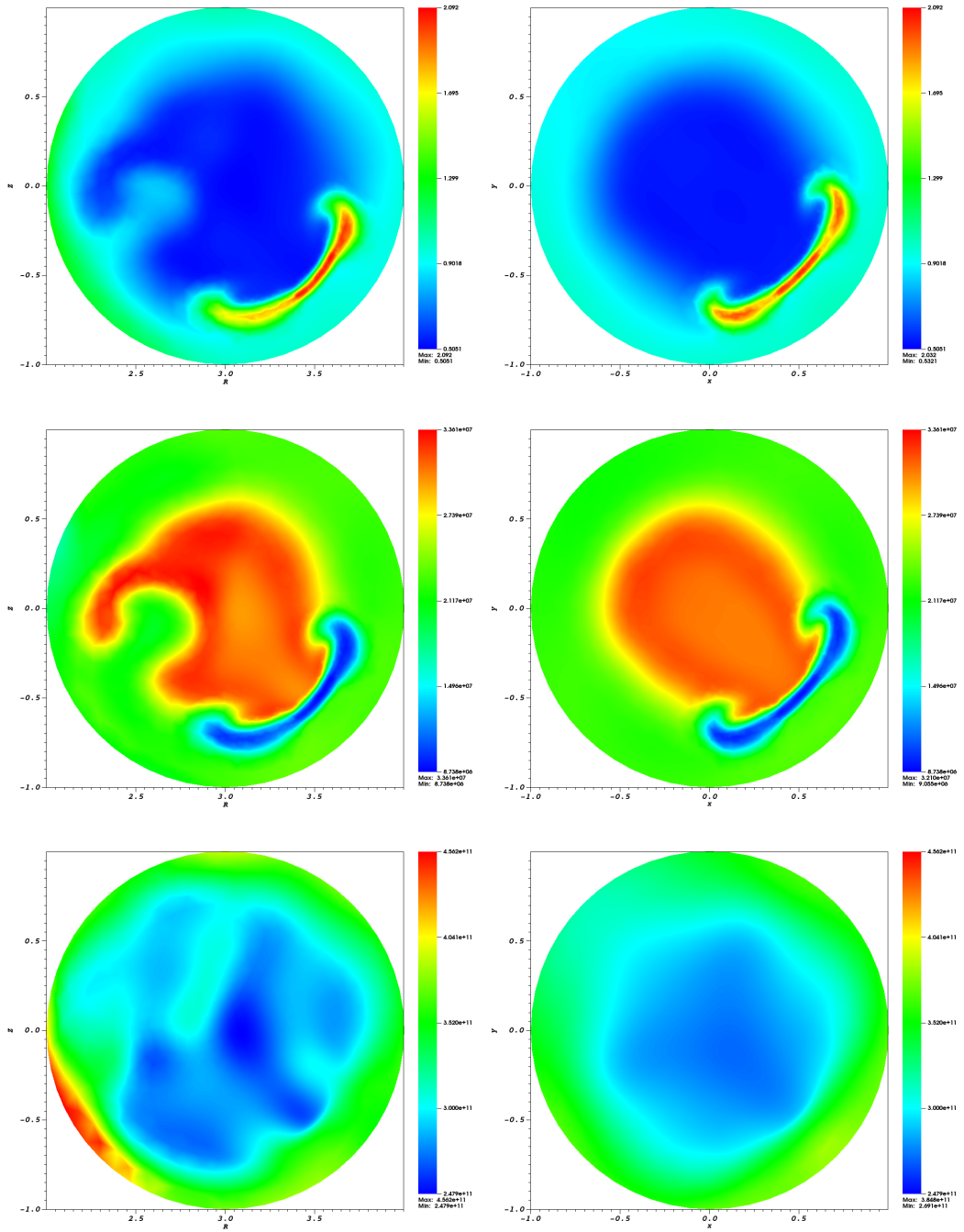


FIGURE 22. Triple point problem at $t = 1.1574 \times 10^{-5}$ s. Comparison of the results obtained in Cartesian geometry and in a torus. Left: 2D axisymmetric run, Right: 2D Cartesian run. Top: Density, Center: electron temperature, Bottom: total pressure.

where $R_{\iota_{2D}}$, $R_{q_{2D}}$, $R_{k_{2D}}$ are the coordinates of the vertices ι_{2D} , q_{2D} and k_{2D} along the R -axis. The coordinates of those points along the Z -axis are $Z_{\iota_{2D}}$, $Z_{q_{2D}}$, $Z_{k_{2D}}$.

The integral $\int_{\Omega_{\iota_{2D}, T_{\ell_{2D}}}^{2D}} R dR dZ$ can be rewritten as

$$(91) \quad \int_{\Omega_{\iota_{2D}, T_{\ell_{2D}}}^{2D}} R dR dZ = \int_{\Omega_{\iota_{2D}, T_{\ell_{2D}}}^{2D, 1}} R dR dZ + \int_{\Omega_{\iota_{2D}, T_{\ell_{2D}}}^{2D, 2}} R dR dZ,$$

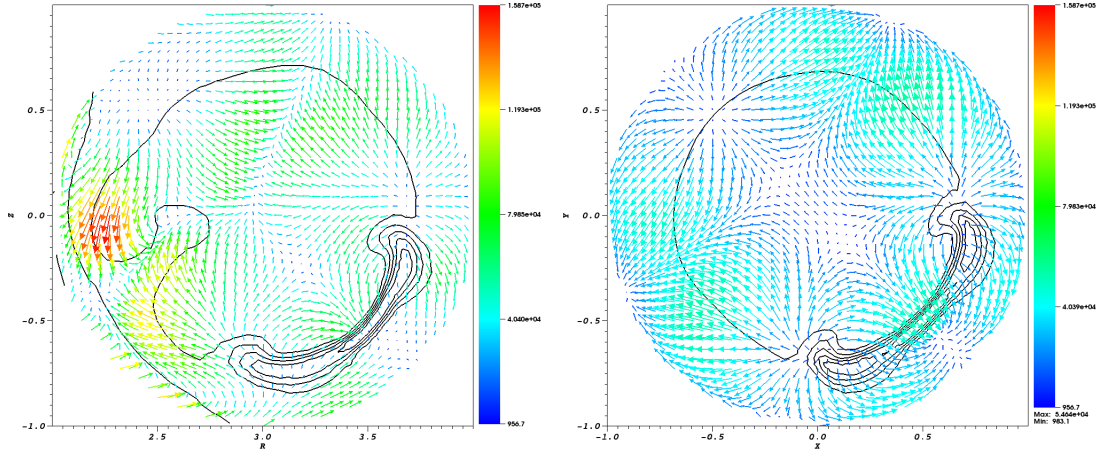


FIGURE 23. Triple point problem at $t = 1.1574 \times 10^{-5}$ s. Comparison of the results obtained in Cartesian geometry and in a torus. Velocity vectors with density contours. Left: 2D axisymmetric run, Right: 2D Cartesian run.

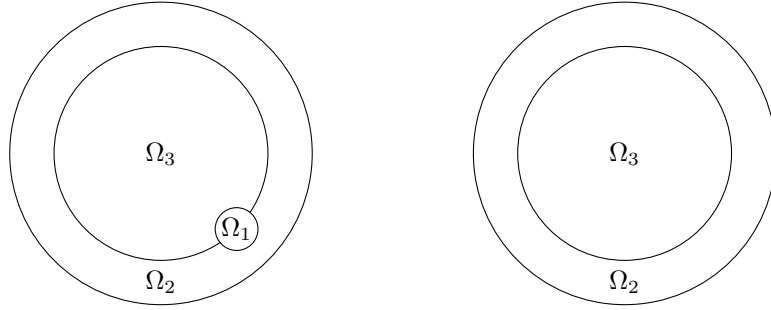


FIGURE 24. Triple point problem initial domain in 3D toroidal geometry. Left: for the poloidal planes 1 to 3. Right: for the rest of the poloidal planes (4 to 20).

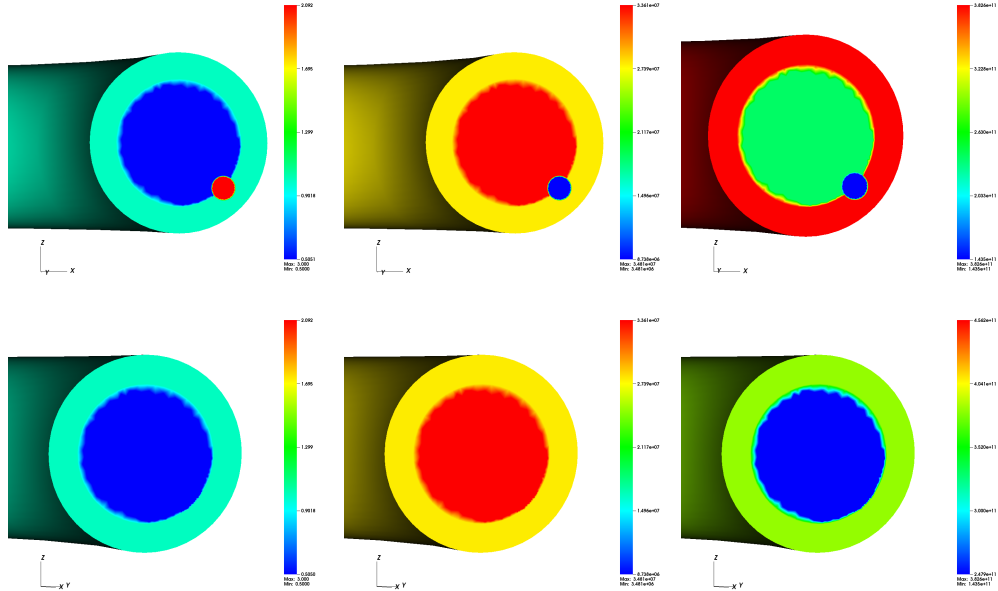


FIGURE 25. Triple point problem initialization. Top: poloidal planes 1 to 3, Bottom: poloidal planes 4 to 20. Left: density, Center: electron temperature, Right: total pressure.

where the triangles $\Omega_{\ell_{2D}, T_{\ell_{2D}}}^{2D,1}$ and $\Omega_{\ell_{2D}, T_{\ell_{2D}}}^{2D,2}$ are depicted in Figure 29. Since the map $(R, Z) \mapsto R$ is linear, each integral in RHS of (91) is exactly computed by the midpoint formula

$$\begin{cases} \int_{\Omega_{\ell_{2D}, T_{\ell_{2D}}}^{2D,1}} R dR dZ = R_{G_{\ell_{2D}, T_{\ell_{2D}}}^1} \int_{\Omega_{\ell_{2D}, T_{\ell_{2D}}}^{2D,1}} dR dZ = R_{G_{\ell_{2D}, T_{\ell_{2D}}}^1} \left| \Omega_{\ell_{2D}, T_{\ell_{2D}}}^{2D,1} \right|, \\ \int_{\Omega_{\ell_{2D}, T_{\ell_{2D}}}^{2D,2}} R dR dZ = R_{G_{\ell_{2D}, T_{\ell_{2D}}}^2} \int_{\Omega_{\ell_{2D}, T_{\ell_{2D}}}^{2D,2}} dR dZ = R_{G_{\ell_{2D}, T_{\ell_{2D}}}^2} \left| \Omega_{\ell_{2D}, T_{\ell_{2D}}}^{2D,2} \right|, \end{cases}$$

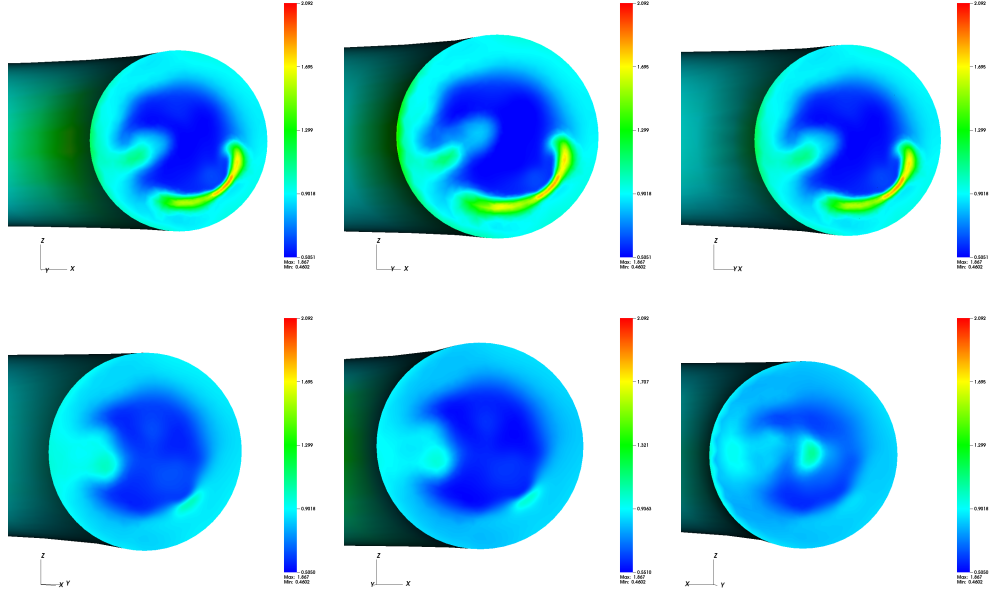


FIGURE 26. Triple point problem in 3D toroidal geometry. Density at $t = 1.1574 \times 10^{-5}$ s. Top-Left: Plane 1, Top-Center: Plane 2, Top-Right: Plane 3, Bottom-Left: Plane 4, Bottom-Center: Plane 20, Bottom-Right: Plane 10.

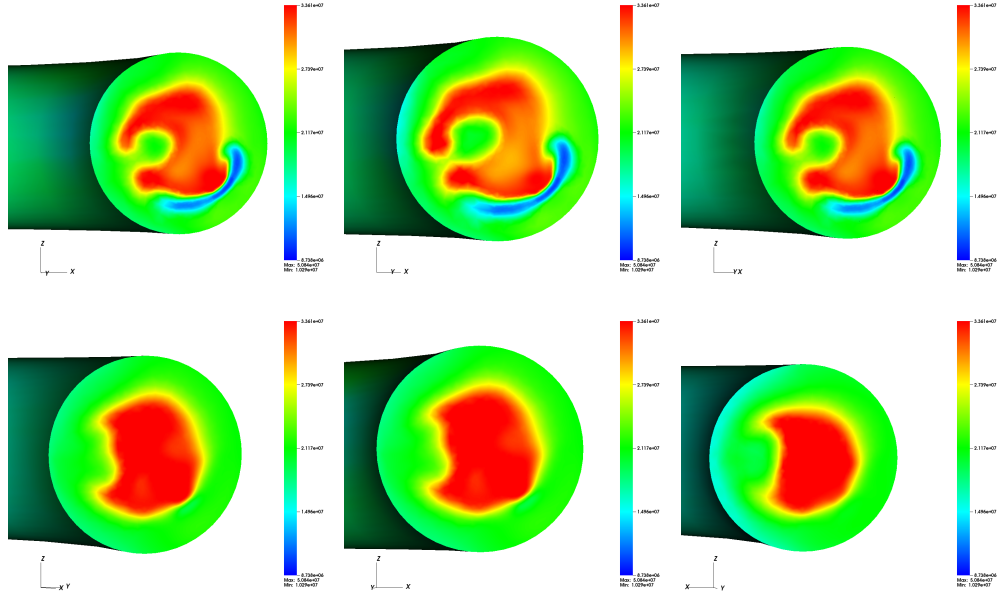


FIGURE 27. Triple point problem in 3D toroidal geometry. Electron temperature at $t = 1.1574 \times 10^{-5}$ s. Top-Left: Plane 1, Top-Center: Plane 2, Top-Right: Plane 3, Bottom-Left: Plane 4, Bottom-Center: Plane 20, Bottom-Right: Plane 10.

where $G_{l_{2D}, T_{\ell_{2D}}}^1$ and $G_{l_{2D}, T_{\ell_{2D}}}^2$ are the coordinates of the centers of gravity of the triangles $\Omega_{l_{2D}, T_{\ell_{2D}}}^{2D, 1}$ and $\Omega_{l_{2D}, T_{\ell_{2D}}}^{2D, 2}$ whereas $|\Omega_{l_{2D}, T_{\ell_{2D}}}^{2D, 1}|$ and $|\Omega_{l_{2D}, T_{\ell_{2D}}}^{2D, 2}|$ are their areas in the logical 2D plane R, Z , respectively. The quantities $R_{G_{l_{2D}, T_{\ell_{2D}}}^1}$ and $R_{G_{l_{2D}, T_{\ell_{2D}}}^2}$ are given by

$$\begin{cases} R_{G_{l_{2D}, T_{\ell_{2D}}}^1} = \frac{R_{l_{2D}} + \frac{R_{l_{2D}} + R_{q_{2D}}}{2} + R_{G_{l_{2D}, T_{\ell_{2D}}}}}{3} = \frac{11}{18} R_{l_{2D}} + \frac{5}{18} R_{q_{2D}} + \frac{2}{18} R_{k_{2D}}, \\ R_{G_{l_{2D}, T_{\ell_{2D}}}^2} = \frac{R_{l_{2D}} + \frac{R_{l_{2D}} + R_{k_{2D}}}{2} + R_{G_{l_{2D}, T_{\ell_{2D}}}}}{3} = \frac{11}{18} R_{l_{2D}} + \frac{2}{18} R_{q_{2D}} + \frac{5}{18} R_{k_{2D}}. \end{cases}$$

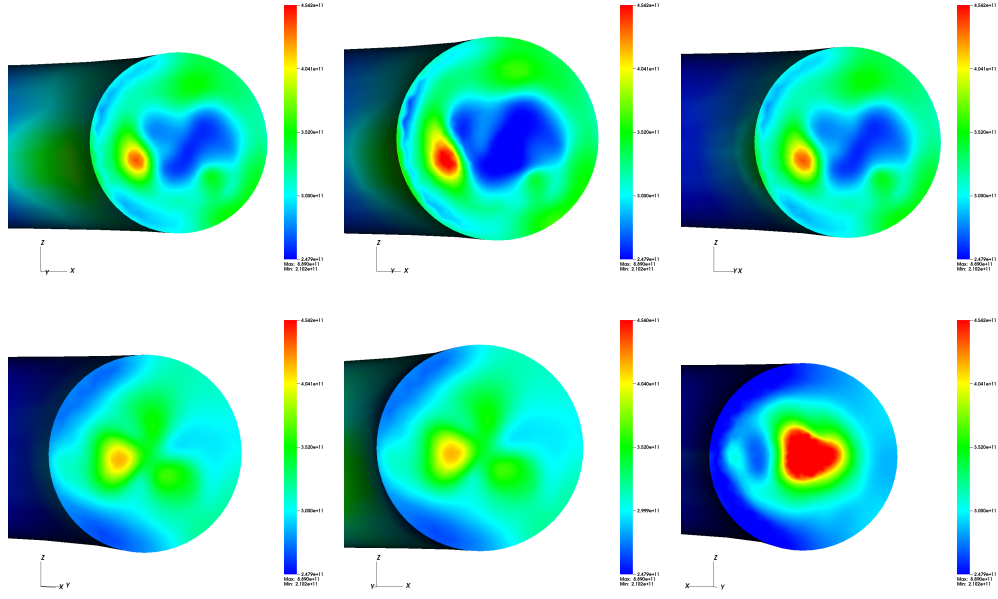


FIGURE 28. Triple point problem in 3D toroidal geometry. Total pressure at $t = 1.1574 \times 10^{-5}$ s. Top-Left: Plane 1, Top-Center: Plane 2, Top-Right: Plane 3, Bottom-Left: Plane 4, Bottom-Center: Plane 20, Bottom-Right: Plane 10.

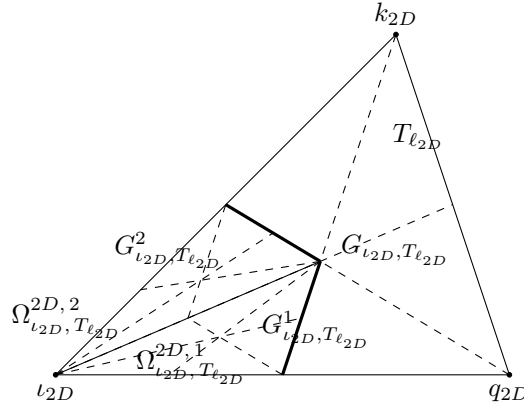


FIGURE 29. The triangle that enters in the construction of a control cell $\Omega_{l_{2D}}^{2D(\ell)}$ in the (R, Z) -plane.

The triangles $\Omega_{l_{2D}, T_{l_{2D}}}^{2D, 1}$ and $\Omega_{l_{2D}, T_{l_{2D}}}^{2D, 2}$ owe the same area in the logical 2D plane R, Z , given by

$$\left| \Omega_{l_{2D}, T_{l_{2D}}}^{2D, 1} \right| = \left| \Omega_{l_{2D}, T_{l_{2D}}}^{2D, 2} \right| = \frac{|T_{l_{2D}}|}{6},$$

where

$$|T_{l_{2D}}| = \frac{1}{2} \left| (R_{q_{2D}} - R_{l_{2D}})(Z_{k_{2D}} - Z_{l_{2D}}) - (R_{k_{2D}} - R_{l_{2D}})(Z_{q_{2D}} - Z_{l_{2D}}) \right|.$$

Therefore, the integral $\int_{\Omega_{l_{2D}, T_{l_{2D}}}^{2D}} R dR dZ$ is provided by

$$\int_{\Omega_{l_{2D}, T_{l_{2D}}}^{2D}} R dR dZ = R_{l_{2D}}^{T_{l_{2D}}} \frac{|T_{l_{2D}}|}{6},$$

where

$$\begin{aligned} R_{l_{2D}}^{T_{l_{2D}}} &= \left(\frac{11}{18} R_{l_{2D}} + \frac{5}{18} R_{q_{2D}} + \frac{2}{18} R_{k_{2D}} \right) + \left(\frac{11}{18} R_{l_{2D}} + \frac{2}{18} R_{q_{2D}} + \frac{5}{18} R_{k_{2D}} \right) \\ &= \frac{11}{9} R_{l_{2D}} + \frac{7}{18} (R_{q_{2D}} + R_{k_{2D}}). \end{aligned}$$

Finally, the measure of the surface of the control cell $\Omega_{l_{2D}}$ is given by:

$$(92) \quad \left| \Omega_{l_{2D}}^{2D} \right| = \sum_{l_{2D}} R_{l_{2D}}^{T_{l_{2D}}} \frac{|T_{l_{2D}}|}{6}.$$

A.2. Measure of the volume of a 3D control cell in (R, Z) -coordinates. We keep the setting of the 2D control cell $\Omega_{\ell_{2D}}^{2D}$, used in Appendix A.1, and consider the 3D control cell Ω_ℓ built on it, in particular:

$$(93) \quad \Omega_\ell = \prod_{\varphi \in [\varphi_{j-1/2}, \varphi_{j+1/2}]} \mathcal{R}_\varphi (\Omega_{\ell_{2D}}^{2D}),$$

where \mathcal{R}_φ stands for the rotation around φ about the Z -axis. The notation (93) means that Ω_ℓ is the 3D physical volume swept by the rotation of the 2D control cell $\Omega_{\ell_{2D}}^{2D}$ from $\varphi_{j-1/2}$ to $\varphi_{j+1/2}$ about the Z -axis. Immediately, thanks to Appendix A.1, the measure of the volume of the 3D control cell Ω_ℓ is:

$$(94) \quad |\Omega_\ell| = \int_{\varphi_{j-1/2}}^{\varphi_{j+1/2}} d\varphi \int_{\Omega_{\ell_{2D}}^{2D}} R dR dZ = \sum_{\ell_{2D}} \int_{\varphi_{j-1/2}}^{\varphi_{j+1/2}} d\varphi \int_{\Omega_{\ell_{2D}}^{2D(\ell)}} R dR dZ = \sum_{\ell_{2D}} \Delta\varphi_\ell R_{\ell_{2D}}^{T_{\ell_{2D}}} \frac{|T_{\ell_{2D}}|}{6},$$

where: $\Delta\varphi_\ell = \varphi_{j+1/2} - \varphi_{j-1/2}$.

A.3. Normals of boundary surfaces of a cell control. We still consider a 3D control cell Ω_ℓ devised on the 2D control cell $\Omega_{\ell_{2D}}^{2D}$:

$$(95) \quad \Omega_\ell = \prod_{\varphi \in [\varphi_{j-1/2}, \varphi_{j+1/2}]} \mathcal{R}_\varphi (\Omega_{\ell_{2D}}^{2D}),$$

where \mathcal{R}_φ stands for the rotation around φ about the Z -axis.

We are interested in the computation of the average unit outward normal of the interface $S_{\ell\ell}$:

$$(96) \quad \mathbf{n}_{\ell\ell} = \frac{\int_{S_{\ell\ell}} \mathbf{n} R d\partial\Omega_{\ell\ell}}{\|\int_{S_{\ell\ell}} \mathbf{n} R d\partial\Omega_{\ell\ell}\|},$$

where $S_{\ell\ell}$ are the boundary surfaces of Ω_ℓ . There are two kinds of boundary surfaces $S_{\ell\ell}$: the toroidal surfaces and the poloidal surfaces.

- The toroidal surfaces, always two, and are the revolved 2D surfaces $\Omega_{\ell_{2D}}^{2D}$, given by:

$$(97) \quad \Omega_{\ell_{2D}}^{2D,+} = \mathcal{R}_{\varphi_{j+1/2}} (\Omega_{\ell_{2D}}^{2D}), \quad \Omega_{\ell_{2D}}^{2D,-} = \mathcal{R}_{\varphi_{j-1/2}} (\Omega_{\ell_{2D}}^{2D}).$$

Immediately, the vectors $\widetilde{\mathbf{e}}_{\varphi_{j+1/2}}$ and $-\widetilde{\mathbf{e}}_{\varphi_{j-1/2}}$ are the average unit outward normals of the interface $\Omega_{\ell_{2D}}^{2D,+}$, and $\Omega_{\ell_{2D}}^{2D,-}$, respectively.

- The poloidal surfaces are surfaces swept by the segments of type $\Gamma_{\ell_{2D}\ell_{2D},1}$ and $\Gamma_{\ell_{2D}\ell_{2D},2}$, as shown in Figure 1, by the rotation from $\varphi_{j-1/2}$ to $\varphi_{j+1/2}$ about the Z -axis. Consider the poloidal surface $S_{\ell\ell}$ and the segment $\Gamma_{\ell_{2D}\ell_{2D}}$ in (R, Z) -plane such that

$$(98) \quad S_{\ell\ell} = \prod_{\varphi \in [\varphi_{j-1/2}, \varphi_{j+1/2}]} \mathcal{R}_\varphi (\Gamma_{\ell_{2D}\ell_{2D}}).$$

Let $\begin{pmatrix} n_R \\ n_Z \end{pmatrix}$ be the coordinates of the constant unit outward normal of $\Gamma_{\ell_{2D}\ell_{2D}}$ in (R, Z) -plane. Then at each point

of the surface $S_{\ell\ell}$, these components remain the same, however now expressed in the local basis, $\begin{pmatrix} n_{R_{\ell_{2D}\ell_{2D}}} \\ n_{Z_{\ell_{2D}\ell_{2D}}} \\ 0 \end{pmatrix}$

in $(\widetilde{\mathbf{e}}_R, \widetilde{\mathbf{e}}_Z, \widetilde{\mathbf{e}}_\varphi)$. Since $d\partial\Omega_{\ell\ell} = dLd\varphi$, where L is the curvilinear abscissa of the segment $\Gamma_{\ell_{2D}\ell_{2D}}$, we get

$$(99) \quad \begin{aligned} \int_{S_{\ell\ell}} \mathbf{n} R d\partial\Omega_{\ell\ell} &= \int_{\varphi \in [\varphi_{j-1/2}, \varphi_{j+1/2}], \Gamma_{\ell_{2D}\ell_{2D}}} \left(n_{R_{\ell_{2D}\ell_{2D}}} \widetilde{\mathbf{e}}_R + n_{Z_{\ell_{2D}\ell_{2D}}} \widetilde{\mathbf{e}}_Z \right) R(L) dL d\varphi \\ &= \int_{\varphi_{j-1/2}}^{\varphi_{j+1/2}} \left(n_{R_{\ell_{2D}\ell_{2D}}} \widetilde{\mathbf{e}}_R + n_{Z_{\ell_{2D}\ell_{2D}}} \widetilde{\mathbf{e}}_Z \right) d\varphi \int_{\Gamma_{\ell_{2D}\ell_{2D}}} R(L) dL \\ &= \left(\widetilde{\eta}_\ell n_{R_{\ell_{2D}\ell_{2D}}} \widetilde{\mathbf{e}}_R(\ell) + n_{Z_{\ell_{2D}\ell_{2D}}} \widetilde{\mathbf{e}}_Z(\ell) \right) \left(\Delta\varphi_\ell \int_{\Gamma_{\ell_{2D}\ell_{2D}}} R(L) dL \right), \end{aligned}$$

where: $\Delta\varphi_\ell = \varphi_{j+1/2} - \varphi_{j-1/2}$, $\widetilde{\eta}_\ell = \frac{\sin\left(\frac{\Delta\varphi_\ell}{2}\right)}{\frac{\Delta\varphi_\ell}{2}}$. The quantity $\Delta\varphi_\ell \int_{\Gamma_{\ell_{2D}\ell_{2D}}} R(L) dL$ is the measure of the surface $S_{\ell\ell}$:

$$|S_{\ell\ell}| = \Delta\varphi_\ell \int_{\Gamma_{\ell_{2D}\ell_{2D}}} R(L) dL.$$

We deduce

$$\int_{S_{\ell\ell}} \mathbf{n} R d\partial\Omega_{\ell\ell} = |S_{\ell\ell}| \left(\widetilde{\eta}_\ell n_{R_{\ell_{2D}\ell_{2D}}} \widetilde{\mathbf{e}}_R(\ell) + n_{Z_{\ell_{2D}\ell_{2D}}} \widetilde{\mathbf{e}}_Z(\ell) \right).$$

Therefore, we get :

$$(100) \quad \begin{aligned} \mathbf{N}_{i\ell} &= \frac{\int_{S_{i\ell}} \mathbf{n} R d\partial\Omega_{i\ell}}{|S_{i\ell}|} = \tilde{\eta}_i n_{R_{i2D}\ell_{2D}} \widetilde{\mathbf{e}_R(\ell)} + n_{Z_{i2D}\ell_{2D}} \widetilde{\mathbf{e}_Z(\ell)}, \\ \mathbf{n}_{i\ell} &= \frac{\int_{S_{i\ell}} \mathbf{n} R d\partial\Omega_{i\ell}}{\|\int_{S_{i\ell}} \mathbf{n} R d\partial\Omega_{i\ell}\|} = \frac{\mathbf{N}_{i\ell}}{\sqrt{\eta_i^2 n_{R_{i2D}\ell_{2D}}^2 + n_{Z_{i2D}\ell_{2D}}^2}}. \end{aligned}$$

Assume R_{i2D} , $R_{\ell_{2D}}$ are the coordinates of the points i_{2D} , ℓ_{2D} along the R -axis, while the coordinates of those points along the Z -axis are Z_{i2D} , $Z_{\ell_{2D}}$. The components $n_{R_{i2D}\ell_{2D}}$ and $n_{Z_{i2D}\ell_{2D}}$ are easily provided by:

$$n_{R_{i2D}\ell_{2D}} = \frac{Z_{\ell_{2D}} - Z_{i2D}}{\sqrt{(R_{\ell_{2D}} - R_{i2D})^2 + (Z_{\ell_{2D}} - Z_{i2D})^2}}, \quad n_{Z_{i2D}\ell_{2D}} = -\frac{R_{\ell_{2D}} - R_{i2D}}{\sqrt{(R_{\ell_{2D}} - R_{i2D})^2 + (Z_{\ell_{2D}} - Z_{i2D})^2}}.$$

APPENDIX B. USEFUL TRANSFORMATION IN THE RELAXATION STEP

We consider the 1D system (32). We show below that if $(\rho, \rho\mathbf{u}, \mathcal{E}, S_e)^T$ satisfies:

$$(101) \quad \begin{cases} \partial_t \rho &= & 0, \\ \partial_t \mathbf{u} &= & 0, \\ \partial_t \mathcal{E} &= & 0, \\ \partial_t S_e &= & (\gamma - 1) \nu_{ei} \rho_e^{-\gamma} (T_i - T_e), \end{cases}$$

then the system (101) is equivalent to:

$$(102) \quad \begin{cases} \partial_t \rho &= & 0, \\ \partial_t \mathbf{u} &= & 0, \\ \partial_t T_i &= & -\nu_{ei} (T_i - T_e), \\ \partial_t T_e &= & \nu_{ei} (T_i - T_e), \end{cases}$$

where $\nu_{ei} = \frac{\gamma - 1}{k_B n} \nu_{ei}^{\mathcal{E}}$.

We recall that : $\mathcal{E} = \frac{1}{2} \rho \mathbf{u} \cdot \mathbf{u} + \frac{k_B}{(\gamma - 1)(m_e + m_i)} \rho (T_i + T_e)$, $S_e = \frac{k_B}{m_e + m_i} \rho T_e (c_e \rho)^{-\gamma}$. Inserting these expressions in (101) leads to :

$$(103) \quad \begin{cases} \partial_t \rho &= & 0, \\ \partial_t \mathbf{u} &= & 0, \\ \partial_t (T_e + T_i) &= & 0, \\ \partial_t T_e &= & \nu_{ei} (T_i - T_e), \end{cases}$$

where $\nu_{ei} = \frac{\gamma - 1}{k_B n} \nu_{ei}^{\mathcal{E}}$, $n = \frac{\rho}{m_e + m_i}$. The system (103) is equivalent to:

$$(104) \quad \begin{cases} \partial_t \rho &= & 0, \\ \partial_t \mathbf{u} &= & 0, \\ \partial_t T_i &= & -\nu_{ei} (T_i - T_e), \\ \partial_t T_e &= & \nu_{ei} (T_i - T_e), \end{cases}$$

which could be solved exactly, leading to:

$$(105) \quad \begin{cases} \rho(t + \Delta t) = \rho(t), \\ \mathbf{u}(t + \Delta t) = \mathbf{u}(t), \\ \begin{pmatrix} T_i(t + \Delta t) \\ T_e(t + \Delta t) \end{pmatrix} = \frac{1}{2} \begin{pmatrix} (T_i(t) + T_e(t)) + (T_i(t) - T_e(t)) e^{-2\nu_{ei}\Delta t} \\ (T_i(t) + T_e(t)) - (T_i(t) - T_e(t)) e^{-2\nu_{ei}\Delta t} \end{pmatrix}. \end{cases}$$

First, we check that if $T_i(t) = T_e(t)$ at a given time $t \geq 0$, then by (104), we get $T_i(t + \Delta t) = T_e(t + \Delta t)$ as it should be. Second, the positiveness of $T_i(t + \Delta t)$ and $T_e(t + \Delta t)$ under the assumption $T_i(t) > 0$, $T_e(t) > 0$, at a given time $t \geq 0$ is obtained since the two last equations of (104) could be rewritten as:

$$(106) \quad \begin{cases} T_i(t + \Delta t) = \frac{1 + e^{-2\nu_{ei}\Delta t}}{2} T_i(t) + \frac{1 - e^{-2\nu_{ei}\Delta t}}{2} T_e(t) > 0, \\ T_e(t + \Delta t) = \frac{1 + e^{-2\nu_{ei}\Delta t}}{2} T_e(t) + \frac{1 - e^{-2\nu_{ei}\Delta t}}{2} T_i(t) > 0. \end{cases}$$

REFERENCES

- [1] D. ARÉGBA-DRIOLLET, J. BREIL, S. BRULL, B. DUBROCA, AND E. ESTIBALS, *Modelling and numerical approximation for the non-conservative bitemperature Euler model*, ESAIM : Mathematical Modelling and Numerical Analysis, **52(4)**: 1353-1383, 2018.
- [2] S. ATZENI, J. MEYER-TER-VEHN, *The physics of Inertial Fusion, Beam Plasma Interaction, Hydrodynamics, Hot Dense Matter*, International Series of Monographs on Physics, Volume **125**, Oxford Sciences Publications, Oxford University Press (2009).
- [3] R. BALESCU, *Transport Processes in Plasmas, Classical transport theory*, **1**, North Holland, Amsterdam (1988).
- [4] R. BALESCU, *Transport Processes in Plasmas, Classical transport theory*, **2**, North Holland, Amsterdam (1988).
- [5] C. BERTHON, F. COQUEL, P.G. LEFLOCH, Why many theories of shock waves are necessary: kinetic relations for non-conservative systems, *Proceedings of the Royal Society of Edinburgh: Section A Mathematics*, **142**, 1-37 (2012).
- [6] C. BERTHON, B. DUBROCA, A. SANGAM, An Entropy Preserving Relaxation Scheme For Ten-Moments Equations with Source Terms, *Communications in Mathematical Sciences*, **13**, 2119-2154 (2015).
- [7] S. I. BRAGINSKII, *Transport Processes in Plasmas, Reviews of Plasma Physics*, **1**, 205, Consultant Bureau, New York (1965).
- [8] M. BILANCERI, L. COMBE, H. GUILLARD, B. NKONGA, A. SANGAM, A 3D Finite Volume Scheme For The Simulation Of Edge Plasma In Tokamak, *ESAIM Proceedings*, **43**, 164-179 (2013).
- [9] A. BONNEMENT, T. FAJRAOUL, H. GUILLARD, M. MARTIN, A. MOUTON, B. NKONGA, A. SANGAM, Finite Volume Method in Curvilinear Coordinates, *ESAIM Proceedings*, **32**, 163-176 (2011).
- [10] F. BOUCHUT, *Nonlinear stability of finite volume methods for hyperbolic conservation laws, and well-balanced schemes for sources*, Frontiers in Mathematics series, Birkhäuser (2004).
- [11] C. COHEN-TANNOUJJI, B. DIU, F. LALOË, Quantum Mechanics, *Basic Concepts, Tools, and Applications*, **I**, Second Edition, Wiley (2019).
- [12] C. COHEN-TANNOUJJI, B. DIU, F. LALOË, Quantum Mechanics, *Angular Momentum, Spin, and Approximation Methods*, **II**, Second Edition, Wiley (2019).
- [13] F. COQUEL, C. MARMIGNON, Numerical methods for weakly ionized gas, *Astrophysics and Space Sciences*, **260**, **1-2**, 15-27 (1998).
- [14] E. ESTIBALS, H. GUILLARD, A. SANGAM, *Bi-temperature Euler Modelling for Fusion Plasma*, INRIA Research Report 9026, 2017.
- [15] D. DE SANTIS, G. GERACI, AND A. GUARDONE, Finite Volume and Finite Element Schemes for the Euler Equation in Cylindrical and Spherical Coordinates, *Journal of Computational and Applied Mathematics*, **236**, 4827-4839 (2012).
- [16] A. DECOSTER, P.A. MARKOWICH, B. PERTHAME, Modeling of Collisions, edited by P.-A. Raviart, *Series in Applied Mathematics*, Volume **2**, Gauthier-Villars, Paris (1998).
- [17] B. DESPRÉS, Lagrangian Systems of Conservation Laws and Approximate Riemann Solvers, in *Godunov Methods: theory and applications*, edited by E.F. Toro, Springer, New York (1999).
- [18] R. FITZPATRICK, *Plasma Physics: an introduction*, CRC, 2014.
- [19] J. FREIDBERG, PLASMA PHYSICS AND FUSION, Cambridge University Press, Cambridge, 2007.
- [20] J. FREIDBERG, *Ideal MHD*, Cambridge University Press, 2014.
- [21] D. FURFALO, R. SAUREL, A simple HLLC-type Riemann solver for compressible non-equilibrium two-phase flows, *Computers & Fluids*, **111**, 159-178 (2015).
- [22] S. GALERA, P.-H. MAIRE, AND J. BREIL, A two-dimensional unstructured cell-centered multi-material ALE scheme using VOF interface reconstruction, *Journal of Computational Physics*, **229**, 5755-5787, (2010).
- [23] J.P. GOEDBLOED, S. POEDT, *Principles of Magnetohydrodynamics: With Applications to Laboratory and Astrophysical Plasmas*, Cambridge University Press, Cambridge (2004).
- [24] E. GODLEWSKI, P.A. RAVIART, *Numerical Approximation of Hyperbolic System of Conservation Laws*, Applied Mathematics Sciences, **118**, Springer, New York (1996).
- [25] H. GUILLARD, R. ABGRALL, *Modélisation Numérique des Fluides Compressibles*, Series in Applied Mathematics, **5**, Gauthier-Villars, Paris, North-Holland, Amsterdam (2001).
- [26] S. GUSTAFSON, M. SIGEL, *Mathematical Concepts of Quantum Mechanics*, Second Edition, Universitext, **223**, Springer, New York (2011).
- [27] R. D. HAZELTINE, J.D. MEISS, *Plasma Confinement*, Dover publications INC, Mineola, New York (2003).
- [28] J. D. HUBA, PLASMA FORMULARY, Naval Research Laboratory, 2014.
- [29] B. B. KADOMTSEV, *Tokamak plasma, a complex physical system*, Institute of Physics Publishing, Bristol (1993).
- [30] P.-H. MAIRE, A high-order cell-centered Lagrangian scheme for compressible fluid flows in two-dimensional cylindrical coordinates, *Journal of Computational Physics*, **228**, 6882-6915, (2009).
- [31] P.-H. MAIRE, R. ABGRALL, J. BREIL, AND J. OVADIA, A cell-centered Lagrangian scheme for two dimensional compressible fluid flows problems, *SIAM Journal on Scientific Computing*, **29**, 1781-1824, (2007).
- [32] R. SENTIS, *Mathematical Models and Methods for Plasmas Physics*, Volume **1**, Fluid Models, Modeling and Simulation in Science, Engineering and Technology series, Birkhäuser, 2014.
- [33] E. F. TORO, *Riemann Solvers and Numerical Methods in Fluid Dynamics, A Practical Introduction*, 3rd Edition, Springer, Heidelberg (2009).
- [34] J. WESSON, *Tokamaks*, Third Edition, International Series of Monographs on Physics, **118**, Oxford Sciences Publications, Oxford (2004).